

APPROVAL SHEET

Title of Dissertation: Analysis of a Functionally Graded Interface between a Novel
Titanium Carbide Surface and Titanium Alloy Substrate

Name of Candidate: Nathanael R. Seay

Doctor of Philosophy, 2022

Dissertation and Abstract Approval: _____

L. D. Timmie Topoleski, Ph.D.

Professor

Department of Mechanical Engineering

Date Approved: _____

Curriculum Vitae

Name: Nathanael R. Seay
Degree and date to be conferred: Doctor of Philosophy, 2022
Collegiate institutions attended: Doctor of Philosophy, Mechanical Engineering
University of Maryland Baltimore County,
Catonsville MD.

Dissertation: "Analysis of a Functionally
Graded Interface Between a Novel Titanium
Carbide Surface and Titanium Alloy Substrate"

Graduate Certificate: (Date) Computational
Thermal/ Fluid Dynamics".

Master of Science, (**Date**), Mechanical
Engineering
University of Maryland Baltimore County,
Catonsville MD.

Dissertation: "Frequency Dependence of the
Piezoelectric Effect in Cow Bone"

Bachelor of Science, (**Date**) Mechanical

Engineering

University of Maryland, College Park MD.

Professional position held:

US Food and Drug Administration (FDA)

Mechanical Engineer, ORISE Research Fellow

University of Maryland Baltimore County,

Research Assistant.

University of Maryland Baltimore County,

Teaching Assistant.

U. S. Department of Commerce, Bureau of

Industry and Security, General Engineer.

Publications:

US Food and Drug Administration (FDA)

Mechanical Engineer, ORISE Re Seay,

Nathanael; Sullivan, Stacey; Zhu, Liang;

Rinaldi, Jean; Hariharan, Prasanna;

Vesnovsky, Oleg; Topoleski, LD. (**Date**). "A

Novel Forehead Phantom for Assessing Non-Contact Infrared Thermometers." (In review)

Sullivan, Stacey; Seay, Nathanael; Zhu, Liang;

Rinaldi, Jean; Hariharan, Prasanna;

Vesnovsky, Oleg; Topoleski, LD. (**Date**).

"Performance characterization of non-contact infrared thermometers (NCITs) for forehead temperature measurement", Medical Engineering & Physics, Volume 93, 2021

Sullivan, Stacey; Rinaldi, Jean; Hariharan,

Prasanna; Casamento, Jon; Baek, Seungchul;

Seay, Nathanael; Vesnovsky, Oleg; Topoleski,

L.D. Timmie. (**Date**). "Clinical Evaluation of

Non-Contact Infrared Thermometers."(In

review)

Sullivan, J.E. Rinaldi, P. Hariharan, J.P.

Casamento, L. Zhu, N. Seay, L.D.T. Topoleski,

O. Vesnovsky. (2015). "An Assessment of the

Accuracy of Non-Contact Infrared

Thermometers (NCITs)." [Poster]. Presented at
the FDA

Stacey J.L. Sullivan, Jean E. Rinaldi, Prasanna
Hariharan, Jon P. Casamento, Seungchul
Baek, Nathanael Seay, Oleg Vesnovsky, L.D.
Timmie Topoleski (2021). "Clinical Assessment
of Non-Contact Infrared Thermometers as a
medical countermeasure." [Poster]. Presented
US FDA's Science Forum

Abstract

ANALYSIS OF A FUNCTIONALLY GRADED INTERFACE BETWEEN A NOVEL TITANIUM CARBIDE SURFACE AND TITANIUM ALLOY SUBSTRATE

by

Nathanael Robert Seay

Doctor of Philosophy in Mechanical Engineering, 2022

University of Maryland Baltimore County

Professor L. D. Timmie Topoleski, Mechanical Engineering

The purpose of this research has been to explore the mechanical characteristics of a novel micro-textured surface. This exploration involved the use of plasma enhanced chemical vapor deposition (CVD) to deposit a thin film onto a metal substrate and to characterize its growth interface. A key to characterizing the film's interface was an assessment of the effect that the fabrication parameters had on the film's functionally graded and adhesion properties.

These stated objectives were divided into three focused activities designated specific aims 1 through 3. Specific aim one focused on the characterization of a novel composite material's surface using CVD onto a Ti6Al4V metal substrate. Specific aim two

undertook a comparative analysis of the computational adhesion of the composite film relative to that of a homogeneous laminate coating. Finally, specific aim three characterized the carbon penetration depth into the metal substrate, and by extension the robustness of the composite material's integration zone as a function of the CVD processing parameters.

Analysis indicated that the composite film surface of fabricated specimens consisted of crystalline channels with nanocrystalline features. X-ray diffraction (XRD) indicated that a thin film layer of titanium carbide was indeed present on the specimen surface. Mechanical testing of the film indicated that it was at least 22% harder than the "as received" pre-processed material. Through grid based indentation and atomic force microscopy (AFM) fast force mapping, it was demonstrated that an integration zone with mechanical properties varied gradually between substrate and thin film. These results were used to inform a molecular dynamic (MD) and finite element simulation model to evaluate the potential adhesive properties of the novel carbide surface. The result of MD simulation showed that the fabricated composite specimen had a functionally graded material interface that exhibited greater adhesion properties than laminate films. The finite element simulation indicated that the AFM identified functionally gradient sample had a greater resistance to fracture propagation than homogenous samples. Thus, taking the results in the aggregate, the novel specimen exhibited biomechanical characteristics that could improve the fitness and performance life span of artificial joints.



**ANALYSIS OF A FUNCTIONALLY GRADED
INTERFACE BETWEEN A NOVEL TITANIUM CARBIDE
SURFACE AND TITANIUM ALLOY SUBSTRATE**

by

Nathanael R. Seay

A Dissertation submitted to the Faculty of the Graduate School of

The

University of Maryland, Baltimore County, in partial satisfaction of the requirements for

the degree of

Doctor of Philosophy – Mechanical Engineering

2022

© Copyright by

Nathanael Robert Seay

2022

Acknowledgements

The greatest privilege of publishing a thesis is the opportunity to thank all those individuals who made it possible. Above all others, I want to express my gratitude to my family. My family has been my bedrock, my emotional support and my technical sounding board. Dad, thank you for resisting the urge to say “I told you so” when I finally figured out what you always knew – that determination to succeed is in my blood. Mom, thank you for always listening to my complaints and reminding me of the bright side. And to my brother, Kevin, words can’t express how much your influence has shaped me into the person I am today as I publish this work. It’s been a journey for both of us, now on to the next one.

Next, I want to thank my mentor and adviser, Dr. Topoleski for his guidance, encouragement, and support throughout my graduate studies. Dr. Topoleski the guidance you provided me in defining my own research path is greatly appreciated. If not for your thoughtful presence, motivation, and enthusiasm, I would never have come to appreciate my affinity for biomechanical engineering and its importance in everyday life. Also, thank you to all the people and institutions that made this research possible through donation of their time or facilities. Thank you to Dr. Karen Gaskell and the University of Maryland for taking the time to educate me on the technique of atomic force microscopy. Thank you to Dr. Yucheng Lan at Morgan State University for

teaching me x-ray diffraction techniques. Thank you to Matt Shaeffer at Johns Hopkins University for teaching me nanoindentation. And thank you to Dr. Tagide DeCarvalho for teaching me scanning electron microscopy. Finally, thank you Dr. Stacey Sullivan for always answering my questions with the utmost thoughtfulness.

As the pursuit of my degree now come to a close, I can say with certainty that the decision to carry out my Ph.D. at University of Maryland Baltimore County (UMBC) is the best one I could have made. I truly believe that the supportive atmosphere provided by the Mechanical Engineering Department and the Meyerhoff Program has been unparalleled. There are numerous individuals that recognized potential in me and therefore mentored me at every opportunity. Last but not least, I offer a heartfelt thanks to my confidant and mentor Judy for her patience, sound advice and guidance.

Table of Contents

Acknowledgements	4
Table of Contents.....	6
List of Figures	9
List of Tables	12
1 Introduction	1
1.1 Motivation	1
1.2 Research Objectives.....	4
1.3 Outline of the Dissertation.....	4
2 LIMB System and Specimen Foundation	6
2.1 Physical Experimentation.....	6
2.1.1 Methods	6
2.1.2 FGM Dynamics	12
2.2 FGM Fabrication Apparatus: The LIMB System	16
2.3 LIMB Metallographic Fabrication.....	20
2.4 Sample Properties.....	24
2.4.1 Observations	26
3 Specimen Fabrication and Characterization	27
3.1 Characterization of Novel LIMB Surface	28

3.1.1	Materials and Methods: Specimen Processing	32
3.1.2	Visualization of Specimen Surface	32
3.1.3	Specimen Characterization: Surface Microhardness	42
3.1.4	Specimen Characterization: Surface Nano Hardness.....	46
3.2	Assessment of Computational Adhesion	62
3.2.1	Application of Molecular Dynamics Technique.....	65
3.2.2	Modeling Substrate Film Interface.....	74
3.3	Characterization of Candidate Sample Design Parameters	81
3.3.1	Design of Experiment Modeling	83
3.3.2	Simulation of Material Dynamic Interaction	87
3.3.3	Fitness of Composite Samples	98
3.4	Observation.....	98
4	Conclusions and Recommendations.....	100
4.1	Physical Fabrication Experimental Outcomes (Objective 1).....	101
4.1.1	General Summary	103
4.2	Virtual Fabrication Modeling and Simulation Outcomes.....	105
4.2.1	Virtual Fabrication Experimental Outcomes (Objective 2)	105
4.2.2	Virtual Fabrication Experimental Outcomes (Objective 3)	106
4.3	Recommendations for Future Work.....	108
4.4	Final Remarks.....	109

5	References.....	111
6	APPENDIX A: MPACVD Standard Operating Procedures	118
7	APPENDIX B:	141
8	APPENDIX C	149
9	APPENDIX D:.....	154
10	APPENDIX E	160

List of Figures

Figure 1. Artificial hip joint implant	2
Figure 2. Hip Implant adapted from [15]	3
Figure 3. Young's Modulus for exponential function.....	13
Figure 4. Profile of candidate sample integration zone.....	14
Figure 5. Young's modulus corresponding to power law.....	15
Figure 6. Young's modulus for sigmoid function.....	16
Figure 7. LIMB lab MPACVD system.....	17
Figure 8. Conceptual LIMB Chamber Environment.....	19
Figure 9. XRD of CoCrMo after plasma processing	20
Figure 10. Brain coral like LIMB surface.....	21
Figure 11. Weight gain of CoCrMo after plasma processing.....	22
Figure 12. Titanium Carbide coating	23
Figure 13. Preliminary process matrix results.....	23
Figure 14. Track of CoCcMo without coating	24
Figure 15. Track of CoCcMo with novel coating	24
Figure 16. Wear factor of coated and uncoated specimens	25
Figure 17. Sample 9A coating and at scale	33
Figure 18. Sample 9A 40X magnification	34
Figure 19. SEM imaging of sample 9A (2500X)	35
Figure 20. SEM imaging of sample 9A.....	36
Figure 21. Image thresholding	37

Figure 22. Black and white image	38
Figure 23. Highlighted features	38
Figure 24. Summary statistics	39
Figure 25. Highlighted pores.....	39
Figure 26. Pore summary statistics	40
Figure 27. An unprocessed sample cross section	40
Figure 28. Sample 5A at 40 times magnification	41
Figure 29. Sample 5A XRD patterns	42
Figure 30. Vickers diamond indenter.....	43
Figure 31: Sample 8A surface microhardness.....	45
Figure 32. Types of indenters used in nano indentation	47
Figure 33. Typical nanoindentation loading cycle.....	49
Figure 34. Load Displacement.....	50
Figure 35. Nano indentation hardness measurements	51
Figure 36. Illustration of grid-based indentation	51
Figure 37. Experimental probability density function.....	52
Figure 38. Cumulative PDF generated by the algorithm.....	55
Figure 39. AFM raster-scanning	56
Figure 40. Force deflection curves.....	57
Figure 41. The hard film to soft substrate deposition profile	59
Figure 42. Sample image deposition matrix	60
Figure 43. Computed fraction of sample image hard versus soft material.....	60
Figure 44. Actual polynomial curve fit for sample image	62

Figure 45. Structural variability of molecular dynamics	64
Figure 46. Conceptual system of atomistic energy supporting sample adhesion characterization.....	66
Figure 47. Interatomic potential graph.....	67
Figure 48. Simulation pre/post composite TiC – TiAl results.	76
Figure 49. Stress fracture driven failure in composite materials.....	76
Figure 50. FEM crack Stress testing geometry.....	78
Figure 51. Material linear meshing scheme.....	79
Figure 52. Stressed material properties variability as a function of depth.....	79
Figure 53. Non-uniform stressed profile of sample material.....	80
Figure 54. Sample fracture toughness	80
Figure 55. Graphical representation of a two-level design with 3 factors [49]	85
Figure 56. Common surfaces generated using RSM [63]	86
Figure 57. DOE model assuming a linear (max depth) and quadratic (average depth) response.....	88
Figure 58. Common temperature range of natural and human elements	90
Figure 59. Confidence interval for estimated maximum depth of material penetration.	95
Figure 60. Maximum penetration depth as a function of Factor 1 and Factor 2.....	95
Figure 61. Estimated average penetration depth as a function of Factor 1 and Factor 2	97
Figure 62. Visualization of average penetration depth.....	98

List of Tables

Table 1. LIMB subsystem supporting sample deposition process.....	17
Table 2. Software codebase used in this thesis	28
Table 3. Sample Material Ingot Chemical Analysis.....	29
Table 4. Fabricated Candidate Specimen.....	30
Table 5. Typical hardness values for some common materials are listed below [45][46]	44
Table 6. 2NN MEAM simulation initialization parameters for singular systems.....	73
Table 7. 2 NN MEAM parameters for binary systems.....	74
Table 8. Morse potential parameters for Al-C interactions	74
Table 9. Available DOE Computational Power provided.....	91
Table 10. DOE simulation results.....	91
Table 11. Response 1 (Max Depth) Fit Summary.....	92
Table 12. DOE Updated model: Response 1 (Max Depth) ANOVA Linear Model	92
Table 13. Response 1 Max depth Updated Model.....	93
Table 14. DOE Max Depth Updated model: Response for Factor 1.....	93
Table 15. Response 2 (Average Depth) Fit Summary.....	95
Table 16. Response 2 (Average Depth) ANOVA Quadratic Model.....	95
Table 17. Updated Analysis of Variance (ANOVA)	96

Chapter 1

1 Introduction

1.1 Motivation

Osteoarthritis (OA) is a painful and frequently debilitating affliction affecting 27 million adults in the United States alone as of 2016. [1] Major clinical symptoms include chronic pain, joint instability, stiffness and narrowing of the joint space.[2] Globally, approximately 10% of men and 18% of women over the age of 60 live with the condition. Eighty percent experience some degree of reduced movement, and 25% are burdened with crippling pain that makes basic activities all but impossible. In 2009, knee OA accounted for 29% of cases while hips accounted for 12% of cases. Among these cases, hip related OA was highest among those between the ages 50 and 64. For 65 years old and older, 47% suffered from some form of knee OA. [3] While other joints such as hands are also affected by OA, joints such as the ankle, wrist and shoulder are rare. [4]

The most pronounced risk factor for OA is age. However, obesity, and sports related dynamic activities are contributing factors. [2] Obesity has been shown to increase the

incidences of OA and obesity plays a role in the severity of the condition.[5][6] Obesity is also responsible for a pronounced increase in biomechanical loading.

Historically, treatments for OA have focused on relieving symptoms: through the employment of drug therapies. However, for extreme cases of pain and deterioration associated with OA, joint replacement remains the best option. Joint replacement, full or partial, continues to be one of medicines most successful interventions. [7]

In day-to-day life, bones are subjected to stress of up to approximately 4 MPa. The mean load experienced by hip joints as depicted in Figure 1 and Figure 2, can be up to approximately 3 KN. Bearing loads due to human activities can result in as much as a ten-fold [10] [*]increase in joint loading.

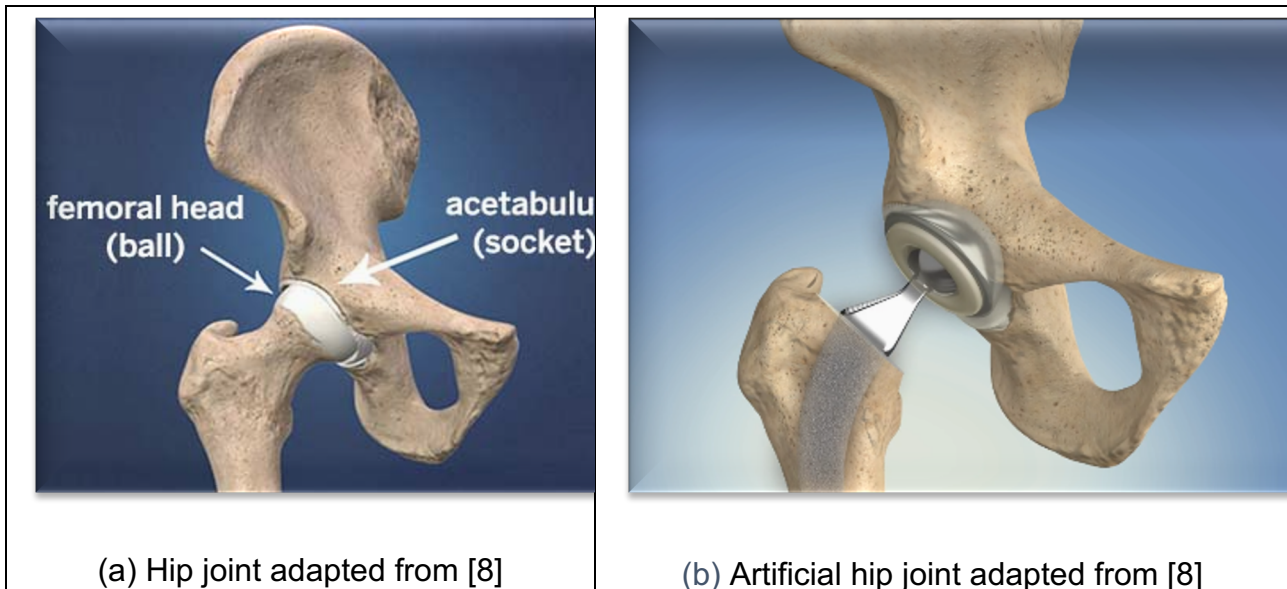


Figure 1. Artificial hip joint implant

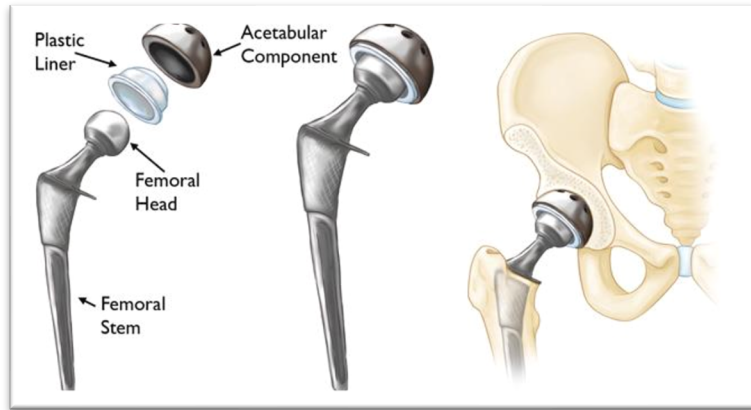


Figure 2. Hip Implant adapted from [15]

The stresses associated with joint loading can subject the body to significant articulating effects such as fracture and wear. These effects have the capacity to compromise the structural integrity of composite biomaterials. To minimize the performance degradation, the design and fabrication of functionally graded materials (FGM) parameters can be tuned to customize to achieve the desired properties in the resultant specimen. Despite the ability to customize a fabricated specimen, it is important to conduct fitness testing to validate its properties.

Biomaterials used to augment or replace biomechanical structures such as hip joints can broadly be grouped into three basic categories: Metal on Polyethylene (MoP), Metal on Ceramic (MoC), or Metal on Metal (MoM).

In recent years, techniques have been developed to address the design and fitness limitations of metallic biomaterials. Specifically, fabrication techniques have been

developed to make the surface of candidate biomaterials resilient in the face of articulating forces such as abrasion and wear. While various deposition techniques exist to obtain thin film surfaces, chemical vapor deposition (CVD) is assumed in the fabrication and analysis of candidate materials in this document.

1.2 Research Objectives

The scope of this thesis research encompasses both conceptual (i.e., virtual modeling and simulation) and physical experimentation. This effort is divided into three focused activities designated specific aims 1 through 3. Each specific aim corresponds to a defined thesis objective. They are: (1) characterizing the surface of a novel candidate material deposited onto a metal substrate.; (2) characterizing the computational adhesion of the candidate film relative to that of typical laminate or homogeneous candidate material; and (3). characterizing the depth of penetration of carbon, and by extension the depth of the integration zone, as a function of design parameters.

1.3 Outline of the Dissertation

Chapter 2 of this thesis introduces a discussion of previous work used to fabricate compositional graded materials. Included in the discussion is a synopsis of the system used to perform the actual fabrication. Additionally, the basic techniques used to characterize the fabricated composite sample specimens is presented. Chapter 3

provides the details of the experimentation and analysis in support of the core objectives stated for this thesis. Specifically, the physical and virtual fabrication of the novel candidate samples, in the characterization of microstructural features are also described in Chapter 3. Finally, Chapter 4 of this thesis concludes with a discussion of the broad conclusions, lessons learned, and recommendations for future work.

Chapter 2

2 LIMB System and Specimen Foundation

2.1 Physical Experimentation

In order to address the objectives of this thesis, it is necessary to both fabricate and characterize the resultant material. The fabrication of candidate samples will be conducted using an experimental system established at University of Maryland Baltimore County (UMBC). The fabrication techniques will build on prior work conducted by other researchers.

2.1.1 Methods

Composite biomaterials are evolving all the time. Based on the target application, it is possible that composite specimens can be fabricated to meet necessary performance criteria. In general, composite materials have three fundamental elements: (1) the matrix (ceramic or metal) as the continuous phase; (2) reinforcements as the discontinuous phase (fibers and particles); and (3) a fine interphase/interface region.

The goal of any fabrication method is to orchestrate the composition of these three elements. That orchestration relies upon fabrication method and precisely controlling the associated deposition parameters (e.g., temperature, pressure, flow rate, and concentration). There are biomechanical advantages and disadvantages to each of the techniques. A few of these techniques are discussed below.

Method 1: Metal on Polyethylene (MoP) Implants

MoP implants are one of the most common and have the longest track record. [9] They are generally considered for patients that are over the age of seventy or patients likely to engage in activities that involve a lot of impact. [10] These implants shed a fair amount of wear particle debris, but the effects of the debris are mostly local to the implant. [11]

The first hip implants used the low friction polymer, polytetrafluoroethylene (PTFE) as the bearing material to replace the natural acetabulum. [12] However, due to poor wear performance these implants typically failed within a couple of years. Ultra-high molecular weight polyethylene (UHMWPE) eventually replaced PTFE. UHMWPE is a specific type of polyethylene (PE), with an extremely high molecular mass. the American Society for Testing and Materials (ASTM) specifies that UHMWPE has a molecular weight greater than 3.1 million g/mol.[14] This polymer exhibited a much better wear performance.[13]

It is important to note that polyethylene components, like most medical devices, are often sterilized by gamma radiation. However, exposure to gamma radiation can break the chains that form the molecular backbone of the polymer. If simultaneously exposed to air and gamma radiation, the damaged polymer can react with oxygen to cause harmful changes in the material's properties such as a decrease in molecular weight, loss of ductility, and a decrease in strength. The aforementioned exposure combination can also make the polymer more susceptible to wear. [15]

Interestingly enough, elevated levels of radiation, beyond what is needed to sterilize a biomaterial specimen, can actually improve wear performance. The improved performance results from an elevated level of crosslinking. Put simply, crosslinking is a set of chemical reactions that induces greater connective resilience in adjacent polymer chains. [16] A potential disadvantage is that increased crosslinking, while improving wear, can also make the polymer more brittle. [17]

Method 2: Ceramic Bearings

Two types of ceramic bearing materials are generally used. They include a zirconia-toughened alumina and an oxidized zirconium material. Alumina CoP bearings for hip replacement showed reduced wear rates over those normally seen with MoP bearings. With this reduction in wear particles there was an associated reduction in local tissue damage. [18] The alumina on alumina combination has shown very low wear and

fracture rates in highly active populations. [19] There is, however, an audible squeaking sound in 1-10% of patients. [20]

Oxidized zirconium is a metal-ceramic hybrid technology. High pressure and heat are used to convert the surface of the metal zirconium alloy into a ceramic. This leads to an implant that has the surface properties of a ceramic (e.g., hard, smooth) with the bulk properties for a metal. Clinical data on oxidized zirconium is positive but lacks sufficient study to prove that the positive results leads to a longer lasting implant.[21]

Method 3: Metal on Metal Bearings

Metal on metal bearings have been the subject of much controversy. Fundamentally, metal on metal bearings are implants that have both a metal femoral head and acetabular cup (see Figure 2). Metal on metal could also refer to hip resurfacing implants which preserve much of the original bone but cover the original bone with a thin metal element.

Metal components were originally used because they could be engineered to a very smooth and hard finish. The idea was that the smooth, hard surfaces would have a low wear rate. The wear rate of these devices are estimated to be 60 times lower than MoP implants. [22] A low wear rate was thought to improve the longevity of the implant. The low wear rate also lead to reduced incidences of osteolysis due to the absence of

Polyethylene wear particles. [24] Other advantages to MoM devices include the ability to manufacture large femoral heads and thin acetabular components.

The downside of using metal components in artificial hip implants is the increased shedding of metal ions. The multitude of reactions that can occur are grouped together under the term Adverse Reactions to Metal Debris (ARMD). The spectrum of ARMD ranges from small cysts to large pseudotumor. [22] Cobalt and chromium are two metals whose ions contribute to ARMD.[25]

There are specific design characteristics that lead to failure of MoM devices. It is known that implantation of the acetabular cup at abnormal angles can lead to increased edge loading and increased wear. [26] Also, shallow acetabular cups like those associated with the DePuy Orthopaedics ASR Hip Replacement System (recalled in 2009) device exhibited increased edge loading and increased wear. [26] Recently, it has been suggested that trunnionosis, wear at the head-neck junction of the implant, is a significant contributor to metal wear particle release. This is, generally speaking, an issue with modular design implants. [27]

Method 4: Bearing Surface Modification

Surface coating has led to improvement in tribological, mechanical, and biocompatibility related properties. Surface modification provides morphological, physicochemical, and biochemical adaptations to the local environment. [28] The treatments of surfaces have

included various hard/wear resistant coatings such as metal nitrides, carbides, carbonitrides and diamond like carbon . These coatings have been shown to improve hardness, elastic strain and wettability of the surface. [29]

Physical Vapor Deposition (PVD) is a method for generating hard coatings by means of a partially ionized vapor. The most common methods are sputtering and cathodic arc. [30] In sputtering, the vapor is formed by a metal target being bombarded with energetic gas ions. The cathodic arc process uses repetitive vacuum arc discharges to strike the metal target and to evaporate the material. PVD coatings can be deposited at temperatures below 70°C or up to 600°C, depending on the application. It has been documented that coating failure is due to corrosion introduced through local defects (i.e., micro-droplets, pinholes or other point defects) that are inherent to the PVD process. [31]

Method 5: Functionally Gradient Materials and CVD

CVD is a process wherein thermally induced chemical reactions, between a gaseous reagent and a solid substrate, result in a thinly deposited film. An important advantage of the CVD process lies in the fact that the reagents are gasses. CVD is not a line-of-sight process like PVD. It can be used to coat restricted access surfaces. A disadvantage of CVD is the high temperatures required to induce the reaction; temperatures can range from 600°C to 1100°C. [32] One technique to combat this is the use of plasma enhanced or plasma assisted devices. In Microwave Plasma Assisted

CVD (MPACVD) a plasma source is used to supply energy to the reaction thereby lowering the temperature required by hundreds of degrees. [33]

A chief advantage of CVD and its derivative MPACVD is the potential creation of a FGM interface between the substrate and the hard thin film surface. It is the primary contention of this thesis that the output of the MPACVD process is a functionally gradient interface rather than a simple laminate thin film as previously assumed

2.1.2 FGM Dynamics

FGMs have received increasing attention due to their advantageous properties. In FGMs, dissimilar materials are joined with the prospect of benefiting from the properties of both material systems. We expect to see a particulate composite interface having an “integration zone” with a gradual transition that phase from volume of high surface particulates to one of pure substrate-like particulates.

The fabrication of FGMs affords the ability to control deformation, manage the material's dynamic response, corrosion, wear, and its application in diverse complex environments.

There are several ways to idealize the heterogeneity of FGM composite with mechanical properties changing smoothly with respect to spatial coordinate axis. Two commonly found in the discussion of sample plate FGMs are the exponential and power

laws. These functions are used to describe the volume fraction of particulates that varies along the spatial coordinate axis of the FGM. The exponential law is defined by:

$$P(z) = P_t \exp \left(-\lambda \left(1 - \frac{2z}{h} \right) \right) \quad (1)$$

where,

$$\lambda = \frac{1}{2} \ln \left(\frac{P_t}{P_b} \right) \quad (2)$$

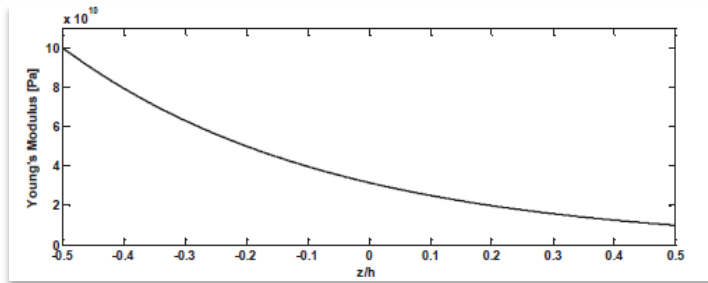


Figure 3. Young's Modulus for exponential function

Here $P(z)$ is representative of an aspect of the material's material properties like Youngs Modulus (Figure 3). The Youngs Modulus, indicate how easily a material can be stretched and deformed and is determined by the slope of the curve describing stress versus strain. The Youngs modulus is used to describe the changes in the Young's elastic moduli between graded materials. P_t (top carbide modulus) and P_b (bottom substrate modulus) are material properties corresponding to the top and bottom surface layers of the composite plate respectively. The existence of the differential moduli is evident that the deposition process produced a film on the material substrate.

Knowing the variation of the composite material's elastic moduli enables a closed form solution for some fabricated composite solutions. The applicability of the exponential, power law or sigmoid function will depend upon the expected characteristic of the integration zone volume fraction relative to the distance beyond the substrate interface.

Figure 4 provides a conceptual view of the expected distribution of surface material in the integration zone. The ratio of the integration zone penetration to the total thickness of the material sample substrate is given by z/h . The modulus at any point on the sample varies continuously in the thickness direction based on the volume fraction of the constituents within the sample.

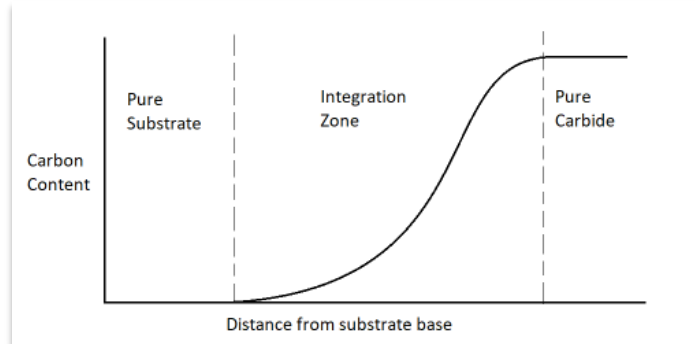


Figure 4. Profile of candidate sample integration zone

For the Power law,

$$P_z = (P_t - P_b) \left(\frac{z}{h} + \frac{1}{2} \right)^n + P_b \quad (3)$$

In equation 3, 'n' is the material grading index which depends upon the specimen design requirements. The volume fraction of the second material corresponding to P_t is given by $f = (\frac{z}{h} + \frac{1}{2})^n$

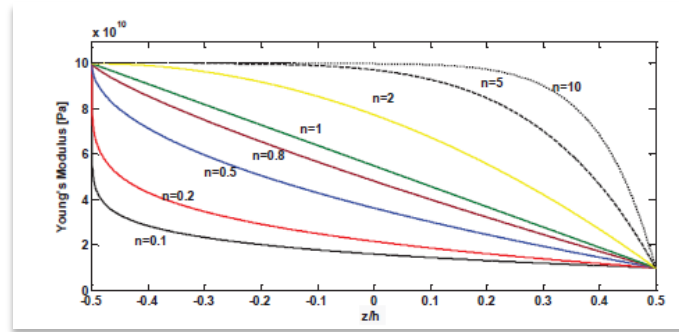


Figure 5. Young's modulus corresponding to power law

The material properties of the sigmoid FGM can be determined by using the Rule of Mixture (see equation 20) For the sigmoid function of FGM structures, the volume fraction consisting of two power-law functions can be written as:

$$P_z = (P_t - P_b)(\frac{1}{2} \left(\frac{z}{h} - \frac{1}{2} \right)^n) + P_b \quad 0 \leq z \leq \frac{h}{2} \quad (4)$$

$$P_z = (P_t - P_b)(1 - \frac{1}{2} \left(\frac{z}{h} + \frac{1}{2} \right)^n) + P_b \quad -\frac{h}{2} \leq z \leq 0 \quad (5)$$

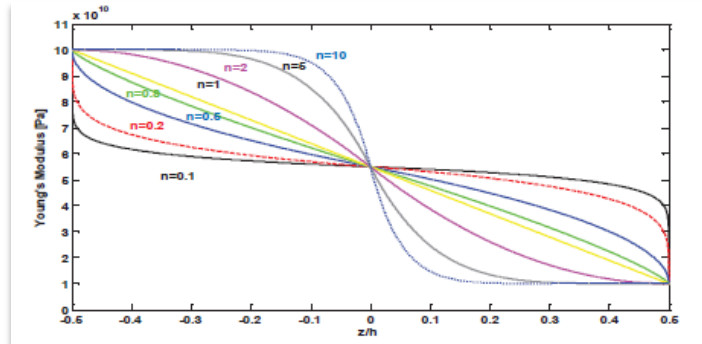


Figure 6. Young's modulus for sigmoid function

Generally, the Young's modulus varies most at the edges of the composite plate sample. Comparing the functions, for $n > 1$, the modulus varies rapidly near the top of the composite sample. Whereas, for $n < 1$, the modulus decreases rapidly near the bottom of the composite plate. As the modulus increase, the stiffer the composite material. Thus, the stress and deformation potential will be small.

2.2 FGM Fabrication Apparatus: The LIMB System

The LIMB MPACVD system depicted in Figure 7 was custom built for the UMBC lab. This system was custom built for the UMBC lab in a prior effort. At its core the LIMB system consists of six major subsystems: a sample chamber made of fused quartz, a 2.45GHz microwave generator, an optical pyrometer for monitoring temperature, a cooling jacket, precursor gas flow and a vacuum pump.

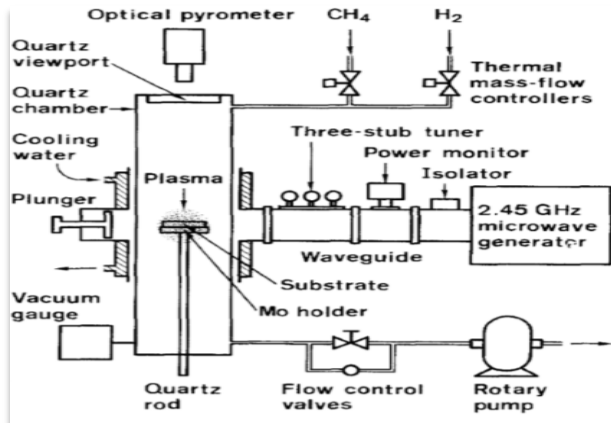


Figure 7. LIMB lab MPACVD system

The preparation of a specimen require establishing a highly controlled environment within the LIMB chamber. A summary of equipment supporting the creation of sample specimen is depicted in Table 1. These equipment were instrumental in establishing and maintaining the controlled environment necessary to produce the samples.

Table 1. LIMB subsystem supporting sample deposition process.

LIMB Subsystem	Operating Range	Manufacturer	Model
Exhaust Valve Controller	Zero Torr environment (1 atmosphere = 760 Torr)	MKS Instruments, Burlington MA	Type 252A
Baratron Pressure Gauge		MKS Instruments, Burlington MA	Type 122AA-0100 AD
Digital Readout	+/- 0.1 Torr	MKS Instruments, Burlington MA	PDR-C-2C
Digital Flow Controller	+/- 0.01sccm	MKS Instruments, Burlington MA	Type 246
Microwave Generator	0.1 – 1.5 KW @ 2.45 GHz	Toshiba Corp, Japan	
Variable Voltage Transformer		Toshiba Corp, Tokyo	SLIDASD2220
Infrared Thermometer		MIKRON Instrument Co., NJ	M90H
Polishing Table		Buehler LTD	Ec850omet III Model

Ultrasonic Bath		Col-Parmer Instrument Co.	8849-00
Polishing Media		DiaDuo, Struers Suspension DP-Floc, Struers polishing cloth	
Diamond Saw		(ISOMET brand, Buehler, Lake Bluff, Illinois)	
Berkovich Indenter		Nano mechanics, Inc's iNano system (Oak Ridge, TN)	
AFM		Cypher ES environmental AFM, Asylum Research, Goleta CA	
Tip		Tap300AI-G, Budget sensors, Sofia Bulgaria	

The creation of material samples using the LIMB system is accomplished through the use of procedures [34][37] that employ microwave energy heated plasma. Within the conceptual LIMB chamber depicted in Figure 8, precursor gases (CH_4 and H_2) are mixed and subsequently pass through the plasma region. The microwave energy heats the gas in the discharge to temperatures ranging from 600°C to 1500°C. As the gasses pass through the plasma discharge activation region, they are ionized and dissociated.

The activation region, generated by microwaves, creates ions, electrons, reactive radicals and atoms. As these reactive radicals are deposited onto the substrate surface, they undergo a set of complex surface reactions. The hydrogen introduced into the chamber is physically absorbed into the substrate where H_2 molecules decompose due to heat of substrate. Additionally, the methane introduced into the chamber is chemically

absorbed into the substrate. In the process, the carbon becomes dehydrogenized leading to the production of carbides.

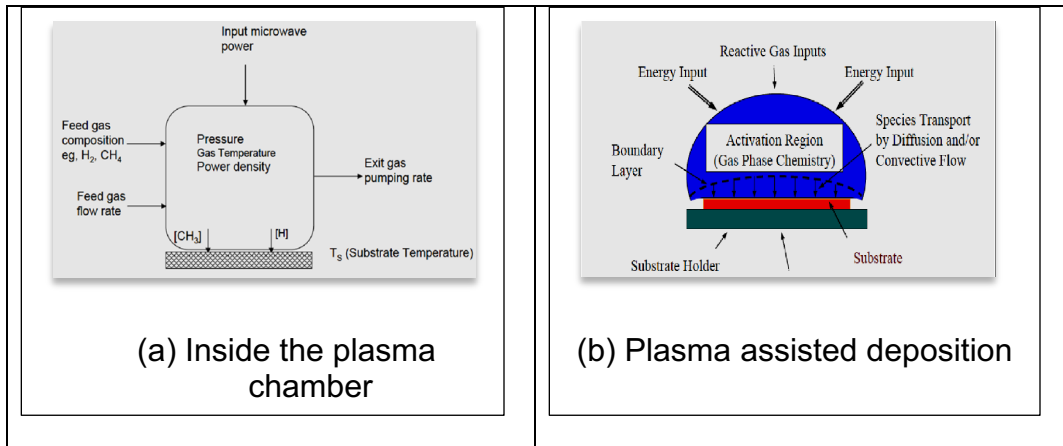


Figure 8. Conceptual LIMB Chamber Environment

One of the most important parameters in the production process is the substrate temperature during deposition. The experimentation temperature range employed during this project ranged from **600°C to 1000°C**. Other parameters of interest are the **total time of deposition and constituent gases precursor balance measured in percent**. The noted parameters effect the two types of essential radicals needed at the sample's growth surface: atomic hydrogen (*H*) and carbon containing growth species such as (*CH₃*). At low pressure, **this requirement is satisfied by [34][32]**:



Where, *M* is a third body.

2.3 LIMB Metallographic Fabrication

Prior Fabrication Effort

In prior work [35][39], a system originally designed to deposit diamond films was repurposed. Pieces of as-cast (F75) and forged (F799) CoCrMo alloys were processed using MPACVD. X-ray diffraction analysis (XRD) patterns (Figure 9) of the processed material indicates that the alloy consisted of mixed phases including Cr_3C_2 , Cr_2C , Cr_7C_3 , Cr_{23}C_6 and Co_2C . [35][41]

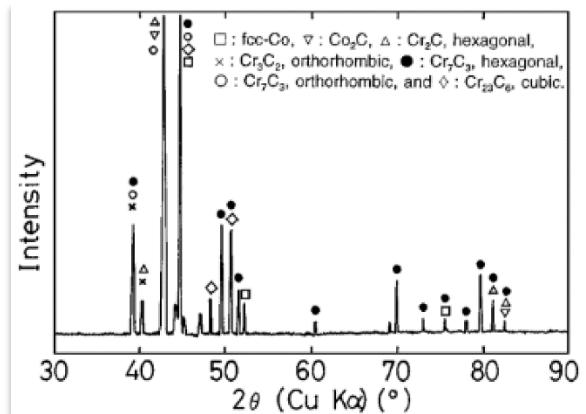
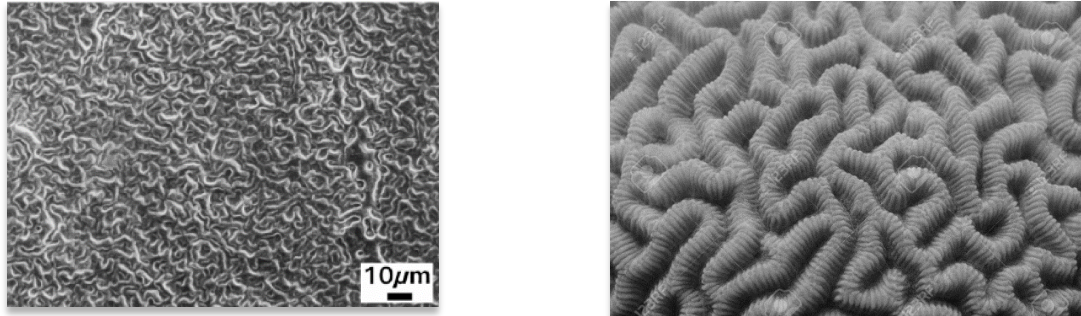


Figure 9. XRD of CoCrMo after plasma processing

The deposition results in a unique surface growth morphology as observed via a Scanning Electron Microscopy (SEM). The crystalline grain clusters was determined to be made up a uniformly distributed texture similar to “brain coral” as seen in Figure 10.



(a) Brain coral-like LIMB surface

(b) Brain coral

Figure 10. Brain coral like LIMB surface

The size of the crystalline grains in the top cluster layer was approximately 3 to 4 micrometers. The total thickness of the surface coating was about 10 micrometers.

As shown in Figure 11, the weight in the CoCrMo specimens increased with an increase in plasma deposition processing time [35]40]. That is, given the deposition rate, the thickness of the deposited film increases in a nonlinear fashion. The material properties have a relatively significant impact on the deposition rate.; hence, an increasing surface thickness over time. The differences observed in Figure 11 suggests that it would be wise to generalize the growth of a sample's surface from one material to the next. However, the dat could by used to define an initial starting point for experimental efforts.

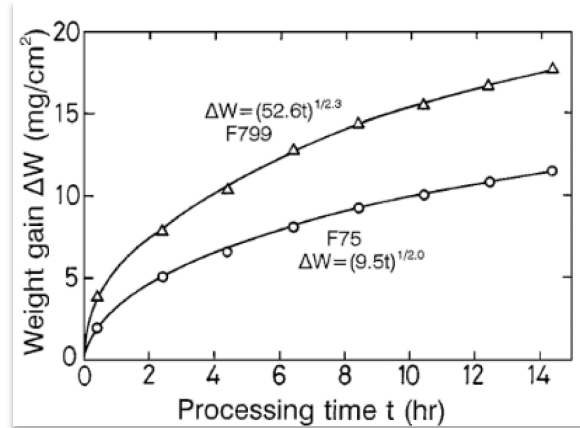


Figure 11. Weight gain of CoCrMo after plasma processing

The deposited surface showed a wide range of hardness ranging from HV 1000 to HV 2100 (compared to HV 350 of as-cast). The hardness values (designated “HV”) are commonly measured on the Vickers scale. However, the Vickers scale can be converted to MPa by multiplying the HV value by 9.807.

Due to prior success of the LIMB surface on CoCrMo alloy, the technology was transferred to titanium alloys, specifically to Ti6Al4V titanium alloy. Until recently, titanium's use as a bearing surface has been limited due to its naturally poor wear performance. However, it has high hardness, abrasion resistance, oxidation and a low coefficient of friction of , titanium carbide (TiC) makes it an excellent candidate. Additionally, TiC has superior biocompatibility and corrosion resistance with a density and elastic modulus closer to bone than CoCrMo. As seen in Figure 12, the titanium LIMB surface exhibit random peaks and valleys similar to those formed on CoCrMo [36][43].

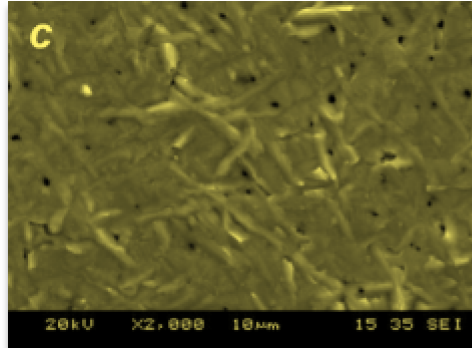


Figure 12. Titanium Carbide coating

Figure 13 indicates that a 1% methane concentration the hardness decreased as the processing temperature is increased.

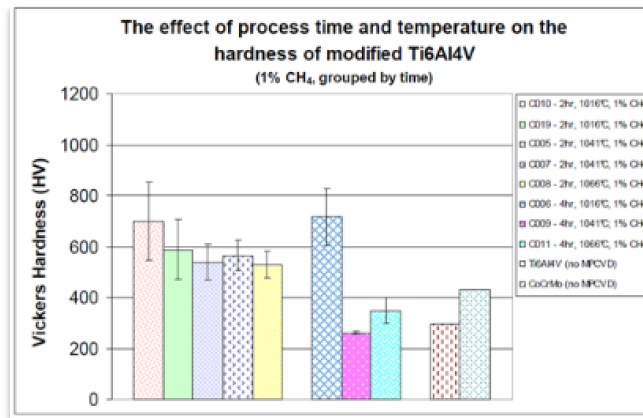


Figure 13. Preliminary process matrix results

At a 5% methane concentration, the opposite occurred, and the hardness increased as the processing temperature increased, up to 300% over the control Ti6Al4V surface.

This change represented a 200% increase over the control CoCrMo [36] [42]. The

increase in hardness exhibited in this prior work demonstrated an improvement in the material property when methane is added. However, the proportion of constituent added to the composite material needs to be carefully controlled during the fabrication process. The variability exhibited suggests that the composite material's property can be "tuned" to achieve a desired characteristics by managing the factors controlling the deposition process.

2.4 Sample Properties

Figure 14 and Figure 15 presents exemplary wear profiles performed on the LIMB surface using a sapphire ball on a rotating CoCrMo disk under harsh conditions: High contact stress (2.4 GPa), Slow sliding speed (17mm/s), no lubrication and deionized water as lubrication.

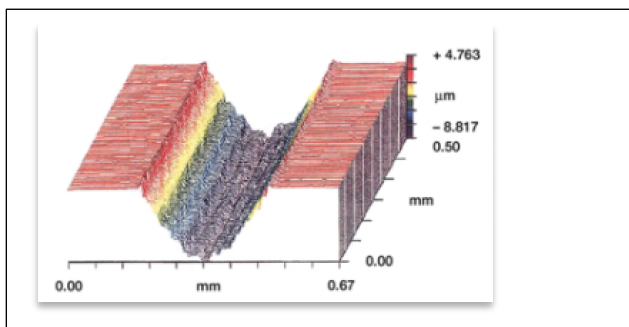


Figure 14. Track of CoCcMo without coating

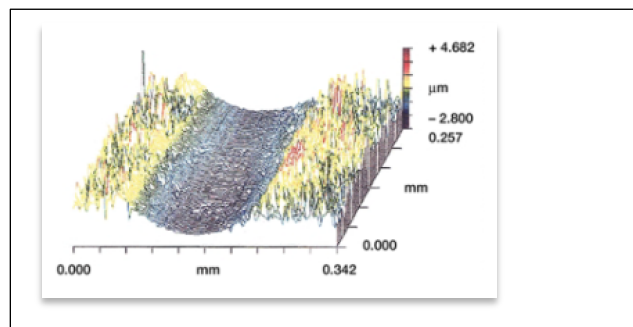


Figure 15. Track of CoCcMo with novel coating

Interference profilometry plots in Figure 15 show that the wear track generated on the carbide coated surface is much shallower than the track on the uncoated surface [37][44]. Under dry conditions the wear factor for uncoated CoCrMo is an order of magnitude higher than the carbide coated sample under dry conditions [37][45]. As indicated by prior work, the composition of the sample composite plays a role in the wear factor (Figure 16). The selection of materials can result in an order or more difference in wear factor under dry conditions. It is expected that the addition of other materials into the composite may result in the strengthening and improvement of the resultant abrasive wear resistance. Based on the experiments carried out the significance of the abrasive wear resistance of material layers when compared to an uncovered substrate is an important consideration. This is a potential concern when implant wear has the potential of releasing high levels of metal ions into surrounding tissue or blood.

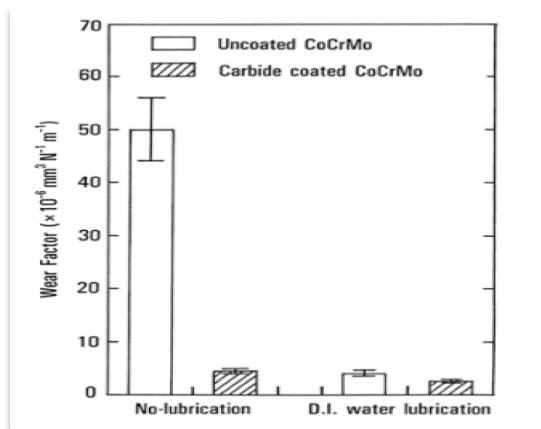


Figure 16. Wear factor of coated and uncoated specimens

2.4.1 Observations

The MPACVD employed in the LIMB system proved successful in the fabrication of both CoCrMo and Ti6Al4V composite material specimens. However, the hardness and wear characteristics of the titanium alloy-based specimen suggested better overall performance.

In addition to being harder with a low frictional coefficient, the **titanium-based** LIMB surface retains the benefits of the bulk material while effectively doing away with the disadvantages like poor wear performance. Also, **there is compounding** evidence that textured surfaces, like the fabricated surface within the LIMB system, can further decrease the COF by as much as 75%. Textured surfaces may retain lubricant and trap abrasive particles. Thinking beyond the bearing surface, the LIMB coating can be used to reduce wear between other metal modular components to the implant such as the stem-neck and head junction. **Using surface modifications in conjunction with lubricants in the construction of composition gradient materials offers excellent potential to target the composite material properties and thus prolong the life of fabricated specimens.**

An open question that this thesis addresses is the nature of the composite and its interface. Specifically, what does the interface look like; is the interface graded, and does it present good adhesion properties. In the next section this question will be addressed through both physical and virtual experimentation.

Chapter 3

3 Specimen Fabrication and Characterization

The core of this thesis is broken into three distinct parts detailed in sections 3.1, 3.2 and 3.3. The first of which, 3.1, is chemically identifying the surface created through the newly transferred MPACVD process then subsequently determining its mechanical properties. However, before we attempt to determine the chemical and mechanical properties of the surface, we examine the surface using light and scanning electron microscopy.

Then in section 3.2 virtual fabrication of composite materials using computational modeling and simulation offers the means to understanding the material's strengths and weaknesses. Since the physical properties of composite materials depend upon the ability to control a set of operating parameters such as temperature, constituent flow rate, temperature, and time, being able to establish a set of optimum values is critical to the properties of the final products.

Two key techniques available to support the virtual modeling and simulation of composite materials are molecular dynamic models and design of experiment. Both of which are used in section 3.3 to understand how processing parameters affect the

depth of the integration zone. Table 2 lists the software applications used to conduct the virtual fabrication and analysis performed in support of this thesis.

Table 2. Software codebase used in this thesis

Software	Purpose	Source	Remarks
LAMMPS	Molecular Dynamics Simulation	https://www.lammps.org/	
Imagej and Otsu Method	Image Thresholding and separation	https://imagej.nih.gov/ij/	
OVITO	Molecular Dynamics visualization	https://www.ovito.org/windows-downloads/vesta	
VESTA	Arranging the simulation domain	https://jp-minerals.org/vesta/en/mm	
Custom code adapted from David Mercier	Takes in nanoindentation data and returns deconvolution histogram	Written in Matlab	Appendix B
Custom code written Nathanael Seay	Takes in AFM images and returns Youngs Modulus profile	Written in Matlab	Appendix C
Custom code adapted from Mark Tschopp	Performs MD ‘pull’ experiment	LAMMPS	Appendix D
Custom code adapted from X. Yang	Performs MD ‘impact’ experiment	LAMMPS	Appendix E
The materials project	Material properties for MD simulation	https://materialsproject.org/a	
atomsk	Converting Vesta output to LAMMPS input	https://atomsk.univ-lille.fr/	
Abaqus	Stress concentration experiment	https://www.3ds.com/products-services/simulia/products/abaqus/	

3.1 Characterization of Novel LIMB Surface

The fabrication of sample specimens begin with the certificate of test provided by the commercial distributor (Vincent and Associates, Minneapolis, MN). The certificate states that the Ti6Al4V alloy base substrate material's composition as a percent of weight was as shown in Table 3. The alloy consisted of a 0.5-inch diameter rod annealed at 1300°F for two hours. Individual Ti6Al4V extra low interstitial specimens were cut and polished to a mirror finish using increasingly fine silicon carbide papers (P500, P800, P1200, P2400, and P4000) and a 3µm diamond suspension.

Table 3. Sample Material Ingot Chemical Analysis.

Sa	Mo	Zr	Cu	Fe	Mn	V	Si	Al
0.013	.001	<0.001	<0.001	0.16	<0.001	4.06	0.013	6.07
C	O	N	Ni	Cr	B	Y	BT	
0.035	0.11	0.006	0.0035	0.002	<0.001	<0.0004	1790	

. Once cleaned with soap and de-ionized (DI) water, the specimen was placed sidewise in an ultrasonic bath and cleaned for 10 minutes in DI water followed by 10 minutes in acetone, then allowed to air dry for a minimum of 2 hours.

To produce usable Ti6Al4V titanium alloy substrate, it was critical to control the specimen's temperature by careful adjustment of the microwave input power and simultaneous monitoring using an infrared thermometer. The microwave induced plasma operating at a wavelength of 0.73 nm and power that ranged from 0.1 to 1.5 KW

was used in the deposition process. At higher microwave powers, parameters were established to ensure deposition and adhesion characteristics. Other process parameters (e.g., flow rate, etc.) were initially based on prior LIMB system operating experience. The initial plasma burns of hydrogen (zero grade, 99.998% pure) at a pressure of 70 Torr was allowed to run for 30 minutes, followed by the introduction of ultra-high purity methane (99.97%). Once both gasses entered the chamber, individual flow rates were controlled to achieve a specific methane percentage (i.e., 1%, 3%, or 5%) (CH_4 and H_2 amount per unit time). The ideal flow rate and temperature were set such that the underlying substrate and holder was not adversely affected. All samples were fabricated in a controlled hydrogenated vacuum atmospheric chamber. The CVD exposure times that ranged from 1 to 4 hours depending upon the specific processing parameter being employed. The detailed MPACVD procedure, as defined in Appendix A, requires 5 to 9 hours to complete.

The 23-sample specimen listed in Table 4 were fabricated using the LIMB system. Table 4 shows sample specimen for eleven different combination of deposition parameters. A subset of these samples was selected for further analysis in support of this theses stated goals and objectives. From Table 4, samples 5A, 8A, and 9A are examined using a variety of physical techniques, such as surface light microscopy, surface SEM, etc.

Table 4. Fabricated Candidate Specimen

Candidate Sample		Fabrication/design Parameters		
index	Sample Designation	Temperature (°F)	Methane Concentration (%)	Time (Hours)
1	1A	990	2	4
2	2A	1040	5	4
3	3A	1040	5	4
4	4A	990	5	2
5	5A	1040	5	4
6	6A	990	5	2
7	7A	990	2	4
8	8A	1040	5	4
9	9A	1040	2	2
10	10A	1040	2	2
11	1B	1000	3	1
12	2B	1000	3	4
13	3B	1000	5	2.5
14	4B	700	3	4
15	5B	850	5	1
16	1C	1000	3	1
17	2C	1000	3	4
18	3C	1000	5	2.5
19	4C	700	3	4
20	5C	850	5	1

21	6C	850	1	1
22	7C	850	3	2.5
23	8C	850	3	2.5

3.1.1 Materials and Methods: Specimen Processing

Specimens are sectioned on a low-speed diamond saw. After the blade is secured, the water bath is filled with tap water. Then the sample is secured such that the newly created surface is perpendicular to the blade. The sample is carefully lowered onto the rotating cutting wheel so as not to damage the sample or the blade. Weights were used sparingly because they caused the cutting wheel and the sample to bind.

After the samples were cut, they were mounted in a copper powder. Hot compression mounting requires that the sample be heated and cooled under pressure. The mounting of the samples was such that the cross-section was visible for microscopy.

3.1.2 Visualization of Specimen Surface

Microscopy: Surface light

Sample 9A was processed for two hours at 1040°K and 2% methane concentration. The surface of the processed samples (Figure 19) exhibits a texture visible to the naked eye with grain-like features approximately four mm in size that are regularly distributed across the entire face of the sample. The features are visible on all samples processed

with methane. To determine if the features were merely the result of a plasma etching process, a sample was processed without CH_4 , the precursor for the CH_3 growth species. With only hydrogen plasma, the features were not present.



Figure 17. Sample 9A coating and at scale

Under five times magnification (Figure 17), the grain-like features are clearly visible. Here we see that the grain size exceeds any visible defect size. We therefore expect grain size to be a significant factor in the mechanical strength of the film. With ultra-pure Al_2O_3 and Ti_2SiC_2 ceramics a decrease in grain size is associated with an increase in film strength in accordance with the Hall-Petch relation. [38][48] However, this relation only holds for grain sizes less than 10 nanometers beyond that grain boundaries start to slide. [39] [49]

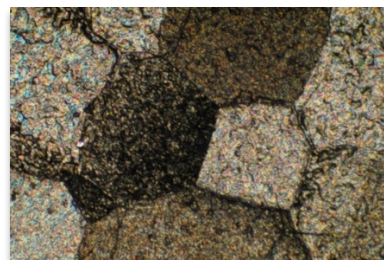


Figure 18. Sample 9A 40X magnification

It has been observed that the size of grains has a significant effect on fracture behavior. As grain size of ceramics increases, fracture mode changes from intergranular to transgranular. With an increase in grain size, grain boundary area decreases allowing cracks to propagate across grains. In some ceramics it has been shown that fracture toughness increases with increasing grain size. [38][48]

The effect of increasing grain size on the hardness have been mixed. Hou et al. measured microhardness of Yb doped $(Y_{0.97}Zr_{0.03})_2O_3$ ceramics. An increase in grain size resulted in a decrease in hardness.[40][50] In contrast, He et. al. showed an increase in piezoelectric ceramic hardness with increasing grain size. [41][51]

Surface SEM

Under a scanning electron microscope, the surface (Figure 19) appears to be crystalline with evenly distributed nanocrystalline features. Secondary to the existence of crystalline features are the existence of holes or “pores”. The microstructural analysis demonstrated that some porosity exists in the microwave deposition integration zone. Their formation most likely depends upon the plasma’s relationship with the substrate. It is reasonable to expect that the density of these pores will vary based on the conditions of the chamber. These defects are of great concern due their effects on the material’s mechanical properties. Porosity occurs with less frequency than nanocrystalline

features and are hard to distinguish with the naked eye. However, porosity does have an impact on material strength. Under stresses, pores (particularly those with close proximity to the sample specimen surface) serve as stress concentration and crack initiation sites, which may lead directly to specimen failures. Minimization and evaluation of these defects is a major concern in the fabrication of deposited specimens.

Under higher magnification ([Figure 19](#)), the characteristics of the

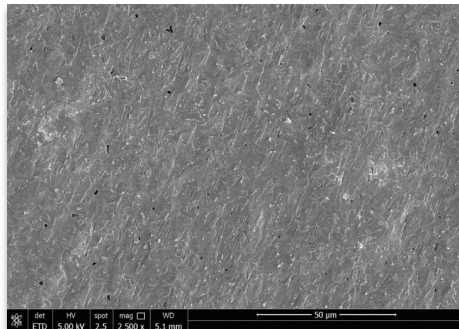


Figure 19. SEM imaging of sample 9A (2500X)

surface is easier to visualize. The surface itself appears to be composed of needle-like channels. There are nanocrystalline growths ([Figure 20](#)) having very small pores dotting the surface.

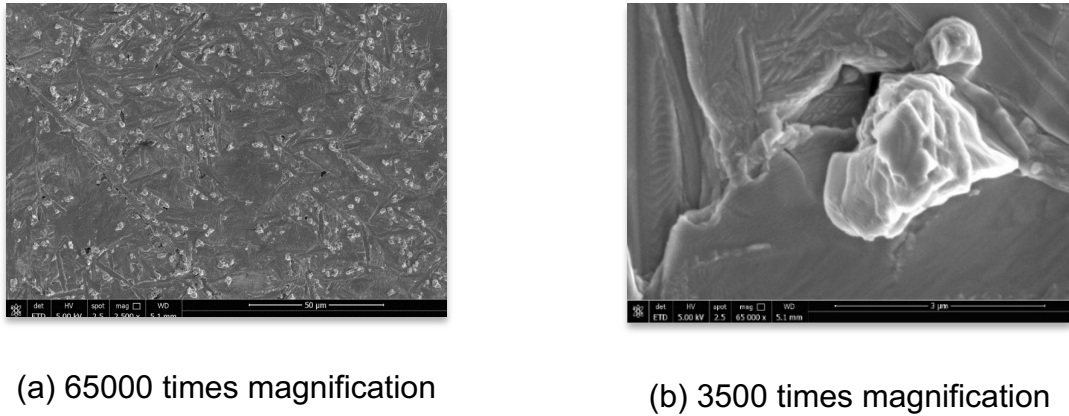


Figure 20. SEM imaging of sample 9A

When looking at the substrate/FGM boundary, it was found that there is good adhesion between layers. The phase intensity increased from the substrate to the outer surface of FGM. Carbide was present in the structure as separate inclusions. XRD analysis revealed reactions (as demonstrated by the integration zone) between the components of the composite layers. The surface roughness was typical of a thermal deposition process.

Threshold imaging

To get a statistical description of the surface and its features we use Imagej software and Otsu's Method. In image processing, the Otsu's Method is used to perform automatic image thresholding. This means that the algorithm separates pixels into two classes; foreground and background. This is done by methodically searching for the threshold that minimizes the intra-class variance or the weighted sum of variance of the

two classes. The following expression is used by the software to produce the resultant images.

$$\sigma_w^2(t) = \omega_0(t)\sigma_0^2(t) + \omega_1(t)\sigma_1^2(t) \quad (8)$$

where ω_0 and ω_1 are the probabilities of the two classes separated by a threshold, t , and σ_0^2 and σ_1^2 are the variance of these two classes. For the two classes, minimizing the intra-class variance is equivalent to maximizing inter-class variance.

Imagej ithe process is used to evaluate image thresholding. Imagej begins by setting the image scale of Figure 21. Once set, the foreground and background is determined based on the histogram generated. The goal is to isolate the nanocrystalline features.

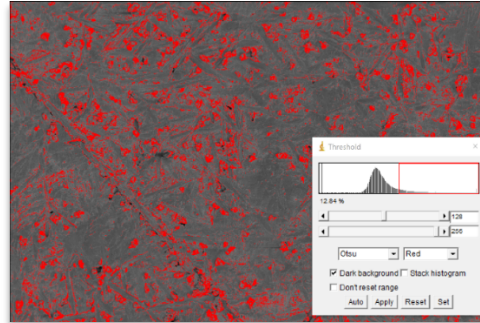


Figure 21. Image thresholding

The grey scale image (Figure 21) is turned into a black and white image with the black being the features of interest (Figure 22).

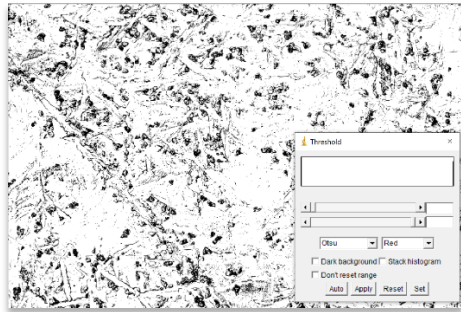


Figure 22. Black and white image

In order to better visualize the target features, the mask is refined based on expected size of the particles of interest ([Figure 23](#)).

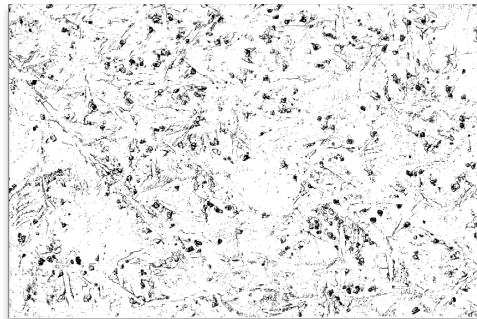


Figure 23. Highlighted features

Based on the application of the refined mask, the image of the specimen surface is summarized as shown in Figure 24.

Slice	Count	Total Area	Average Size	%Area	Mean
sample 9a 2500[4331].tif	16823	1595793423.085	94857.839	8.182	255

Figure 24. Summary statistics

From the summary **shown in Figure 24**, we can see that the nanocrystalline features are 95,000 nm² on average and cover approximately 8% of the samples surface area. We determine the samples porosity in a similar fashion. The threshold image for the pores in the sample is shown in Figure 25.

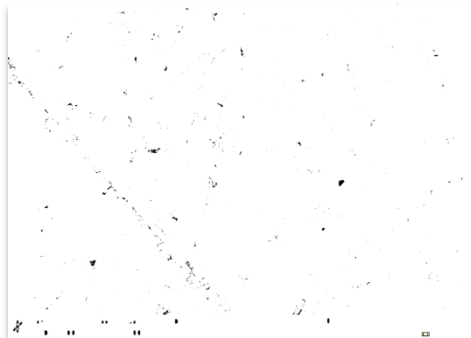


Figure 25. Highlighted pores

From the summary **provided in Figure 26**, we can see that the average pore size is 89,000 nm² and pores represent 0.36 % of the surface area.

Slice	Count	Total Area	Average Size	%Area	Mean	
sample 9a 2500[4331].tif	798	71063632.623	89052.171	0.361	255	

Figure 26. Pore summary statistics

Cross section light

A composite sample specimen (designated 9A) was processed over four hours at a temperature of 1040°F at 5% methane concentration is shown in Figure 27. Sectioned and mounted samples were examined under 30- and 40-times magnification. Figure 30 shows the unprocessed sample's cross-section. On the right the dark copper mounting material is visible. And the light grey on the left is the sample substrate.



Figure 27. An unprocessed sample cross section

Below in Figure 28, we observe sample 5A under 40 times magnification. A new feature is visible; a porous region about 50 microns thick can be seen. This is the newly created surface/ film. Below this film is the region of interest. There are no visible changes here, at least not under a light microscope but further testing reveals an “integration zone” does exist here.

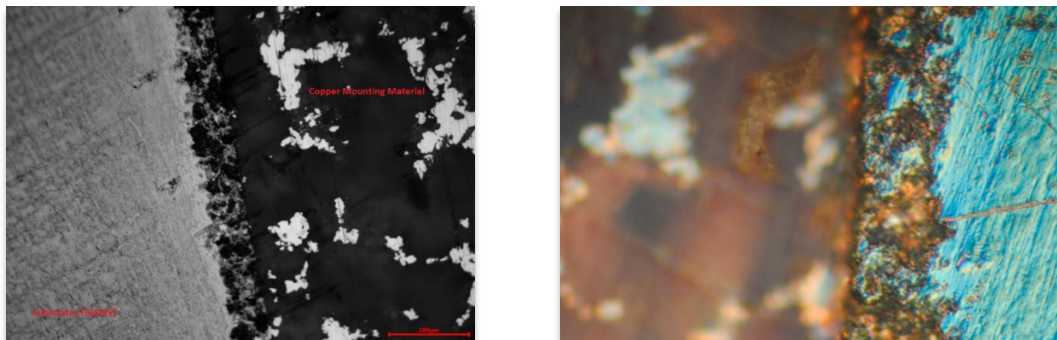


Figure 28. Sample 5A at 40 times magnification

XRD

X-ray diffraction analysis was done using Cu-K α radiation for the phase characterisation of the novel surface created using MPACVD. As expected, the XRD patterns indicated the presence of both Ti64 and TiC.

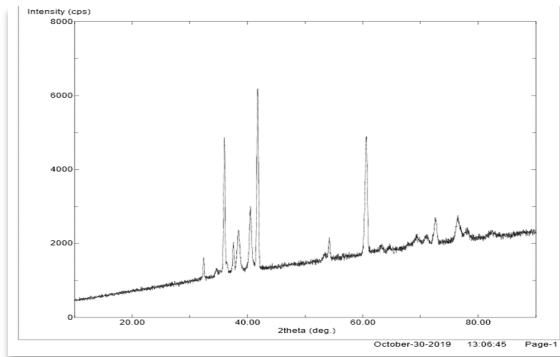


Figure 29. **Sample 5A XRD** patterns

Knowing we have TiC comprising our novel surface allows us to make certain assumptions about its performance characteristics. TiC is known to be extremely hard, heat resistant, and durable and insoluble in water. [42]53] Additionally, TiC has a very low coefficient of friction. These properties make it a very good candidate for the bearing surface of joint replacements.

3.1.3 Specimen Characterization: Surface Microhardness

Vicker's Approach

Hardness testing is particularly effective for rapidly mapping local mechanical properties along a composite's surface. Thus, providing a first-order assessment of its properties. Microhardness testing has been the common first approach for assessing mechanical properties. Not only does this testing require minimal sample preparation, but it is capable of resolving the spatially varying properties characteristic of a layered

composite specimen. A fully manual Vickers indenter was employed to conduct microhardness testing. The nature of the manual indenter required indents to be measured by hand with an optical microscope.

Generally, Vickers microhardness testing is a non-destructive small-scale method for determining the hardness of a specimen. During a Vickers test, a small load is applied to a standardized diamond indenter having a square-based pyramid and a fixed angle (Figure 30). The angle is such that the hardness value will be constant regardless of load. The diagonal lengths of the indent impression on the polished surface is measured

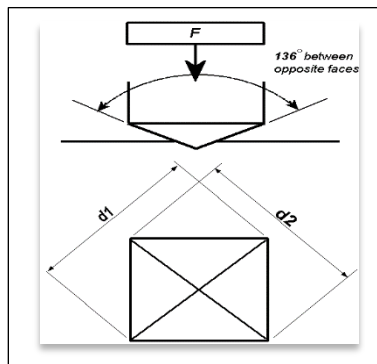


Figure 30. Vickers diamond indenter

through a microscope. The hardness value, HV, can then be calculated by plugging the lengths into equation 9.

$$HV \approx 0.1891 \frac{F}{d^2} \quad [kgf/mm^2] \quad (9)$$

where F [kgf] is the force applied with the indenter, and d [mm] is the average length of the indent diagonal. The resulting hardness value, HV (also referred to as VHV), has units of kgf/mm². In addition to nominal hardness values, Vickers indentation can be used to determine the composition ranges within which brittle intermetallic phases are likely to be present. Extremely high hardness values and the presence of cracks radiating from the indent corners are indicative of hard, brittle material.

Table 5 provide the HV for some common materials. In Table 5, the first number is the hardness value; the letters following the first number indicate the hardness scale (Vickers); and the last number indicate the test load in kilograms.

Table 5. Typical hardness values for some common materials are listed below [45][46]

Material	Hardness Value
316L stainless steel	140HV30
347L <u>stainless steel</u>	180HV30
<u>Carbon steel</u>	55–120HV5
<u>Iron</u>	30–80HV5
<u>Martensite</u>	1000HV
<u>Diamond</u>	10000HV

The indenters employed in this effort were calibrated using standard samples. The sample copper “puck” was inserted into and leveled in the iNano system. The target Berkovich indenter tip indentation depth was set to 100 nm and 500 nm with a target load of up to 45 mN (this load is never actually reached). The mechanical properties of a specimen’s surface was determined using 20 indents each separated by 100 microns

As stated earlier, candidate samples fabricated in support of this thesis at various operating parameter settings within the LIMB system. Table 4 indicates that the data presented in Figure 31 was obtained for sample 8A having a four-hour material substrate deposition time at a temperature of 1040°K and a 5% methane concentration. Four different distinct hardness tests were conducted on this sample. Figure 31 shows the result of Vicker’s hardness conducted on candidate sample 8A. The Vickers values ranged from 434HV0.5 to 652HV0.5. The control used during these tests ranged from 335HV0.5 to 356HV0.5

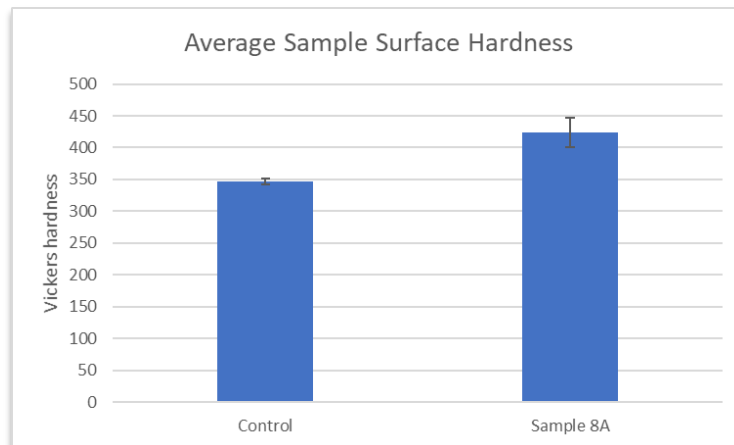


Figure 31: Sample 8A surface microhardness

According to Figure 31, sample 8A is approximately 22% harder than the as received material. It is important to note that indenter sizes on the same order of the composite film's thickness will likely have an influence on the substrate's hardness measurement. That is to say, the film may be much harder than indicated by its given measurement.

When it comes to thin film, Vickers hardness may not be the best method to use. Nano-indentation may be more appropriate. There have been efforts to assess the correlation between Vickers and nanoindentation. [%.. T. Sawa, "Correlation between Nanoindentation Test results and Vickers Hardness," IMEKO-TC5-2010 Conference, pp171-174, 2010]. It was concluded that a correlation exists for some materials, that correlation is inconsistent when considering a broad range of materials. For the materials assessed, the correlation indicated that nanoindentation was on the order of 1 to 2 (resin to copper) times that of Vickers. Due to the inconsistencies, nanoindentation will be used as an alternative hardness testing method for characterizing LIMB fabricated thin-film specimen.

3.1.4 Specimen Characterization: Surface Nano Hardness

Nanoindentation Approach

When evaluating the hardness of small-scale gradient material, nanoindentation is very useful. Nanoindentation, also referred to as depth sensing indentation differs from micro indentation in several ways. The most obvious being the indentation scale. With nano

indentation the scale is generally several orders of magnitude smaller than micro indentation. Also, where micro indentation measures the area of the residual impression, nanoindentation measures the depth of penetration. With nanoindentation the area of contact at full load is determined by the depth of the impression and the known angles of the indenter. The scale and versatility of nanoindentation give us our first opportunity to explore the mechanical properties of the substrate/ film interface. We suspected that the transition from substrate to film wasn't homogeneous, rather we anticipated that was a heterogenous mix of multiple phases.

All nano indentation was performed on [Nano Mechanic's indenter](#). Figure 32 shows many different types of indenters used in nano indentation. One of the most commonly used is the Berkovich tip because it's three-sided geometry is easier to grind to a very sharp point. This fact makes the Berkovich tip appropriate to use in the present study.

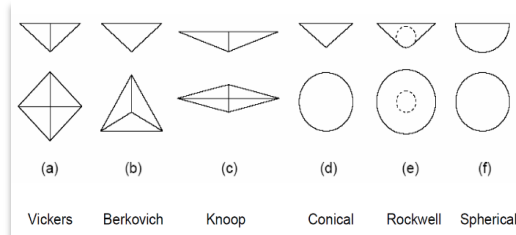


Figure 32. Types of indenters used in nano indentation

There are many analytical models available, but this thesis assumes the Pharr, Oliver, and Brotzen nanoindentation model. The basic concept and assumptions required for all the models are essentially:

- Deformation upon unloading is purely elastic
- The compliance of the sample and of the indenter tip can be combined like springs in a series:

$$\frac{1}{E^*} = \frac{1-v_i^2}{E_i} + \frac{1-v_s^2}{E_s} \quad (10)$$

where, E_r is the reduced or combined modulus and E_i is the modulus of the indenter.

- The contact can be modeled using an analytical model for contact between a rigid indenter of defined shape with a homogeneous isotropic elastic half space:

$$S = \frac{dP}{dh} = \frac{2\sqrt{A}}{\sqrt{\pi}} E_r \quad (11)$$

where, S is the contact stiffness and $A = 3\sqrt{3}h_p^2 \tan^2 65.3 = 24.5h_p^2$ is the contact area.

For hardness, given by $H = P/A$, the elastic modulus in terms of the known radius of the punch becomes:

$$E^* = \frac{dP}{dh} \frac{1}{2h_p} \frac{1}{\beta} \sqrt{\frac{\pi}{24.5}} \quad (12)$$

where, $\beta = 1.034 f$ for the Berkovich indenter. Figure 33 shows typical loading cycle for nanoindentation. The characteristic loading and unloading curve are depicted in Figure 34.

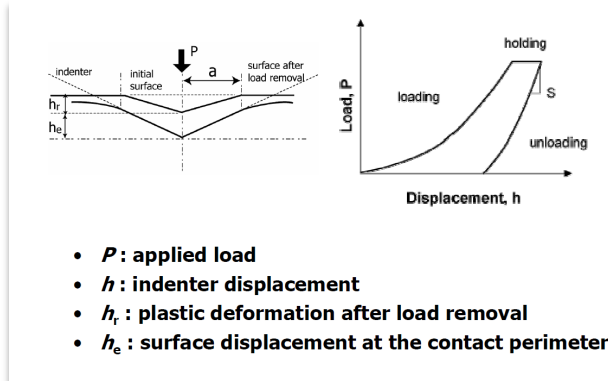


Figure 33. Typical nanoindentation loading cycle

Pharr, Oliver, and Brotzen has shown that the loading cycle identified in Figure 34 applies to all axial-symmetric indenters. Specifically, it applies to the Vicker's indenter being used in support of this thesis work. The contact stiffness of Equation 11 as depicted in Figure 34, shows that the slope of the unloading curve is proportional to the elastic modulus and may be calculated from the known radius of the punch. From Figure 34, the first time the sample material is loaded, the stress and strain rise along the loading curve towards the peak. Once the load is relaxed, the material's response follows the unloading curve. However, if the elastic limit is exceeded, only the elastic portion recovers; a permanent residual strain persists in the material corresponding to

the residual strain. Thus, if the material is again loaded, its response will rise along the unloading curve and tail off to the right on the peak is reached.

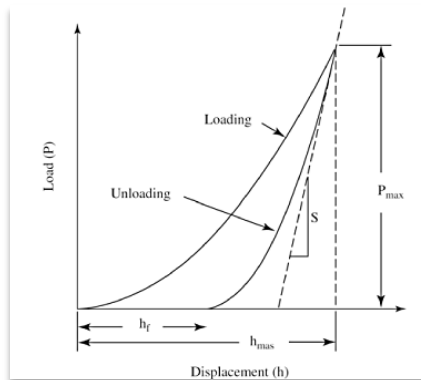


Figure 34. Load Displacement

Figure 35 show that the hardness of the sample is more than twice that of the control at 500 nanometers. This indicates that our previous micro indentation measurements were influenced by the soft substrate. At 500 nanometers, we are far less likely to be measuring the harness of the substrate considering that our previous estimate of film thickness was about 30 to 50 microns.

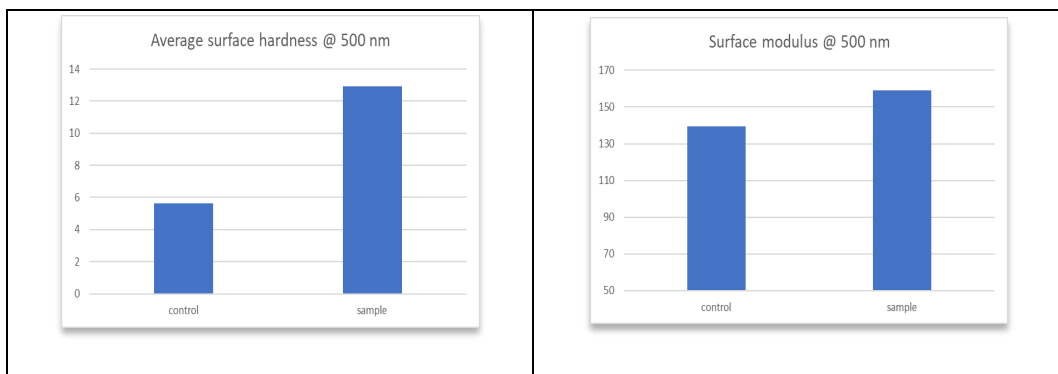


Figure 35. Nano indentation hardness measurements

Composite Material Interface Characterization

The characterization of the interface (i.e., integration zone) between composite materials can be accomplished using grid based nanoindentation and statistical deconvolution of experimental data. Grid indentation relies on a large array of nanoindentation to extract the mechanical properties of individual components.

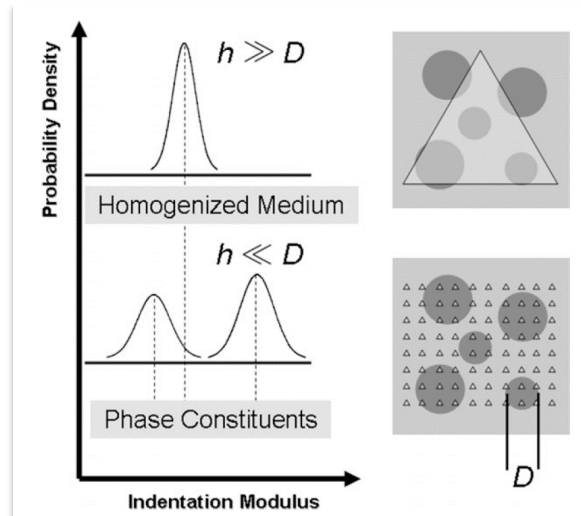


Figure 36. Illustration of grid-based indentation

Figure 36 illustrate the power of grid-based indentation. While large indents are unable to parse the difference between different phases of materials, the grid-based technique can. Assuming that the distribution of the mechanical property of each phase can be described by a Gaussian distribution (Figure 36), grid indentation yields a multimodal probability function that allows determination of properties of each phase. If we assume

that the only source of property variation in our sample is random it is also reasonable to assume that that the distribution of properties in each phase is approximately Gaussian. Deconvolution is performed using a software program (i.e., Doconvolution.m written in Matlab code) whose statistical deconvolution algorithm is described as follows:

Let N^{exp} represent the number of measurements taken and used to construct a histogram using equally spaced N^{bins} of size b . Each bin is assigned a frequency of occurrence f_i^{exp} that is then normalized with respect to the overall number of measurements. Using these elements, we can compute the experimental probability density function (PDF) (Figure 37):

$$P_i^{exp} = \frac{f_i^{exp}}{N^{exp}} \frac{1}{b} \quad (13)$$

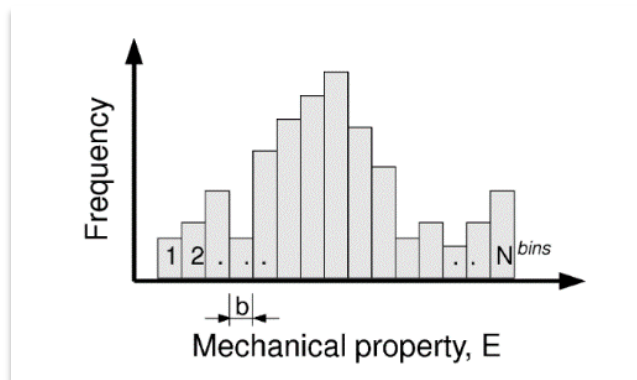


Figure 37. Experimental probability density function

Deconvolution involves finding PDFs for individual phases in our global histogram. The PDF for individual phases can be written as:

$$p_j(x) = \frac{1}{\sqrt{2\pi s_j^2}} \exp \frac{-(x-\mu_j)^2}{2s_j^2} \quad (14)$$

Where μ_j and s_j are the mean value and standard deviation of the j-th phase.

$$\mu_j = \frac{1}{n_j} \sum_{k=1}^{n_j} x_k, \quad (15)$$

and

$$s_j^2 = \frac{1}{n_j-1} \sum_{k=1}^{n_j} (x_k - \mu_j)^2 \quad (16)$$

Then x is the approximated quantity, in our case x is the modulus. The overall PDF can be written as:

$$C(x) = \sum_{j=1}^M f_j p_j(x) \quad (17)$$

where, f_j is the volume fraction of a single phase.

$$f_j = \frac{n_j}{N_{exp}} \quad (18)$$

The individual distributions can be found by minimizing the following error function

$$\min \sum_{i=1}^{N^{bins}} [(P_i^{exp} - C(x_i)) P_i^{exp}]^2 \quad (19)$$

Materials and methods: Deconvolution of Grid based Nanoindentation

Each individual indent was performed in accordance with the procedure previously outlined for individual nanoindentation. The distinction here is that indents are: (a) performed in a grid pattern; (b) performed on the cross section of the sample; and (c) the max depth was set to 100 nm rather than 500 nm. Indents are performed in 5 rows of 30 for a grand total of 60 indents in a grid pattern. The distance avoids overlap between adjacent interaction volumes. To increase spatial resolution beyond this value, staggered lines of indents could be made along the composition gradients.

Results of Deconvolution of Grid based Nanoindentation

The cumulative PDF generated by the algorithm is shown in Figure 38. We detected two individual phases. Phase 1 is centered around 122 GPa and is in agreement with what we'd expect to see for the modulus of the substrate material Ti6Al4V. There is a second peak centered around 152 suggesting the presence of hardened deposits beneath the surface film.

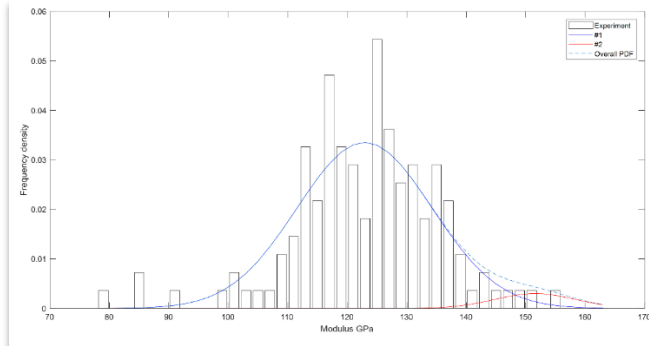


Figure 38. Cumulative PDF generated by the algorithm

AFM

Analysis of the composite requires a means of imaging the material surface. To perform this function, Atomic Force Microscopy (AFM) is the best choice since it overcomes the limitation of techniques such as Scanning Tunnelling Microscopy (STM); AFM is able to image conducting or semiconducting sample surfaces from ceramics to biological AFM system (Figure 39) works by raster-scanning an extremely sharp tip over a surface. Atomic forces are used to map the tip-sample interaction. AFM techniques exist for most measurable force interactions: van der Waals, electrical, magnetic, thermal. Each of these techniques requires special calibration and tip selection.

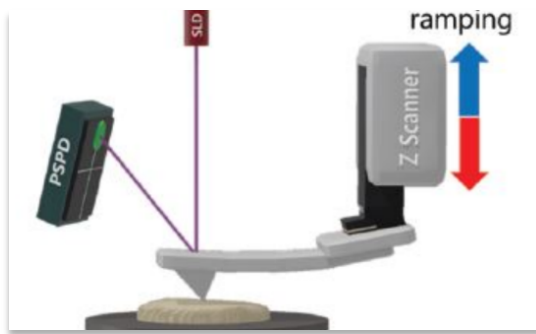


Figure 39. AFM raster-scanning

Often AFM is used to probe the nanomechanical properties of a surface. Force-Distance (FD) curves ([Figure 40a](#)) are used to study properties such as Youngs modulus and adhesion with nanometer resolution. In FD spectroscopy, the cantilever is used as force sensor. The approach and retraction curves of the cantilever deflection versus the movement of the Z scanner can be converted into FD curves ([Figure 40](#)) that contain information on nanomechanical properties of the sample at a given location. At distances on the order of several micrometers, electrostatic forces represent long-range interactions. Attractive van der Waals forces and capillary forces, in air only, are common at tip-sample-distances up to a few nanometers. Once the tip is in contact with the sample, repulsive Pauli interaction controls the acting forces between the tip and sample. As the tip retracts from the sample surface, the cantilever bends towards the surface due to the adhesion force. Getting usable force curves and analyzing said curves is a science of its own.

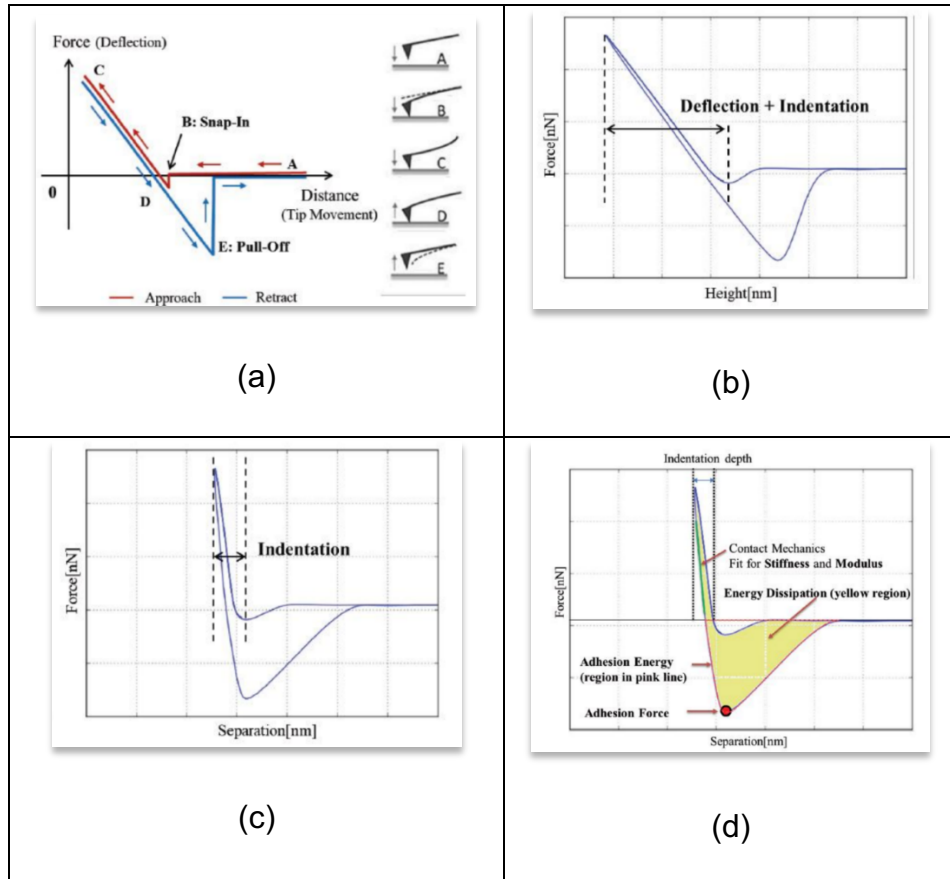


Figure 40. Force deflection curves

FD curves used to study material properties with nanometer resolution.

In Figure 40b, height refers to the position of the Z scanner during the FD measurement, and separation (Figure 40c) is the tip position with respect to the sample surface. This correction for the cantilever deflection is important for quantitative elasticity measurements, which are based on the indentation of the tip in the sample surface. These measurements require an accurate separation of deflection and indentation and, therefore, the conversion of height to separation between the tip and the sample.

Figure 40d shows how various mechanical properties can be obtained from the separation force curve.

Fast force mapping

As discussed previously, in addition to generating information about a sample's topography, AFM can also be used to generate information about nanomechanical information. And we can also map these properties onto high resolution images of the sample's surface. Such 2D arrays can give valuable information about the samples overall make up. Unfortunately, acquiring force curves can be a time-consuming process. Fast Force Mapping (FFM) is a proprietary technique developed by Asylum Research for their AFM machines which dramatically increases the acquisition speed of force curves (up to 1000Hz).

All measurements were taken with an AFM (with tip) operating at a frequency of 300khz, a spring constant of 40 N/m, and a of length 125 micrometers. Samples were sectioned and superglued to a standard 12mm AFM/STM sample mount. Images of nanomechanical properties as a function of position were generated using the AFM's proprietary FFM mode.

Profile

To construct a profile representing the transition from hard film to soft substrate a code is written to analyze images. From the image depicted in [Figure 41](#), we see that the transition has a composite-like structure where there are spots of hard material and spots of soft material with varying frequency. The left side of the image is closer to the surface of the sample and the right side ends approximately 30 microns into the sample cross-section. It's not immediately obvious that there is a gradient at all. This is where Hardstuff.m ([Appendix C](#)) written in MATLAB finds its utility.

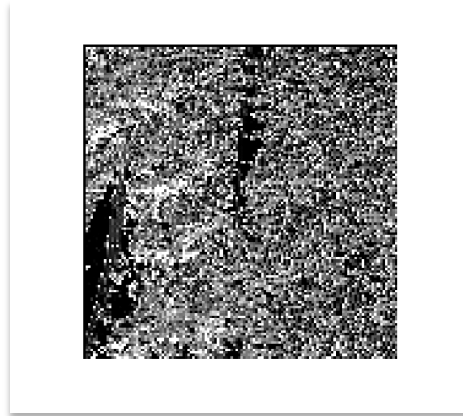


Figure 41. The hard film to soft substrate deposition profile

First the program breaks the AFM image into a matrix of 64 equally sized square blocks (Figure 42).

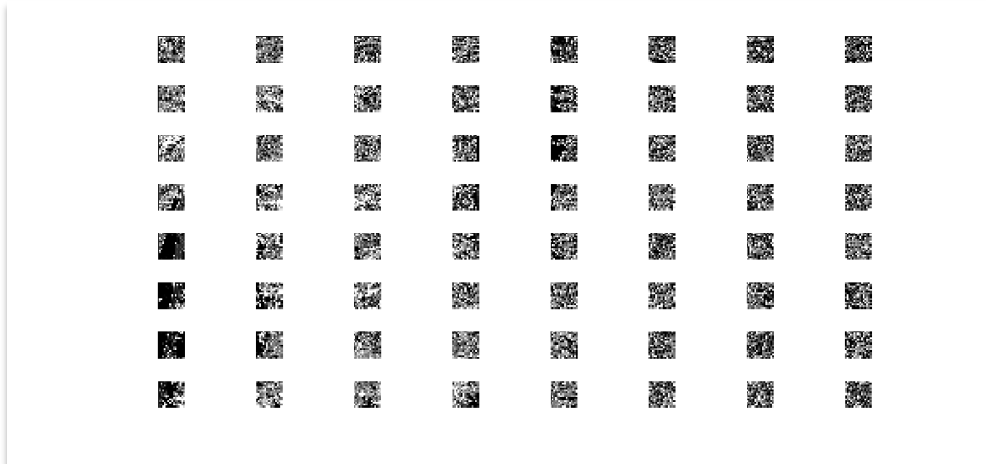


Figure 42. Sample image deposition matrix

Then it stacks the columns vertically. The program, based on a predetermined threshold, determined the ratio of hard spots (white) to soft spots (black). This process is much like the threshold image analysis discussed earlier in this thesis. Once this is completed, the program plots the fraction of hard to soft material (**Figure 43**).

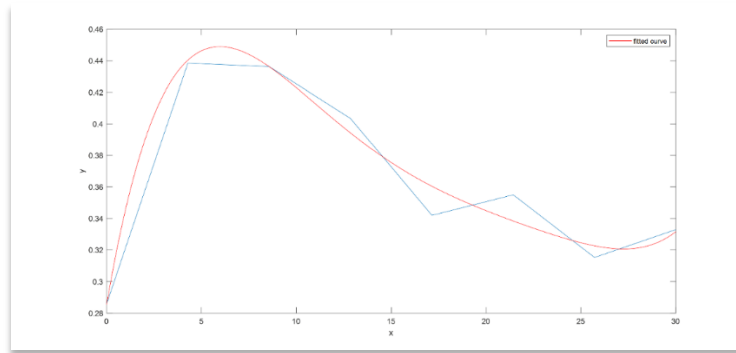


Figure 43. Computed fraction of sample image hard versus soft material

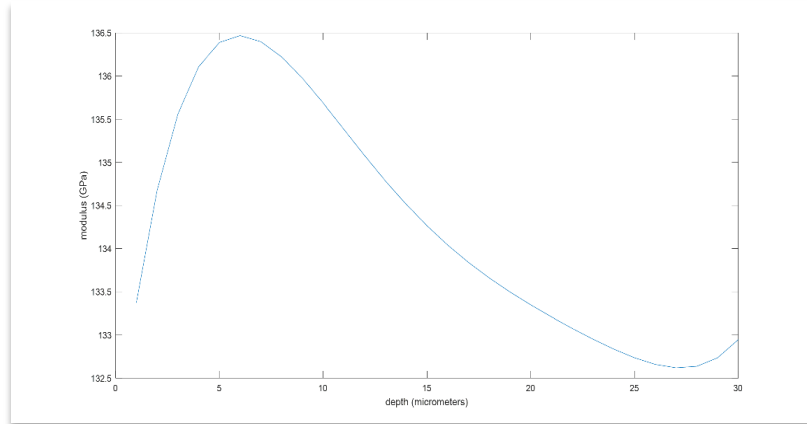
It's immediately apparent from the shape of the curve that there is a gradient in the image. To facilitate generalized analysis, the data is computationally fitted to a smooth polynomial curve. Specifically, for the sample noted above, the polynomial curve (Figure 43) was determined to be:

```
profile3 =
Linear model Poly5:
profile3(x) = p1*x^5 + p2*x^4 + p3*x^3 + p4*x^2 + p5*x + p6
Coefficients (with 95% confidence bounds):
p1 = 1.908e-07 (-6.799e-07, 1.061e-06)
p2 = -1.749e-05 (-8.305e-05, 4.807e-05)
p3 = 0.0006191 (-0.001123, 0.002361)
p4 = -0.01027 (-0.02951, 0.008973)
p5 = 0.07015 (-0.007529, 0.1478)
p6 = 0.2852 (0.2014, 0.3691)
```

The coefficients of the polynomial are given with their 95% confidence interval. The Rule of Mixtures for composite materials can be applied to estimate the combined modulus as a function of depth. The Rule of mixtures is given by:

$$E_c = fE_f + (1 - f)E_m \quad (20)$$

where E_f is the elastic modulus of the **candidate carbide** fiber material (hard stuff) and the E_m is the modulus of the substrate matrix material (soft stuff), **and the volume function $f = [\frac{(z+1/2)}{h}]^n$** . The result of applying equation 19 is shown in Figure 44.



$$z \approx 5.724 \times 10^{-6} x^5 - 0.0005247 x^4 + 0.018573 x^3 - 0.03081 x^2 + 2.1045 x + 131.556 \quad (\text{max } = 136.468 \quad \text{Min } = 132.629)$$

Figure 44. Actual polynomial curve fit for sample image

3.2 Assessment of Computational Adhesion

Molecular Dynamics Modeling

Molecular dynamics (MD) simulations are not new. MD simulation was used to study the effect of the intrinsic interlayer on the diffusion bonding of the composite material. That is, MD simulations predict how every atom in a molecular system will move over time, based on a general model of the physics governing interatomic interactions. We start with a given number of atoms whose initial position and velocity are known. We then use information about the interatomic energies and newtons laws of motion to make predictions about the molecular system's atomic motion.

The atomic interactions between atoms are formulated using the empirical embedded atom method (EAM) potential [1]. The EAM provides a realistic approximation of real-world processes regarding the structural and thermodynamic properties of materials. EAM provides a good depiction of the metallic bonding that occur in fabricated candidate specimens. The models of both material alloy are put together inside a simulation box with dimension 47.13x75.67x158.32 nm (the z -direction is perpendicular to the composite interface). The contact surface between the TiC and TiAl alloy is the plane (0 0 1). There are 34,000 atoms in the model of the composite. All molecular dynamics simulations are carried out by the Large-scale Atomic/Molecular Massively Parallel Simulator (LAMMPS) [47] [*.] and post-processing the atomistic data obtained from MD simulation is performed by the Open Visualization Tool (OVITO) [??]. LAMMPS is an open-source package that runs on a single processor or in parallel. LAAMPS supports solid state materials (i.e., metals) and soft material such as biomolecules and polymers. Through LAAMPS visualization of the atomic motion we can derive bulk properties of composite materials like pressure and stiffness.

A statistical description of the surface and its features was obtained using Imagej software and Otsu's Method. In image processing, the Otsu's Method is used to perform automatic image thresholding. In order to analyze the image profile's transition from hard film to the soft substrate, it was necessary to develop some custom code. This is where Hardstuff.m (Appendix C) written in MATLAB finds its utility.

The second thesis objective (i.e., specific aim) is to explore the theoretical adhesive properties of a functionally graded interface. We have previously established that the novel candidate textured surface is primarily composed of TiC and that the transition to substrate is graded. The graded constituents vary according to the expression shown in Figure 44. In the current section we use this information and computational tools to explore the theoretical adhesive properties of a sample we created.

Until this point, we have explored the properties of the LIMB novel candidate surface and its interface at a macro-scale, meso- scale, and even a nano scale using (Figure 45) various technologies (i.e., SEM and AFM data). For this virtual assessment, we use atomistic simulation or more commonly MD information about the bulk properties of experimental specimens.

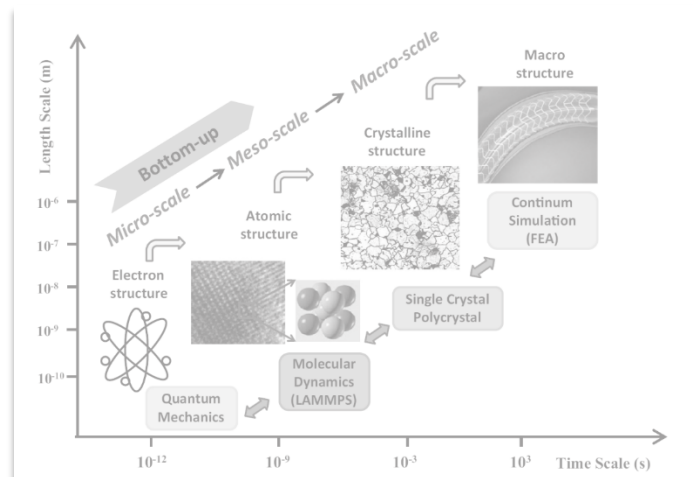


Figure 45. Structural variability of molecular dynamics

The purpose of this experimentation is to conduct a virtual pull off test, wherein we literally pull the carbide film from the Ti64 substrate and measure the force required to do so. In order to accomplish this task, we construct a model based on what is known about the substrate film's dynamics. More specifically, we create two models. The first is based on the presumption that the substrate film interface is laminated; thus, represented by two flat layers. The second is based on what we believe is a more realistic assumption that the interface is mixed, with a gradual transition from film to substrate. The question to be answered is which scenario yields the better adhesion.

3.2.1 Application of Molecular Dynamics Technique

In molecular dynamics we start with a material representation whose given number of atoms have an initial position and velocity that is known. We then use information about the interatomic energies and newtons laws of motion to make predictions about material's atomic motion. From the atomic motion, we can derive bulk properties like pressure and stiffness.

Fundamentally, a molecular dynamics simulation consists of the numerical solution of the classical equations of motion. These equations are written as:

$$m_i \ddot{r}_i = f_i \quad f_i = -\frac{\partial}{\partial r_i} U \quad (21)$$

These equations imply that we need to calculate the force, f_i , acting on the atoms (N atoms). The force is the gradient of the energy U ; where r represent the complete set of $3N$ atomic coordinates. **These interactions are depicted in Figure 46.** The non-bonded interactions between atoms is generally split into 1-body, 2- body, and 3-body terms:

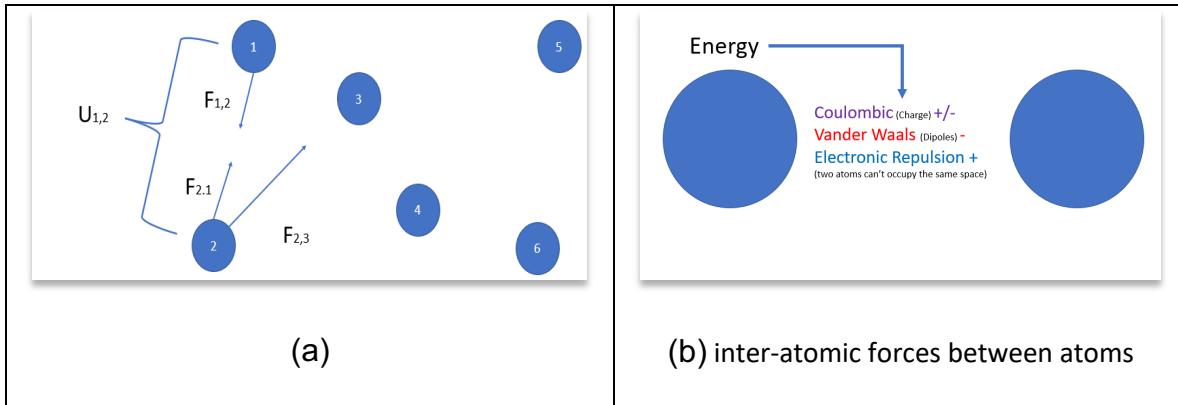


Figure 46. Conceptual system of atomistic energy supporting sample adhesion characterization

$$U_{non-bonded}(r^N) = \sum_i u(r_i) + \sum_i \sum_{j>i} v(r_i, r_j) + \dots \quad (22)$$

The term $u(r)$ represents an externally applied potential field, it is usually dropped for fully periodic simulations. In addition, it is frequently possible to neglect three-body interactions and concentrate on the pair potential:

$$v(r_i, r_j) = v(r_{ij}) \quad (23)$$

For illustration purposes we will examine the Lennard-Jones potential:

$$\nu^{LJ}(r) = 4\varepsilon \left[\left(\frac{\sigma}{r} \right)^{12} - \left(\frac{\sigma}{r} \right)^6 \right] \quad (24)$$

For a given diameter sigma and well depth epsilon, the Lennard-Jones potential was used in early MD studies to examine the properties of liquid argon. [43][54] Casual examination of the formula reveals that it has an attractive r^6 contribution (Vander Waals) and a repulsive r^{12} contribution (mostly electronic repulsion). The combined characteristic curve is shown in Figure 47.

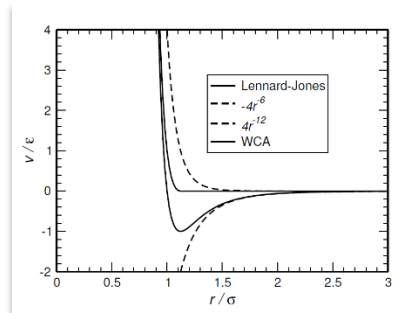


Figure 47. Interatomic potential graph

The interatomic potentials describe the potential energy surface of a collection of atoms and are fundamental inputs for the atomistic simulation. It may be noticed that the interatomic potential graph looks a lot like the force curve in AFM, this similarity comes

from the fact that the tip of the probe is subject to the same Vander Waals and electronic repulsion forces.

Key MD Simulation Design Parameters

As previously mentioned, selection of the interatomic potential is the most important part of developing an MD simulation. The interatomic potential describes how atoms of the material system interact with each other. For a material system with many different atom types, it is important to select an interatomic potential that can describe all the interactions between atom types. For this experiment, we have decided to focus on the alpha phase/TiC interaction because it is weaker than the beta phase/TiC interaction.

{REF}[55] In this material system we have Ti-Ti, Al-Al, C-C, Ti-Al, Ti-C, and Al-C interactions. Amongst the methods that can fulfill this requirement is the second-nearest neighborhood (2NN) modified embedded atom method (MEAM). This potential includes the second nearest neighbor atom interaction, allowing it to describe a wide range of metals and ceramics with different crystal structures. The energy of the system can be described by [44] [56]:

$$E = \sum_i [F_i(\bar{\rho}_i) + \frac{1}{2} \sum_{j \neq i} \phi_{ij}(r_{ij})] \quad (25)$$

This is the MEAM potential. The purpose is to show the relationship between the commonly used MEAM potential and the somewhat less popular but more accurate 2NN MEAM potential.

Here F_i is the embedding function required to place atom i of type ρ_i into the electron cloud, ρ_i is the background electron density at site i , and $\phi_{ij}(R_{ij})$ is the pair interaction potential between atoms i and j at distance R_{ij} . The embedding function has the form:

$$F(\bar{\rho}) = AE_c \left(\frac{\bar{\rho}}{\rho^0} \right) \ln \left(\frac{\bar{\rho}}{\rho^0} \right) \quad (26)$$

Here A is an adjustable parameter, E_c is the sublimation energy, and $\bar{\rho}^0$ is the background election density for a reference structure. Where the reference structure is a category of atomic arrangements generally taken as the equilibrium structure. The background electron density $\bar{\rho}_i$ is a combination of spherically symmetric partial electron density and angular contributions 1, 2 and 3 shown respectively below.

$$(\rho_i^{(0)})^2 = \left[\sum_{j \neq i} \rho_j^{a(0)}(R_{ij}) \right]^2 \quad (27)$$

$$(\rho_i^{(1)})^2 = \sum_{\alpha} \left[\sum_{j \neq i} \left(\frac{R_{ij}^{\alpha}}{R_{ij}^3} \right) \rho_j^{a(1)}(R_{ij}) \right]^2 \quad (28)$$

$$(\rho_i^{(2)})^2 = \sum_{\alpha, \beta} \left[\sum_{j \neq i} \frac{R_{ij}^{\alpha} R_{ij}^{\beta}}{R_{ij}^2} \rho_j^{a(2)}(R_{ij}) \right]^2 - \frac{1}{3} \left[\sum_{j \neq i} \rho_j^{a(2)}(R_{ij}) \right]^2 \quad (29)$$

$$(\rho_i^{(3)})^2 = \sum_{\alpha, \beta, \gamma} \left[\sum_{\alpha} \frac{R_{ij}^{\alpha} R_{ij}^{\beta} R_{ij}^{\gamma}}{R_{ij}^3} \rho_j^{a(3)}(R_{ij}) \right]^2 - \frac{3}{5} \sum_{\alpha} \left[\sum_{j \neq i} \frac{R_{ij}^{\alpha}}{R_{ij}} \rho_j^{a(3)}(R_{ij}) \right]^2 \quad (30)$$

where, $\rho_j^{a(h)}$ represents the atomic electron density from j atom and a distance R_{ij} from atom i.

The 2NN MEAM potential is derived from the MEAM potential which only considers the nearest neighbor interactions. R_{jk}^{α} is a component of the distance vector between i and j . These angular contributions are the chief difference between the MEAM potential and the EAM potential. And are responsible for the addition of the term ‘Modified’ to the Embedded Atom Method. They allow for the description of directional bonding as seen in covalent materials such as silicon and diamond.

The following is a way of binning the partial electron densities to give total background electron density:

$$\bar{\rho}_i = \rho_i^{(0)} G(\Gamma) \quad (31)$$

$$\text{where, } G(\Gamma) = \frac{2}{(1+e^{-\Gamma})} \quad (32)$$

Also,

$$\Gamma = \sum_{h=1}^3 t_i^{(h)} \left[\frac{\rho_i^{(h)}}{\rho_i^{(0)}} \right]^2 \quad (33)$$

$t_i^{(h)}$ is an adjustable parameter. The atomic electron density is given by:

$$\rho_j^{a(h)}(R) = e^{-\beta^{(h)}(R/r_e - 1)} \quad (34)$$

Here $\beta^{(h)}$ is an adjustable parameter and r_e is the nearest neighbor distance in the equilibrium reference structure. With the MEAM potential the energy per atom for the reference structure is derived from the universal equation of state by Rose et al [45] [57]

$$F[\bar{\rho}^0(R)] + \frac{1}{2} \sum \phi(R) = E^u(R) = -E_c(1 + a^*)e^{-a^*} \quad (35)$$

where, $a^* = \alpha(\frac{R}{r_e} - 1)$ (36)

and $\alpha = \sqrt{\frac{9B\Omega}{E_c}}$ (37)

It is important to note that $E^u(R)$ is the universal function for uniform expansion or contraction in the reference structure. B is the bulk modulus and Ω is the equilibrium atomic volume. With the MEAM potential S_{ij} is the many body screening function between atoms i and j . It is defined as the product of the screening factors, S_{ikj} due to all other neighbor atoms k ,

$$S_{ij} = \prod_{k \neq i,j} S_{ikj} \quad (38)$$

and,

$$S_{ikj} = f_c \left[\frac{(c - c_{min})}{(c_{max} - c_{min})} \right] \quad (39)$$

Here C_{\min} and C_{\max} are the limiting values of C where f_c is determined by:

$$f_c(x) = \begin{cases} 1, & x \geq 1 \\ [1 - (1 - x)^4]^2, & 0 < x < 1 \\ 0, & x \leq 0 \end{cases} \quad (40)$$

Taking the second nearest-neighbor into consideration, the energy per atom in the reference structure can be expressed as:

$$E^u(R) = F[\bar{\rho}^0(R)] + \left(\frac{Z_1}{2}\right)\phi(R) + \left(\frac{Z_2S}{2}\right)\phi(aR) \quad (41)$$

Z_2 is the number of second nearest- neighbor atoms and ‘ a ’ is the ratio between the second nearest neighbor distance and the first nearest neighbor distance.

For a reference structure of the crystal structure body and face (e.g., bcc or fcc) centered cubic, the background electron density is calculated as a function of first nearest-neighbor distance R :

$$\bar{\rho}^0(R) = Z_1\rho^{a(0)} + Z_2S\rho^{a(0)}(aR) \quad (42)$$

Introducing another pair potential $\psi(R)$ we can write:

$$E^u(R) = F[\bar{\rho}^0(R)] + \left(\frac{Z_1}{2}\right)\psi(R) \quad (43)$$

where,

$$\psi(R) = \phi(R) + \frac{Z_2 S}{Z_1} \phi(aR) \quad (44)$$

Now we can say:

$$\phi(R) = \psi(R) + \sum_{n=1} (-1)^n \left(\frac{Z_2 S}{Z_1}\right)^n \psi(a^n R) \quad (45)$$

Relevant constants (Table 6) for the 2NN MEAM where obtained from the literature[46]

[58]:

Table 6. 2NN MEAM simulation initialization parameters for singular systems

	E_c	r_e	β	A	$\rho^{(0)}$	$\rho^{(1)}$	$\rho^{(2)}$	$\rho^{(3)}$	$t^{(1)}$	$t^{(2)}$	$t^{(3)}$	C_{min}	C_{max}	d
Ti	4.87	2.92	1.10	0.66	2.70	1.00	3.00	1.00	6.80	-2.0	-12	1.00	1.44	0.00
Al	3.36	2.86	0.79	1.16	3.20	2.60	6.00	2.60	3.05	0.51	7.75	0.49	2.80	0.05
C	7.37	1.54	4.44	1.18	4.25	2.80	2.00	5.00	3.20	1.44	-4.48	1.41	2.80	0.00

For binary systems, the 2NN MEAM potential parameters of samples are presented in Table 7.

Table 7. 2 NN MEAM parameters for binary systems

	Ti - Al	Ti - C
E _c	7.97	6.90
r _e	2.80	2.21
B	142	241
ρ_0^Y / ρ_0^X	1	6.00

To handle the Al-C system the Morse potential (Table 8) was used [46] [58]:

Table 8. Morse potential parameters for Al-C interactions

D ₀ (eV)	$\alpha(1/\text{Å})$	R _e (Å)
0.4691	1.738	2.246

3.2.2 Modeling Substrate Film Interface

Fundamentally, the model consists 34715 atoms of three different types (Al, Ti, C). At room temperature Ti64 consists of 2 phases: α -TiAl and β -TiV. In the current model we are dealing only with the alpha phase. According to the literature the adhesion between the alpha phase and the carbide surface is the weaker of the two interfaces. Therefore, we can get a conservative estimate of the strength of the interface with the present configuration.

The current configuration consists of TiC at the top (yellow and red) and α -TiAl at the bottom. The dimensions of the virtual sample are $47.13 \times 75.67 \times 158.32$ nm. The crystal structure for TiC is FCC-NaCl and the lattice constant is 0.4328nm. The α -TiAl phase has HCP structure with lattice constants $a= 0.291$ nm and $c=0.467$ nm represent the spacing between Ti64 atoms. [46] [58].

The simulation was run were conducted using LAMMPS open-source MD code.

LAMMPS is a classical molecular dynamics code with a focus on materials modeling.

It's an acronym for Large-scale Atomic/Molecular Massively Parallel Simulator.

LAMMPS runs on single processors or in parallel using message-passing techniques and a spatial-decomposition of the simulation domain. Many of its models have versions that provide accelerated performance on CPUs and GPUs. The code is designed to be easy to modify or extend with new functionality. LAMMPS is distributed as an open-source code under the terms of the GPLv2.

MD requires that the initial position of each atom to be defined. This was done using data from The Materials Project [47][59] and Vesta software [48]. Figure 48 shows the simulated composite before and after virtual simulation. The strain rate was set to be 10^9 s⁻¹ in mode I loading. The boundary conditions were periodic in the x and y direction and non-periodic in the z direction.

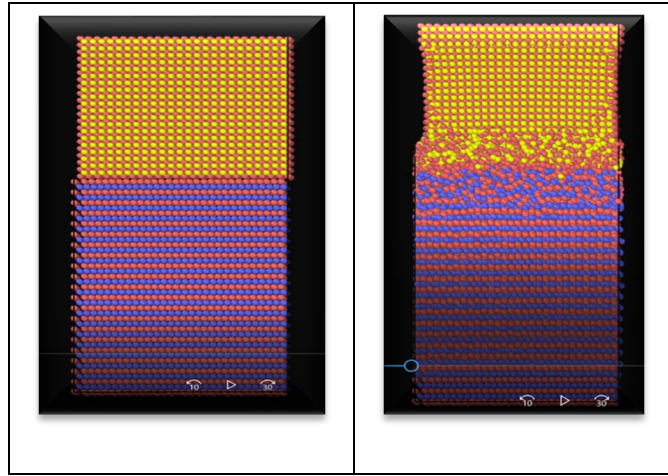


Figure 48. Simulation pre/post composite TiC – TiAl results.

Validation of the model and its potentials was done by comparing the ultimate stress of separation of the laminate model to the values reported in the literature.[46] [58] As can be seen from Figure 49, the mixed region sample has a significantly higher force of separation than the laminate model. Moreover, the separation happens all at once in the laminate model, representing immediate catastrophic failure. In the mixed region model failure more closely resembles the plasticity that we expected to see.

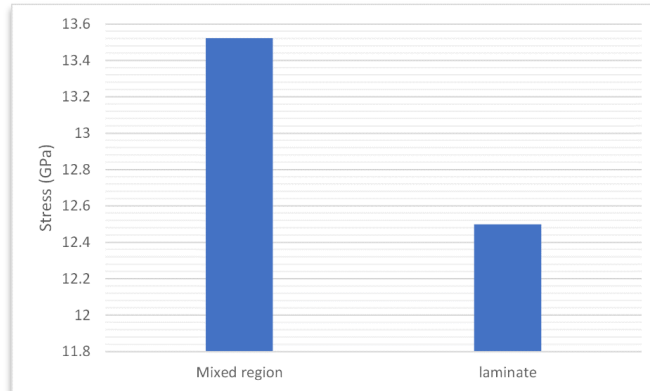


Figure 49. Stress fracture driven failure in composite materials

Application of Finite Element Method

After determining that the force of separation of the laminate model is significantly lower than the mixed region model, we sought to determine if a sample with the gradient profile determined in specific aim one would have greater fracture toughness than a homogeneous material. To do this we conduct a pull test using the finite element method (FEM). FEM is a method for deriving approximate solutions to complex mathematical problems. It is generally used when problems are too complex to be solved analytically and some degree of error is tolerable. There are two fundamental concepts associated with FEM. The first being partitioning bounded domains into a finite number of small, non-overlapping subdomains, or elements. Secondly, the boundary/initial value problems are formulated in a integral form so the contributions of each subdomain to the global integral sum to produce a complete integral characterizing the problem over the whole domain.

FEM Model Execution via Simulation

The simulation goal is goal to measure the stress intensity factor (SIF). Then we compare the stress intensity factor, K, for mode 1 crack propagation for the gradient sample and the homogeneous sample. The key idea being that the sample with the lower SIF is less likely to have crack propagation.

As detailed in Figure 50, the problem consists of a small patch of material in two dimensions. The crack is placed equidistant from the top and bottom at $h=15$. The width of the sample is 30 microns. And the length of the crack is 8.5 microns long. The carbide surface would be on top in this configuration. The Youngs modulus of the material is varied according to the polynomial defined in specific aim 1 using a **custom user subroutine**. All FEM calculations are completed in Abaqus.

Parameter	Dimensions (microns)
b	30
h	15
a	8.5

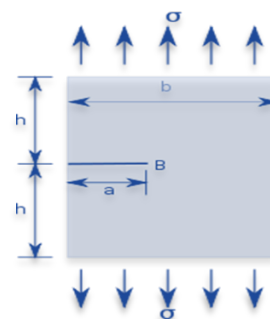


Figure 50. FEM crack Stress testing geometry.

Meshing

Meshing is a concept where many points are defined across the substrate geometry that allows software to identify clusters domains employed in the solution of equations. Figure 51 shows the substrate meshing scheme. The meshing intensifies as it approaches the crack tip depicted in Figure 50. The meshing is linear with quad elements in plain strain.

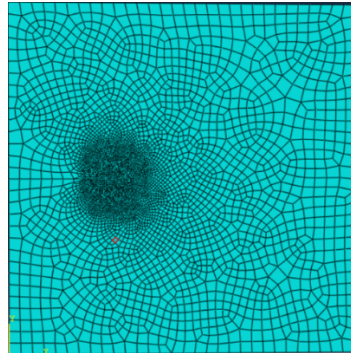


Figure 51. Material linear meshing scheme

Outcome

Figure 52 presents a visual representation of how the material properties vary with position or depth with the hardest material being on the top and the softer material being on the bottom.

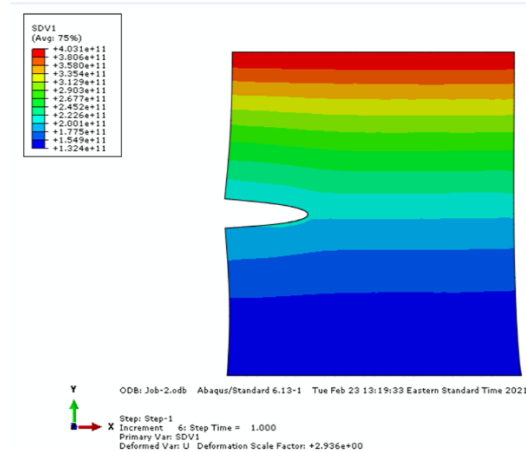


Figure 52. Stressed material properties variability as a function of depth

After applying a uniform stress to the top surface of the sample Figure 53 shows the non-uniform state of stress in the sample.

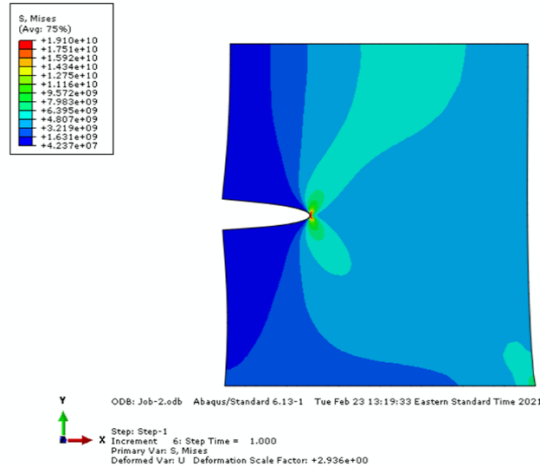


Figure 53. Non-uniform stressed profile of sample material

Figure 54 shows the modest improvement in the fracture toughness of the sample. The graded sample has a lower SIF than the uniform sample.

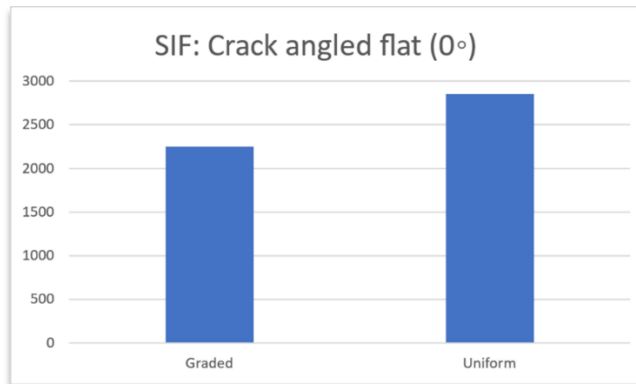


Figure 54. Sample fracture toughness

It is important to note that while performing MD simulations is relatively straightforward, using MD simulations to reach sound, high-impact conclusions remain decidedly nontrivial. Quality conclusion require: (1) an important question that can be addressed

by MD, (2) an appropriate simulation designed to answer relevant questions, (3) analyzing simulation runs for errors that might misinform the interpretation of results across runs, (4) comparison of simulation data to inform any subsequent experimentation.

Observation

Experiments can be designed to test specific fabrication scenarios. Thus, experiments and simulations can be used to broadly validate each other's results. Perhaps even more importantly, simulations can generate hypotheses that lead to new experimental work.

The careful application of MD simulations in concert with complementary experimental methods an area of great opportunity in material science. This opportunity will only grow as simulations become more tailorabile to material environment, faster, cheaper, and accurate. Effectively applying simulations to FGM material science requires careful thinking about both experimental and computational data available and thus will benefit from both broad expertise and interdisciplinary collaborations.

3.3 Characterization of Candidate Sample Design Parameters

Design of Experiment (DOE)

DOE is a powerful data collection and analysis tool allows the manipulation of multiple inputs to assess the fabrication of a composite run (i.e., experimental response/output). The strength of DOE is its ability to draw conclusions about the manner in which fabrication cycles are designed. This insight also allows the characterization of what the results of the run should look like. Thus, DOE can be used to address issues such as:

- The identification of those input factors not primary to the fabrication of the composite sample
- The identification of the primary input factors required to maximize control sample design properties
- The determination of the best setting for each of the primary control factor
- The stabilization of fabrication process variation to achieve a robust composite surface/interface profile.

DOE assumes that all inputs are independent of one another. The simultaneous manipulation of the design factors allows for evaluating important interactions that affect specimen fabrication that may not be immediately obvious. With DOE, any combinations of design factors (up to all combinations) can be examined.

The idea behind specific aim 3 is to explore the effect **that** relevant processing parameters play in the characteristics of the fabricated composite material. Two

properties of key interest are the depth, of the integration zone of the processed composite material. The integration zone being the affected subsurface region where properties gradually vary between those of the carbide film and the Ti64 substrate. Typically, an endeavor of this sort would take many experiments.

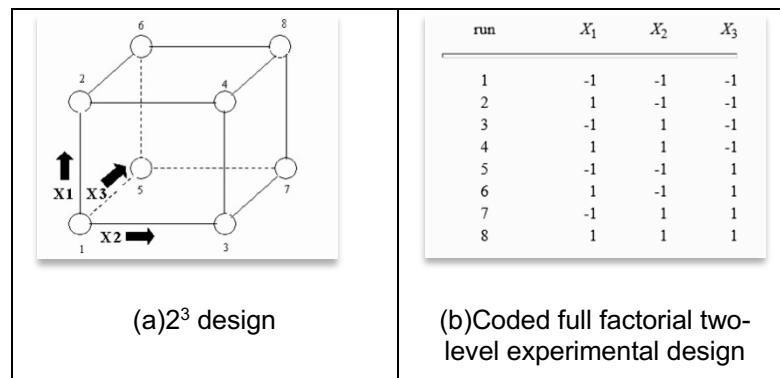
For the MD approach being used herein, an experiment consisting of 5 variables or “Factors” at 5 levels replicated 5 times would require 125 experiments. From experience, even a modest number of MD simulations running on a typical desktop computer can take many days to complete. The numbers quickly become untenable. For this reason, we use the concept of design of experiments (DOE) [Ref: Engineering Statistics Handbook] to improve the process experimental efficiency and cost.

DOE is a powerful data collection and analysis tool. It allows for multiple input factors (i.e., k) to be assessed to determine their effect on a desired experimental output (response). The simultaneous manipulation of factors allows for evaluating important interactions that may not be obvious. With DOE, all possible combinations (i.e., N^k , where N is the number of levels for each factor) can be examined or only a fraction (N^{-p}), where p indicated the fraction by which the possible number of experiments are down selected.

3.3.1 Design of Experiment Modeling

An important element of simulation design is the tailoring of the experimental plan to minimize extraneous runs. This screening is accomplished by limiting the simulation to only important factors that have a significant impact on the desired material properties. To design a simulation plan where there are k factors having only two possible values, there are as many as 2^k runs required (Figure 55). A 2^{k-p} design is a fractional factorial with even fewer runs than the full factorial design.

For instance, a $k=3$ -factor design would require 8 runs while a half fractional factorial design ($p=1$) would require only 4 runs. Levels are generally coded as high level (+/+1) or Low level (-/-1). So, if temperature is one of our factors, we would have a high (+) temperature and a low (-) temperature. The Figure 56a is a graphical representation of a two-level design with 3 factors (designated X_1 , X_2 , X_3)



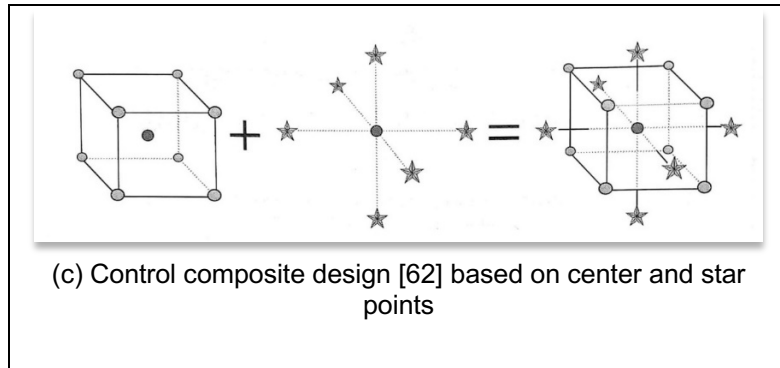


Figure 55. Graphical representation of a two-level design with 3 factors [49]

For such an experiment an ordinary linear regression model can be employed,

$$y = \beta_0 + \beta_1 x_1 + \beta_2 x_2 + \cdots + \beta_k x_k + \varepsilon \quad (46)$$

where y is the experimental outcome response of interest; β_0 is the intercept; β_i , β_{ij} and β_{ii} are coefficients of the linear effect, double interactions; x_i , x_j are the independent variables or factors and ε is error in y . The β s are related to main effects (and interactions in some cases). However, under many circumstances, Equation 45 may be too simple because it fails to allow for any curvature in the data surface. To detect curvature, center points may be added to the basic 2^k design of Figure 55a. Replication of center points (Figure 55c) can be used to estimate pure error.

If curvature is detected higher order terms are required. The generalized quadratic polynomial for describing the main and interaction effects for a $k=3$ process variables is:

$$\begin{aligned} y = & \beta_0 + \beta_1 x_1 + \beta_2 x_2 + \beta_3 \beta x_3 + \beta_4 x_1^2 + \beta_5 x_2^2 + \beta_6 x_3^2 \\ & + \beta_7 x_1 x_2 + \beta_8 x_2 x_3 + \beta_9 x_1 x_3 + \cdots \end{aligned} \quad (47)$$

The experiment is designed to allow the estimation of interaction and even quadratic effects (Figure 56), and therefore give an idea of the (local) shape of the response surface being investigated. For this reason, they are termed *response surface method (RSM) designs*. RSM designs RSM [49] [62] are used to:

- Find improved or optimal process settings
- Troubleshoot process problems and weak points
- Make a process more *robust* against external and non-controllable influences (i.e., CVD fabrication environment).

RSM methods can be used to fit the above polynomial. The data is then fit to a series of polynomial models using tools of regression. The resultant models are subjected to an analysis of variance to assess statistical significance and test for lack of fit.

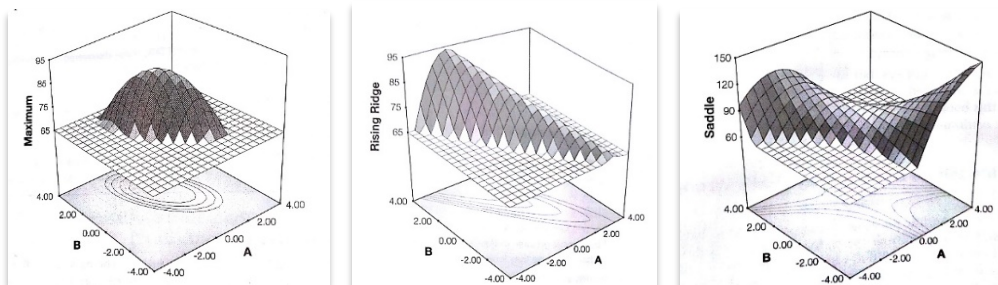


Figure 56. Common surfaces generated using RSM [63]

It is important that the selected model demonstrate a good fit. That is, the selected model predicts the best response. We need a numerical response to execute RSM.

A central composite design (CCD) is a subset of RSM that represent a 2^k full factorial construct to which a center and star points (α) are added.

The CCD is a **five-level** design with star points (Figure 55c) representing new extremes outside of the factorial points. The star points are, among other things, useful in estimating curvature. The precise value of $\alpha = [2^k]^{1/4}$ depends on certain properties desired for the design and the number of factors involved. The CCD always contains twice as many star points as there are factors.

3.3.2 Simulation of Material Dynamic Interaction

The carbon penetration experiment is based on the same physics as the pull off experiment of specific aim 2. This means that the atom types and interatomic potentials remain the same. The size of the simulation is much increased, However, specific aim 2 consisted of approximately 34,000 atoms while the current experiment consists of 8,000,000 atoms. The reason for the dramatic increase is we did not know how deep the carbon atoms would penetrate the substrate before beginning the experiment.

As seen in Figure 57, the basic model consists of a single carbon atom “fired” anywhere from 27 to 100 times at the substrate in an arbitrary direction determined by LAMMPS’ random number generator. The carbon atom begins centered three angstroms above the surface of the substrate. A two-dimensional representation of the 3D scheme can be seen in the figure below. The boundaries are periodic in the x and y directions and fixed in the z. The units scheme is set to ‘metal’. The 2NN MEAM potential is employed for interaction between Ti and Al and Ti and C. The Morse potential is used for interactions between Al and C. Time steps were adjusted based on the minimum needed to capture the motion at a given temperature. The NVE ensemble is used in this simulation, meaning that the number of particles, volume, and total energy for the system remain constant. The simulation is non-cumulative.

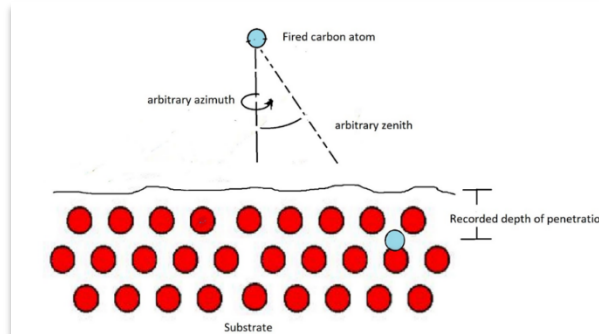


Figure 57. DOE model assuming a linear (max depth) and quadratic (average depth) response

Similar molecular dynamics studies have been conducted in the literature to track the amount of carbon and deuterium trapped in fusion relevant materials in Tokamak reactors.[50] [64] In these reactors energetic particles are produced and effect the

chamber walls in a number of ways that are reminiscent of the current experiment, these effects include but are not limited to sputtering, erosion, blistering , and finally deposition and retention.

Simulation Execution

For Specific Aim 3 we considered two responses for y: (1) average depth d_{avg} of carbon penetration, and (2) maximum depth d_{max} of carbon penetration.

Design Factor 1: Electron Temperature

Figure 58 gives a good overview of electron temperatures associated with different plasmas. [51] Based on Figure 58, the highest practical electron temperature is on the order of 10^3 . Because of this the high mark in our CCD was set to 1000eV. The low point was set to a reasonable 200eV. Of note these forces one of our star points into an unreasonable value of -72.72eV. This run is ignored for the purposes of evaluating this design. All runs are randomized.

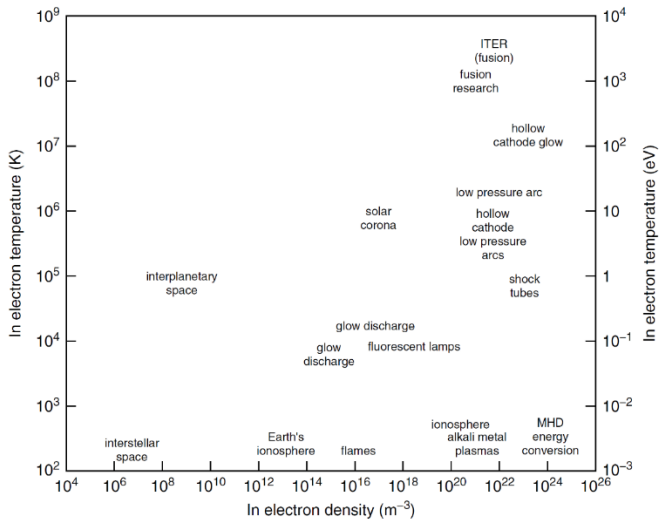


Figure 58. Common temperature range of natural and human elements

Design Factor 2: Substrate Temperature

The substrate temperatures are taken directly from the ranges achieved and measured in Specific Aim 1. Six hundred kelvin being the lowest temperature measured and 1300°K being a little higher than the highest temperature measured in the chamber. Of note is the fact that this temperature range forces one of our star points to be 1538.63°K, approaching the melting temperature of the substrate and higher than can safely be run in the quartz chamber.

Design Factor 3: Time

For time the limiting factor is the computational power available. The specifications of the system used are listed in Table 8. The smallest step size was 10^{-4} . With these

limitations the simulations lasted anywhere from 27 to 100 ps for the CCD with star points at 2 and 125 ps.

Table 9. Available DOE Computational Power provided by through Sabalcore Computing Inc.

CPU brand	CPU Model	Clock Speed	OS	Nodes used	Cores / Node	Total cores used	Ram/ Node	Ram/ Core	MPI Rate
Xeon	E5-2667v3	3.2 GHz	CentOS-7	4	16	64	256 GB	16 GB	100 Gb/s

Table 10. DOE simulation results.

Std	Run	Factor 1		Factor 2		Factor 3		Response	Response	Response
		A:Electron Temp eV	B:Substrate Temp K	C:Time Ps		Max depth A	Avg depth A	Thrap %		
12	1	600	1538.6274906776	63.5	29.63	24.19	100			
16	2	600	950	63.5	68.72	50.49	100			
2	3	1000	600	27	113.92	99.65	100			
9	4	-72.71713220	950	63.5						
5	5	200	600	100	103.16	91.02	100			
1	6	200	600	27	96.24	90.86	100			
6	7	1000	600	100	121.58	98.71	100			
10	8	1272.7171322	950	63.5	133.16	54.36	100			
13	9	600	950	2.1145616864789	55.33	52.06	100			
8	10	1000	1300	100	174.65	42.71	100			
4	11	1000	1300	27	174.65	42.62	100			
7	12	200	1300	100	62.1	30.63	100			
17	13	600	950	63.5	68.72	50.49	100			
11	14	600	361.3725093224	63.5	154.07	151.21	100			
18	15	600	950	63.5	68.72	50.49	100			
20	16	600	950	63.5	68.72	50.49	100			
15	17	600	950	63.5	68.72	50.49	100			
3	18	200	1300	27	32.7	30.17	100			
19	19	600	950	63.5	68.72	50.49	100			
14	20	600	950	124.8854383135	68.72	50.44	100			

Table 11. Response 1 (Max Depth) Fit Summary

Source	Sequential p-value	Lack of Fit p- value	Adjusted <i>R</i>²	Predicted <i>R</i>²	
<i>Linear</i>	0.0251		0.3440	0.0055	Suggested
<i>2FI</i>	0.1772		0.4477	-0.8781	
<i>Quadratic</i>	0.2031		0.5475	-1.2578	
<i>Cubic</i>			1.0000		Aliased

The **Model F-value** of 4.15 implies the model is significant. There is only a 2.51% chance that an F-value this large could occur due to noise.

P-values less than 0.0500 indicate **model terms are significant**. Thus, A (electron temperature) is a significant model term. Values greater than 0.1000 indicate the model terms are not significant.

Table 12. DOE Updated model: Response 1 (Max Depth) ANOVA Linear Model

Source	Sum of Squares	df	Mean Square	F- value	p-value
Model	15472.76	3	5157.59	4.15	0.0251*

					*Significant
<i>Factor 1:</i>					
<i>Electron</i>	12217.62	1	12217.62	9.82	0.0068
<i>Temp</i>					
<i>Factor 2:</i>					
<i>Substrate</i>	2931.34	1	2931.34	2.36	0.1456
<i>Temp</i>					
<i>Factor 3:Time</i>	323.80	1	323.80	0.2603	0.6173
Residual	18659.92	15	1243.99		
<i>Lack of Fit</i>	18659.92	10	1865.99		
<i>Pure Error</i>	0.0000	5	0.0000		
Cor Total	34132.69	18			

Table 13. Response 1 Max depth Updated Model

Linear	0.0251	0.3440	0.0055	Suggested
2FI	0.1772	0.4477	-0.8781	
Quadratic	0.2031	0.5475	-1.2578	
Cubic		1.0000		Aliased

Table 14. DOE Max Depth Updated model: Response for Factor 1

Model	12217.62	1	12217.62	9.48	0.0068	significant
Factor 1: Electron Temp	12217.62	1	12217.62	9.48	0.0068	
Residual	21915.07	17	1289.12			
Lack of Fit	21915.07	12	1826.26			
Pure Error	0.0000	5	0.0000			
Cor Total	34132.69	18				

From Table 14, the Model F-value of 9.48 implies the model is significant. There is only a 0.68% chance that an F-value this large could occur due to noise.

Removing the other two factors with less significance resulted in a significant increase in the overall significance of the model. The maximum depth of carbon penetration depends almost exclusively on the electron temperature.

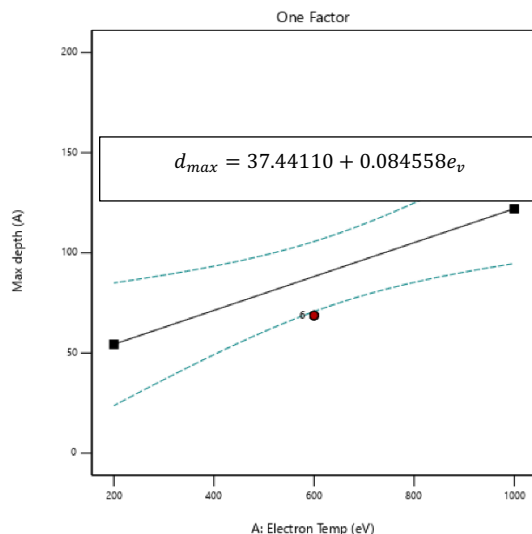


Figure 59. Confidence interval for estimated maximum depth of material penetration.

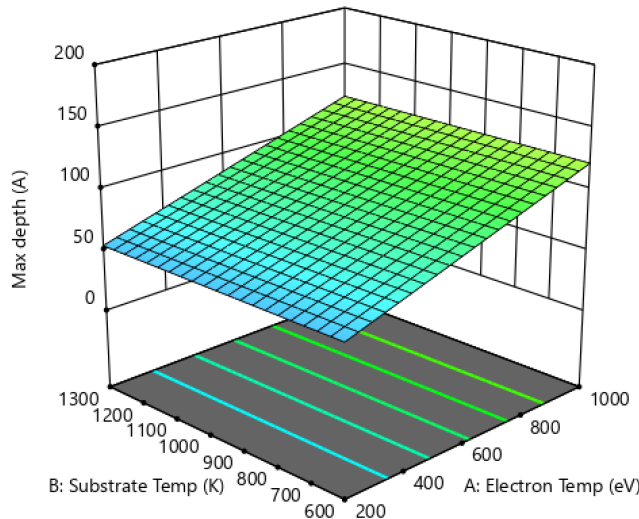


Figure 60. Maximum penetration depth as a function of Factor 1 and Factor 2.

Table 15. Response 2 (Average Depth) Fit Summary

Source	Sequential p-value	Lack of Fit p-value	Adjusted R ²	Predicted R ²	
Linear	< 0.0001		0.8039	0.7241	
2FI	0.9981		0.7556	0.5969	
Quadratic	< 0.0001		0.9694	0.8462	Suggested
Cubic			1.0000		Aliased

Table 16. Response 2 (Average Depth) ANOVA Quadratic Model

Source	Sum of Squares	df	Mean Square	F-value	p-value	
Model	17374.27	9	1930.47	64.27	< 0.0001	significant
A-Electron Temp	180.71	1	180.71	6.02	0.0366	
B-Substrate Temp	14678.59	1	14678.59	488.65	< 0.0001	
C-Time	0.6392	1	0.6392	0.0213	0.8872	
AB	8.10	1	8.10	0.2697	0.6161	
AC	0.2701	1	0.2701	0.0090	0.9265	
BC	0.2211	1	0.2211	0.0074	0.9335	
A ²	0.3853	1	0.3853	0.0128	0.9123	
B ²	2579.56	1	2579.56	85.87	< 0.0001	
C ²	9.43	1	9.43	0.3139	0.5890	
Residual	270.35	9	30.04			
Lack of Fit	270.35	4	67.59			
Pure Error	0.0000	5	0.0000			
Cor Total	17644.62	18				

The **Model F-value** of 64.27 implies the model is significant. There is only a 0.01% chance that an F-value this large could occur due to noise. From **Table 17**, a P-values less than 0.0500 indicate that the model terms are significant. In this case A, B, B² are significant model terms. Values greater than 0.1000 indicate the model terms are not significant.

Table 17. Updated Analysis of Variance (ANOVA)

Source	Sum of Squares	df	Mean Square	F-value	p-value	
Model	17355.44	3	5785.15	300.08	< 0.0001	significant
A-Electron Temp	196.61	1	196.61	10.20	0.0060	
B-Substrate Temp	14678.59	1	14678.59	761.39	< 0.0001	
B ²	2594.72	1	2594.72	134.59	< 0.0001	
Residual	289.18	15	19.28			
Lack of Fit	289.18	10	28.92			
Pure Error	0.0000	5	0.0000			
Cor Total	17644.62	18				

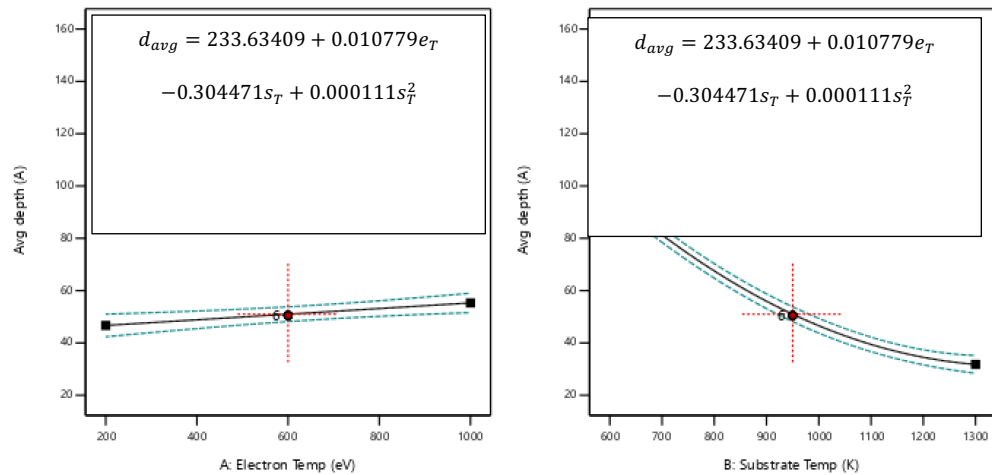


Figure 61. Estimated average penetration depth as a function of Factor 1 and Factor 2

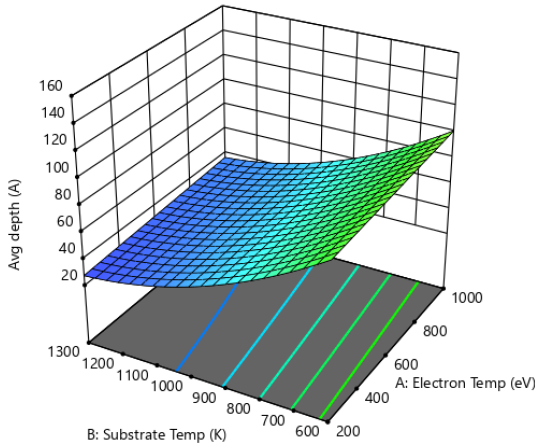


Figure 62. Visualization of average penetration depth

3.4 Observation

Because an electron temperature of -73 is not practical, run number 4 was excluded from this analysis. The first thing we notice about the results of this virtual experiment is that the carbon trap rate is 100 percent for all conditions explored. Based on the trajectory in Figure 62, if the substrate were sufficiently hot or the electron temperature were dropped, the trap rate may drop. But it's impossible to know for the data provided.

We found that the maximum depth of carbon penetration is dominated by the energy supplied to the plasma. However, the current model was time limited and therefore did not address the relatively slow process of diffusion. With sufficient computational power we may find that the complex interaction of substrate temperature pressure, velocity, and grain size and density play a significant role in the depth of carbon penetration. It

would be interesting to assess the impact of these factors independently and in combination.

The current experiment suggests that within the 100 or so picoseconds modelled, the substrate temperature exhibit a counterintuitive effect on carbon penetration. The model indicates that the higher the substrate temperature the lower the penetration depth, at least initially. This may be due to increased motion of surface atoms leading to deflection/ redirection of incident carbon atoms.

Chapter 4

4 Conclusions and Recommendations

The purpose of this research **has been** to explore the creation of a novel micro-textured surface, through plasma enhanced chemical vapor deposition on a Ti6Al4V metallic substrate and to understand the nature of the composite material interface. Specifically, we **wanted** to determine: (1) if a substrate film is being created and (2) what effect the processing parameters had on film growth and performance characteristics. As part of the assessment of the impact of processing parameters on the fabrication process, we **wanted** to know whether the substrate-film interface was functionally graded and its implication of what that means for film adhesion. To that end, our effort consisted of three investigative activities: (1) the characterization of the fabricated surface using techniques such as microscopy, indentation, and statistical methods to determine the deposited film's composition and properties; (2) assessment of the fabricated specimen's computational adhesion using FEM and MD to determine if the fabricated composite specimen has a greater theoretical adhesion than a laminate or homogeneous specimen; and (3) employment of the DOE method to assess the depth of penetration profile of carbon, and by extension the depth of the fabricated specimen's integration zone, as a function of the processing parameters.

This study effort confirmed that the issues encountered in compositional grading are truly alloy-specific. While the titanium-carbide gradient was impeded by a set of more subtle metallurgical concerns. The modeling and experimental efforts demonstrated that the concept is promising. More specifically, the gradients produced using TiC -TiAl may be suitable for biomechanical service with additional refinement.

The efforts undertaken proved to be instrumental in identifying a number of important details of additive compositional grading that would otherwise have gone unacknowledged. A summary of the major observations and lessons learned are provided for each thesis objective.

4.1 Physical Fabrication Experimental Outcomes (Objective 1)

Experimentation was fundamentally focused at gaining a depth of insight about the properties of a novel composite specimen. To achieve the desired understanding, the growth of the composite material's properties requires a careful fabrication of the target material. The LIMB system was instrumental in the fabrication of sample specimens. Once the system was calibrated, each specimen was fabricated using a set of specific design parameters that required approximately four hours to complete the end-to-end process.

Characterization of the specimen's surface using light microscopy revealed that it had a grain like growth structure. We believe this to be epitaxial carbide growth where the thin

film's growth is aligned with the underlying crystal orientation. A more detailed examination using SEM revealed that small crystalline clusters of unknown composition was also present. Using automatic image thresholding we found that these features covered 8.2 % of the surface and that 0.36% of the surface were pores. The remaining 91.44% represented carbide coverage. It was also determined that the carbide region of the cross section was approximately 30 to 50 microns thick.

Microhardness testing of the specimen indicated that the film was at least 22 percent harder than the underlying substrate. But due to the relative size of the indenter, it was not possible to gain the precision required to make a definitive determination. However, nanohardness testing, with its ability to isolate the film from the substrate, indicated that the film was at least twice as hard as the unprocessed substrate.

The heterogeneous nature of the subsurface gradient precluded using a strict linear probe. Instead, a grid-based indentation was used along with statistical deconvolution to extract the mechanical properties of differential phases within the specimen's subsurface region. Atomic force microscopy proved useful in mapping the nanomechanical data. Custom computer code was developed and applied to process the specimen's block pixelated surface image (to differentiate hard carbide material from the softer substrate material). The analysis indicated that a material gradient spanned approximately 30 microns beyond the visible region.

4.1.1 General Observations

- Although plasma is a useful technique for the development of additive gradients, it is apparent that much of the success comes from a dedication to ensuring the plasma intermixing at temperature is compatible with the infrastructure being used. While this is a reasonable approach for some joining processes, its viability needs to be proven for full additive manufacturing due to the potential for melting. Also, the risk of cracking is a real risk.
- Fabrication-dependent adjustment of process parameters is only so effective in accommodating large property differences between materials. Simultaneous deposition of material with large differences in density and melting temperature is particularly difficult to manage with a single set of process parameters, and is likely to result in striation of material within the thermal plasma and nonuniform distributions of alloying elements in the resultant specimen.
- Refinement of the plasma dynamic process is a critical activity for the development of graded specimens. The fabrication of specimens must be found for composite material gradients that does not promote deleterious effects at the microstructural level. However, for gradients between alloys with

large property differences, this may not always be possible. As a result, the specimen will not exhibit optimum fitness characteristics,

- Characteristics microstructure, mechanical properties, and thermal properties do not vary smoothly within fabricated specimen, but can display threshold behavior. If sharp and shallow interfaces are to be avoided, these thresholds must be identified such that the gradient can be extended to an appropriate performance range.
- The concentrations of impurities along a gradient can affect the specimen's microstructure by the formation of deleterious phases (e.g., nonuniform), and defect concentration (e.g., pores). Thus, it is important to use materials with good purity to minimize the possibility of these undesired effects.

Beyond research, the typical candidate specimen testing other factors to consider include cost, durability, maintenance, weight, strength to weight ratio stiffness, thermal conductivity, and expansion coefficient. The research objectives of this thesis did not consider all these factors. As stated, the focus has been limited to testing related to wear, adhesion, etc. For the novel material being studied, these are factors are considered most likely to cause degrade a specimen's structural and biomechanical performance; whereas issues such as fabrication temperature was identified as having an effect on the sample matrix.

4.2 Virtual Fabrication Modeling and Simulation Outcomes

4.2.1 Virtual Fabrication Experimental Outcomes (Objective 2)

For specific aim 2 we are trying to determine if a sample with a mixed interface would have better adhesion than a laminate (flat layered sample). We, first, used MD and the open-source programming language LAMMPS to create a virtual sample consisting of 34,000 atoms. The carbide region was then virtually pulled from the substrate and the maximum stress recorded. This was done for a sample with a mixed interface and a sample with a laminate interface. The model included periodic boundary conditions and the 2NN MEAM interatomic potential. The results indicated that the stress of separation was significantly higher for the mixed sample.

Second, a finite element approach was used to determine if a sample with the gradient profile measured in specific aim 1 is tougher than a homogenous sample with the material properties of the substrate. Commercially available software Abaqus was used with a custom user subroutine to vary material properties according to the results of specific aim 1.

The general idea is to conduct a pull off test using the FEM then measure the SIF. The sample with the lower SIF is less likely to have crack propagation (i.e., is tougher). The model consisted of a two-dimensional square specimen with a crack. Results indicate that the mesh density increased near the crack tip and its type was linear with quad

elements in plane strain. The stress intensity at the crack tip was significantly higher for the uniform sample indicating that a crack is less likely to propagate in our graded sample.

4.2.1.1 General Observations

- The use of MD and FE computational models to gain insight into the material properties of composite specimens has proved to be very insightful;
- One of the challenges in conducting virtual modeling and simulation of composite material may be the need to customize existing software.
- The computational intensity required to conduct virtual experimentation can become resource prohibitive;
- The use of virtual modeling and simulation tied to the LIMB capability has great potential to expand the scope of question that can be pursued.

4.2.2 Virtual Fabrication Experimental Outcomes (Objective 3)

The idea behind specific aim 3 is to use MD to explore the effect key processing parameters have on the growth properties of the integration zone (i.e., depth).

The DOE model was central to the success in meting the goal of this objective. The basic model consists of a single carbon atom “fired” anywhere from 27 to 100 times at the substrate in an arbitrary direction determined by LAMMPS’ random number generator. The process begins with the carbon atom centered three angstroms above the surface of the substrate. The process ends with the recording of the atom’s final penetration depth.

Manipulating the electron and substrate temperature independently, it was found that the substrate temperature had the greatest effect on penetration depth. However, the effect was counterintuitive. That is, the hotter the substrate, the lower the penetration depth. We reason that this is because of the increased surface motion of substrate atoms essentially obscuring the projectiles path.

4.2.2.1 General Observations

The outcome of this study has been the establishment of an interim approach for developing and analyzing gradients based on iterative modeling and experimental efforts. The tenets of that approach spanned a literature review, physical gradient fabrication, microstructural characterization, and thermodynamic modeling. Iterating on these efforts would allow the design of the gradient to be characterized based on a set of optimized fabrication parameters. While a more comprehensive modeling approach

may have been ideal, it was found that the experimental efforts were adequate for focusing the development and assessment of gradient material. Without the fabrication and analysis of prototypes, there were simply too many degrees of freedom to predetermine the critical phenomena that must be addressed with modeling. The modeling, in turn, provide for dynamic approaches than are possible through physical with experiment alone. Combining physical and virtual experimentation has proved to be an effective means of reducing the time required to characterize a successful gradient design.

- Modeling is particularly useful for predicting the occurrence of fast-forming equilibrium phases, as well as nonequilibrium solidification behavior. The predictions generally agree with observations (when all factors are taken into consideration, e.g., diffusion) in plasma deposited gradients. However, this negative is limited when considering laminated (i.e., diffusionless) composites.

4.3 Recommendations for Future Work

Overall, it is recommended that continued experimentation with compositionally graded metals be carried out in tandem with the application of improved open-source modeling tools. Of particular interest for immediate applications are gradients of titanium composite materials. Increasing the scope and number of experimental case studies will facilitate the ability of modeling efforts to guide and predict the performance and

behavior of fabricated specimens. Also, modeling and simulation can reduce the timeline from prototype to final gradient.

The most critical aspect of virtual experimentation is:

- Development of a more rigorous method for fabrication parameter optimization. Of course, in the longer term, advances also remain to be made in the fabrication process itself to expand beyond one-dimensional gradients. Only then can true three-dimensional tailoring of composition be realized;
- The creation, use, and refinement of visualization tools for intuitive exploration of higher order more complex material matrices;
- Enhanced ability to predict phase composition of new alloys;
- Better control of feedstock powder quality and defect concentration in gradient parts;
- Expanded availability and use of diagnostic tools and techniques.

4.4 Final Remarks

Many questions remain whether research and experimentation fabrication can produce materials that don't suffer the degrading effects of erosion caused by wear related abrasive forces. Given the pace of technology advances, there is no doubt that there will be improvements in material sciences processes that will have a demonstrative impact on the construction and performance characteristics of biomechanical systems. While this thesis has considered an aspect of the technology, the complexity of other materials and fabrication processes must be added to the mix. At that point, the question becomes: How far are we away from being able to realize this goal 'scapability, and what will it take to get there? If the results of this thesis are any indication, the answer varies. For evolving technologies such as 3D printing, simple interfaces between composite alloys, such as titanium and aluminum, may benefit from an iterative series of physical and virtual modeling experimentation. Through effective research, the rapid development and qualification of differential alloys need not go through the exhaustive and time-consuming empirical testing required currently. Fortunately, such approaches are gaining momentum.

5 References

- [1] S. Shrestha, A. J. Dave, E. Losina, and J. N. Katz, "Diagnostic accuracy of administrative data algorithms in the diagnosis of osteoarthritis: A systematic review," *BMC Medical Informatics and Decision Making*, vol. 16, no. 1. BioMed Central Ltd., 07-Jul-2016.
- [2] D. Chen *et al.*, "Osteoarthritis: Toward a comprehensive understanding of pathological mechanism," *Bone Research*, vol. 5. Sichuan University, 17-Jan-2017.
- [3] A. Manoharan, X. Xie, O. Gajic-Veljanoski, D. Wells, and C. Holubowich, "Structured education and neuromuscular exercise program for hip and/or knee osteoarthritis: A health technology assessment," *Ont. Health Technol. Assess. Ser.*, vol. 18, no. 8, pp. 1–110, Nov. 2018.
- [4] M. H. Atkinson, "Osteoarthrosis.," *Can. Fam. Physician*, vol. 30, pp. 1503–7, Jul. 1984.
- [5] D. T. Felson, J. J. Anderson, A. Naimark, A. M. Walker, and R. F. Meenan, "Obesity and knee osteoarthritis. The Framingham Study," *Ann. Intern. Med.*, vol. 109, no. 1, pp. 18–24, 1988.
- [6] J. Conde, M. Scotce, R. Gómez, V. Lopez, J. J. Gómez-Reino, and O. Gualillo, "Adipokines and Osteoarthritis: Novel Molecules Involved in the Pathogenesis and Progression of Disease," *Arthritis*, vol. 2011, pp. 1–8, Aug. 2011.
- [7] "Hip replacement." [Online]. Available: <https://www.mayoclinic.org/tests>

procedures/hip-replacement/about/pac-20385042.

- [*] G.S. Nayak, et al, "Trends in Metal-Based Composite Biomaterials for Hard Tissue Applications," *JOM* vol 74, No 1, 2022.
- [8] "Hip Joint." [Online]. Available: https://www.hss.edu/condition-list_hip-replacement.asp.
- [9] C. Y. Hu and T.-R. Yoon, "Recent updates for biomaterials used in total hip arthroplasty," *Biomater. Res.*, vol. 22, p. 33, Dec. 2018.
- [10] J. Migaud, H., Putman, S., Krantz, N., Vasseur, L., & Girard, "Cementless metal-on-metal versus ceramic-on-polyethylene hip arthroplasty in patients less than fifty years of age: a comparative study with twelve to fourteen-year follow-up," *J. bone Jt. Surg.*, vol. American v, pp. 137–142, 2011.
- [11] D. Bitar and J. Parvizi, "Biological response to prosthetic debris," *World J. Orthop.*, vol. 6, no. 2, pp. 172–189, Mar. 2015.
- [12] P. F. Gomez and J. A. Morcuende, "A historical and economic perspective on Sir John Charnley, Chas F. Thackray Limited, and the early arthroplasty industry," *Iowa Orthop. J.*, vol. 25, pp. 30–37, 2005.
- [13] P. Bracco, A. Bellare, A. Bistolfi, and S. Affatato, "Ultra-High Molecular Weight Polyethylene: Influence of the Chemical, Physical and Mechanical Properties on the Wear Behavior. A Review," *Mater. (Basel, Switzerland)*, vol. 10, no. 7, p. 791, Jul. 2017.
- [14] M. C. Sobieraj and C. M. Rimnac, "Ultra high molecular weight polyethylene: Mechanics, morphology, and clinical behavior," *J. Mech. Behav. Biomed. Mater.*, vol. 2, no. 5, pp. 433–443, 2009.

- [15] L. McKeen, *The Effect of Sterilization on Plastics and Elastomers*, 3rd ed. Elsevier Inc, 2012.
- [**] A.J., Sturgeon, Mater. World 1, 1 (1993).
- [16] K. M. M. Matyjaszewski, Ed., *Polymer Science: A Comprehensive Reference*. Elsevier Science, 2012.
- [17] M. D. Ries and L. Pruitt, "Effect of Cross-linking on the Microstructure and Mechanical Properties of Ultra-High Molecular Weight Polyethylene," *Clin. Orthop. Relat. Res.*, vol. 440, 2005.
- [18] N. A. Beckmann *et al.*, "Long-term durability of alumina ceramic heads in THA," *BMC Musculoskelet. Disord.*, vol. 16, no. 1, p. 249, 2015.
- [19] Y.-K. Lee, Y.-C. Ha, J. J. Yoo, K.-H. Koo, K. S. Yoon, and H. J. Kim, "Alumina-on-Alumina Total Hip Arthroplasty: A Concise Follow-up, at a Minimum of Ten Years, of a Previous Report: *," *JBJS*, vol. 92, no. 8, 2010.
- [20] I.-Y. Choi, Y.-S. Kim, K.-T. Hwang, and Y.-H. Kim, "Incidence and factors associated with squeaking in alumina-on-alumina THA," *Clin. Orthop. Relat. Res.*, vol. 468, no. 12, pp. 3234–3239, Dec. 2010.
- [21] A. Salehi and G. Hunter, "Laboratory and Clinical Performance of Oxidized Zirconium Alloy," *Clin. Cases Miner. Bone Metab.*, vol. 7, no. 3, p. 169, 2010.
- [22] J. Drummond, P. Tran, and C. Fary, "Metal-on-Metal Hip Arthroplasty: A Review of Adverse Reactions and Patient Management," *J. Funct. Biomater.*, vol. 6, no. 3, pp. 486–499, Jun. 2015.
- [23] S. Agarwala, G. Mohrir, and P. Moonot, "Functional outcome following a large head total hip arthroplasty: A retrospective analysis of mid term results," *Indian J.*

- Orthop.*, vol. 48, no. 4, pp. 410–414, Jul. 2014.
- [24] J. M. Cuckler, “The Rationale for Metal-on-Metal Total Hip Arthroplasty,” *Clin. Orthop. Relat. Res.*, vol. 441, 2005.
- [25] F. Staff, “Concerns about Metal-on-Metal Hip Implants,” 2021. .
- [26] R. J. Underwood, A. Zografos, R. S. Sayles, A. Hart, and P. Cann, “Edge loading in metal-on-metal hips: low clearance is a new risk factor,” *Proc. Inst. Mech. Eng. H.*, vol. 226, no. 3, pp. 217–226, Mar. 2012.
- [27] J. B. Mistry *et al.*, “Trunnionosis in total hip arthroplasty: a review,” *J. Orthop. Traumatol.*, vol. 17, no. 1, pp. 1–6, 2016.
- [28] S. Ghosh and S. Abanteriba, “Status of surface modification techniques for artificial hip implants,” *Sci. Technol. Adv. Mater.*, vol. 17, no. 1, pp. 715–735, Nov. 2016.
- [29] I. Gómez *et al.*, “Improved Adhesion of the DLC Coating Using HiPIMS with Positive Pulses and Plasma Immersion Pretreatment,” *Coatings*, vol. 11, no. 9, 2021.
- [30] R. Morent and N. De Geyter, “1 - Improved textile functionality through surface modifications,” in *Functional Textiles for Improved Performance, Protection and Health*, N. Pan and G. Sun, Eds. Woodhead Publishing, 2011, pp. 3–26.
- [31] IHI Group, “PVD.” [Online]. Available: <https://www.ionbond.com/technology/pvd/>.
- [32] TWI, “What is Chemical Vapour Deposition (CVD)?” [Online]. Available: <https://www.twi-global.com/technical-knowledge/faqs/faq-what-is-chemical-vapour-deposition-cvd>.
- [33] K. Mallika and R. Komanduri, “Low pressure microwave plasma assisted chemical

vapor deposition (MPCVD) of diamond coatings on silicon nitride cutting tools," vol. 396, pp. 145–165, 2001.

[!!@] Y.L.Chung and S.H. Chi, "The residual stress of functionally graded materials," Journal of the Chinese Institute of Civil and Hydraulic Engineering, vol 13, pp 1-9, 2001.

[!!@@] S.H. Chi, and Y.L.Chung, "Cracking in sigmoid functionally graded coating," Journal of Mechan1qcs, vol 18, pp 41-53, 2002.

[34] J. E. Butler, Y. A. Mankelevich, A. Cheesman, and J. Ma, "Understanding the chemical vapor deposition of diamond : recent progress," vol. 364201, 2009.

[35] T. L. VanDamme NS, Que L, "Carbide surface coating of Co-Cr-Mo implant alloys by a microwave plasma-assisted reaction," *J Mater Sci.*, vol. 34, 1999.

[36] S. Sullivan, "An investigation of the growth and characteristics of a micro- textured titanium alloy surface and the biocompatibility of a micro-textured cobalt-chromium-molybdenum alloy surface Name," University of Maryland Baltimore County, 2012.

[37] T. L. VanDamme NS, Wayman BH, "Wear behavior of carbide coated Co-Cr-Mo implant alloy," *J. Mater. Sci.*, vol. 14, 2003.

[!] M.S. Daw, et al, "The embedded-atom method: a review of theory and application," Materials Science Reports 9, North-Holland, 1993, p251-310.

[*.] Plimpton J., "Fast Parallel Algorithms for Short-Range Molecular Dynamics," *J Comput. Physics*. 1995.

[38] S. P. B. K.R. Kambale, Akash Mahajon, "Effect of grain size on the properties of cermics," *Met. Powder Rep.*, 2019.

[39] S. N. Naik and S. M. Walley, "The Hall–Petch and inverse Hall–Petch relations

- and the hardness of nanocrystalline metals," *Journal of Materials Science*, vol. 55, no. 7. pp. 2661–2681, 2020.
- [40] G. D. Junbo Hou, Zaoli Zhang, Wolfgang Preis, Werner Sitte, "Electrical properties and structure of grain boundaries in n-conducting BaTiO₃ ceramics," *J. Eur. Ceram. Soc.*, 2011.
- [41] Y. C. Z. He, J. Ma, R. Zhang, ".," *Mater. Sci. Forum*, pp. 483–486, 2003.
- [42] S. S. Zumdahl, "titanium carbide," *britannica*. 2022.
- [43] G. Sastre, "Chapter 2 - Molecular Dynamics of Hydrocarbons in Zeolites: Historical Perspective and Current Developments**Dedicated to the memory of Prof. Jule A. Rabo, a pioneer in zeolite science.," in *Modelling and Simulation in the Science of Micro- and Meso-Porous Materials*, C. R. A. Catlow, V. Van Speybroeck, and R. A. van Santen, Eds. Elsevier, 2018, pp. 27–62.
- [44] B.-J. Lee, M. I. Baskes, H. Kim, and Y. Koo Cho, "Second nearest-neighbor modified embedded atom method potentials for bcc transition metals," *Phys. Rev. B*, vol. 64, no. 18, p. 184102, Oct. 2001.
- [45] J. H. Rose, J. R. Smith, F. Guinea, and J. Ferrante, "Universal features of the equation of state of metals," *Phys. Rev. B*, vol. 29, no. 6, pp. 2963–2969, Mar. 1984.
- [46] Y. C. S. Mohamed G. Elkhateeb, "Molecular dynamics-based cohesive zone representation of Ti6Al4V/TiC composite interface," *Mater. Des.*, vol. 155, pp. 161–169, 2018.
- [47] A. Jain *et al.*, "The Materials Project: A materials genome approach to accelerating materials innovation," *APL Mater.*, vol. 1, no. 1, p. 11002, 2013.

- [48] K. MOMMA, “VESTA.” 2022.
- [49] M. J. Anderson, *RSM Simplified*. New York, NY: Productivity Press, 2005.
- [50] X. Yang, “Atomistic Simulation of Plasma Interaction with Plasma Facing Components in Fusion Reactors,” Purdue University, 2013.
- [51] H. John, *Introduction to Plasma Technology: Science, Engineering and Applications*. Wiley-VCH, 2010.

6 APPENDIX A: MPACVD Standard Operating Procedures

The procedures outlined ion this appendix are designed to support the fabrication of composite specimens using the LIMB system. The table below provides an overview of the operational timescale required of each procedure.

CAUTION:

- The chamber should **always** be kept under a vacuum, even when not running experiments, to ensure optimal system performance.
- All valves must be closed at the beginning and end of each experiment.
- Only the flow controller power supply/readout units are on – all other power is off at the beginning and end of each experiment.

Step	Order of Operation	Procedure No.	Est. Time Required	Monitoring Requirements
1	System On	I	5 min	Full attention
2	Insert/Remove Substrate Material	II	15 - 30 min	Full attention
Possible break time: If not shutting down the system prior to conducting the leak test, goto #6				
3	Create a Vacuum (for shut down)	III	15 min	System must be under vacuum at all time: pull vac for 10 minutes, minimum

4	System Shut Down	VIII	5min	Full attention
5	System On	I	5 min	Full attention
6	Create a Vacuum (for deposit)	III	1 hr 5 min	No monitoring required during 1 hr vacuum pull.
7	Vacuum Leak Test	IV	1 hr 15 min	No monitoring required during 1 hr wait period
Possible break time: If not shutting down the system prior to conducting the deposit, goto #10				
8	System Shut Down	VIII	5min	Full attention
9	System On	I	5min	Full attention
10	Starting the H ₂ Flow	V	20 min	Full attention
11	Microwave Generation & Methane	VI	2 hrs 45 min to 6 hrs 45 min	Full attention
12	CVD Stop process	VII	2 hrs 25 min	No monitoring required during 2 hr + specimen cool
Possible break time: If not shutting down the system while the specimen cools, goto #15				
NOTE: If inserting a new substrate specimen while retrieving a completed deposit, goto # 2				
13	System Shut Down	VIII	5min	Full attention (no monitoring during 2 hr cool)
14	System On	I	5min	Full attention

15	Insert/Remove Substrate Material	II	15 - 30 min	Full attention
16	Create a Vacuum (for shut down)	III	15 min	System must be under vacuum at all time: pull vac for 10 minutes, minimum
17	System Shut Down	VIII	5 min	Full attention

Procedure I: System On

Overview:

The chamber is currently under a vacuum and all valves are closed. During this step, the Exhaust Valve Controller (EVC), EVC Cooling Fan, Baratron Pressure Gauge, and Vacuum Pump are turned on to ready the system for either a CVD on a substrate or for performing only the vacuum test.

Turn on the exhaust valve controller (EVC). Pull the lever out and flip it up into the “ON” position.

Turn on the Baratron Pressure Gauge controller. Pull the lever out and flip it up into the “ON” position. The digital read out will turn on.

Turn on the cooling fan located behind the EVC and Baratron Pressure Gauge and check that it is aimed to cool them.

- 1 Plug in the thermocouple vacuum gauge (note hydrogen, H₂ exception below) located on the top position of the power strip on the left end of the CVD.
 - a. EXCEPTION: the thermocouple should always be unplugged when using hydrogen, H₂

NOTE: thermocouple vacuum gauge does not have an on/off switch. When it is plugged in, it is turned on, when it is unplugged, it is off.

Plug in the vacuum pump. NOTE: the vacuum pump does not have an on/off switch. When it is plugged in, it is turned on, when it is unplugged, it is off.

End of this procedure.

Procedure II: Insert/Remove Substrate Material

Overview:

The chamber is currently under a vacuum and all valves are closed. During this step, the chamber is filled with Argon gas to bring the chamber to (approximately) ambient pressure. The chamber is opened, the substrate inserted/removed and the chamber is sealed again.

- 2 Open the Argon gas cylinder
 - a. Open the valve to the Argon cylinder
 - b. Open the regulator valve to the Argon gas cylinder
 - a Note: the regulator should be set to 18 to 20 psi
- 3 Open the Gas Flow Controller Panel
 - a. Fully open the Argon, Ar, flow valves (2 valves, 1 before and 1 after the flow controller) on the Gas Flow Controller Panel
 - b. Open the Pre-Reactor Valve on the Gas Flow Controller Panel
- 4 Start the flow of Argon
 - a. Turn on the Argon Flow Controller Readout by switching the right lever up into the "ON" position. (Note: this is a 3-position switch; up = "ON", middle = "OFF" and down = "EXT")
 - b. Start the flow by switching the left lever up into the "FLOW" position. (Note: this is a 3-position switch; up = "FLOW", middle = (no label) and down = "REMOTE")
- 5 Record the start time of Argon gas flow
 - a. Allow the Argon gas to flow until the pressure reaches ~740.
 - b. Note: The dial is used to regulate the flow. The calculated setting for the dial is 556 (5 in the window, 56 on the dial ring).
- 6 Stop the flow of Argon when the chamber reaches the ambient pressure (~740 Torr with the present Baratron Pressure Gauge controller).
 - a. Stop the flow by switching the left lever from the "FLOW" position to the middle position (not down).
 - b. Turn off the Argon Flow Controller Readout by switching the right lever from the "ON" position to the middle, "OFF" position.
 - c. Note: It is best not to create a pressure in excess of 740 Torr. A pressure greater than ambient may force gas into areas, requiring longer vacuum times to extract it.
- 7 Record the time at which the Argon gas flow was stopped
- 8 Note the pressure: 740 ± 10 Torr (mmHg) is acceptable
 - a. If the chamber pressure of 740 ± 10 Torr (mmHg) is acceptable, continue to step "8. Close the gas controller panel"

- b. If a chamber pressure exceeding 750 Torr is created, evacuate the chamber
- Close the two Argon flow valves on the Gas Flow Controller Panel
 - Complete "Procedure III: Create a Vacuum"
 - When the chamber has reached it's minimum value on the Baratron Pressure Gauge
 - Close the throttling valve on the Exhaust Valve Controller (EVC)
 - Flip the switch down to the "CLOSED" position.
 - Rotate the knob counter-clockwise into the "CLOSED" position.
 - Close main valve on the vacuum pump
 - Return to Step "2. Open the Gas Flow Controller Panel", and continue the procedure from there.
- 9 Close the Gas Flow Controller Panel
- Close the 2 Argon flow valves on the Gas Flow Controller Panel
 - Close the Pre-Reactor valve on the Gas Flow Controller Panel
- 10 Close the Argon gas cylinder
- Close the regulator valve to the Argon gas cylinder
 - Close the valve on the Argon cylinder
- 11 Check that the vice clamp is available and ready to hold the substrate mount feed-through
- 12 Be sure the substrate specimen/container and tweezers are ready and accessible prior to accessing the chamber substrate mount.
- 13 Place a clean piece of paper below the opening to the chamber.
- 14 Any person handling the equipment or substrate specimen must thoroughly wash and dry their hands.
- 15 Open the chamber
- Loosen the wing nut without unclamping the seal for the substrate mount feed-through
 - Hold the knob in one hand (white mark on knob is facing forward) and release the clamp with your other hand.
 - Place the clamp on the clean piece of paper below.
-
- 16 Remove the substrate mount
- Holding the knob in one hand, use the other hand to steady the quartz rod and slowly & cautiously remove the substrate mount through the feed-through opening in the chamber.
 - Be careful not to touch the area near the vacuum seal – it will have vacuum grease on it.
 - Note: the quartz rod is not attached to the metal knob base and can be easily lifted out of the base. Be cautious while handling these so that they do not detach.
- 17 Secure the substrate mount on the vice
- Place the substrate mount in the vice such that the black knob is below the vice and the vacuum seal flange is above it.
 - Align the rod of the substrate mount w/ the v-notch in the vice
 - Close the vice so that it is fitted without using much force
- 18 Using the tweezers, place (or remove) the specimen in the tantalum basket
- 19 Carefully reinsert and clamp the substrate mount. Note: maintain alignment or the substrate mount will catch along the sides of the chamber while feeding it though.
- The white mark on the knob should face out
 - Re-assemble the clamp. The wing nut is to be finger tight.

Note: The **tatalum** basket in the chamber holds a .75" diameter specimen, typically 7mm thick.

The system is on (See Procedure I: System On)

Procedure III: Create a Vacuum

Overview:

With the exception of the insertion or removal of a specimen, the system should be kept under vacuum at all times. When the system is shut down, all valves are closed to maintain the vacuum. While pulling a vacuum, the Pre-Reactor valve is opened to allow any gases in the line to be pulled.

The system is on (see Procedure I: System On)

- 1 Open the Pre-Reactor valve on the Gas Controller Panel
- 2 Completely open the main valve on the vacuum pump
- 3 Open the throttling valve on the Exhaust Valve Controller (EVC)
 - a. The knob is in the “CLOSED” position, rotate it one position clockwise, to align with the line just above the closed position. This is manual mode.
 - b. The switch is currently flipped down to the “CLOSED” position. To open the valve, switch it up to the “OPEN” position. NOTE: this switch has 3 positions: up = “OPEN”, center = Neutral (no label), and down = “CLOSED”.
- 4 Make sure the pressure decreases rapidly on the thermocouple pressure gauge.
- 5 Check that the wing nut on the substrate mount feed-through is finger tight.
Note: the wing nut will need retightening once the system is under a vacuum.
Record the time.

End of this procedure.

Procedure IV: Vacuum Leak Test

Overview:

After completing Procedure I: Create a Vacuum, the system is allowed to evacuate for 1 hour. After one hour, the system valves are closed and the thermocouple vacuum gauge reading is recorded. The system is allowed to sit for one hour and the thermocouple vacuum gauge is read again. If the difference between the first and second reading is less than 60 mTorr, the system is able to maintain a vacuum. If the difference in the readings is more than 60 mTorr, Procedure X: Extended Vacuum Leak Test will need to be conducted.

A vacuum is being pulled (see Procedure II: Create a Vacuum)

- 1 Continue pumping for at least 1 hour (extended times are acceptable). Check that all wing nuts on the reaction chamber column and the vacuum pump are finger tight.

After at least one hour has passed:

- 2 Close the throttling valve on the Exhaust Valve Controller (EVC)
 - a. Flip the switch down to the "CLOSED" position.
 - b. Rotate the knob counter-clockwise into the "CLOSED" position.
- 3 Close the main valve on the vacuum pump.
- 4 Unplug the vacuum pump (to turn it off).
- 5 Record the time
- 6 Record the pressure from the thermocouple pressure gauge.
- 7 Allow the system to sit for 1 hour

After 1 hour has passed:

- 8 Record the time
- 9 Record the pressure from the thermocouple pressure gauge.
- 10 Record the difference between the first and second thermocouple pressure gauge readings
 - a. An increase of up to 60 mTorr (μmHg) is acceptable

- b. An increase greater than 60 mTorr indicates there is a leak – Do not attempt CVD. Go to Procedure X: Extended Vacuum Leak Test

End of this procedure.

Procedure V: Starting the H₂ Flow

Overview:

The substrate is inside the chamber and the chamber has been checked for leaks. The digital manometer is zeroed to create the baseline for the pressure measurements used to introduce the Hydrogen and Methane. The Hydrogen flow is started and set to a pressure of 10-15 Torr.

- 1 Plug in the vacuum pump (turn it on).
- 2 Completely open the main valve on the vacuum pump.
- 3 Open the throttling valve by switching to “OPEN” on the exhaust valve controller
 - a. The knob is in the ‘closed’ position, rotate it one position clockwise, to align with the line just above the lead line to the closed position. This is manual mode.
 - b. The switch is flipped down to the “CLOSED” position. To open the valve, switch it up to the “OPEN” position. NOTE: this switch has 3 positions: up = Open, center = Neutral (no label), and down = Closed.
- With the vacuum pump running, all gas valves closed and the Pre-Reactor, throttling and main valve open, allow the pressure to reached its minimum value on the digital readout on the Baratron Pressure Gauge, this should not take long being a vacuum test was just completed.
- 4 Set the digital (manometer) readout on the Baratron Pressure Gauge to zero using a small screwdriver.
- 5 Unplug the thermocouple vacuum gauge (turn it off).
- 6 Check that the exhaust valve controller set point dial is set to the desired pressure
 - a. Set to 70 for the brain coral micro texture CVD = 70 Torr (mmHg)
 - b. Check that the switch below the set point dial is flipped up into the “INT” position (not down in the “EXT” position).
- 7 Check that Hydrogen flow controller is at the appropriate set point
 - a. Set to 99 sccm for the brain coral CVD. To produce a flow of 99 sccm, the calculated setting for the dial is 490 (4 in the window, 90 on the dial ring).
 - b. Check that the Hydrogen flow controller readout is at zero +/-.

(End procedure)

Procedure V: Starting the H₂ Flow (continued)

- 8 Check that the Methane flow controller is at the appropriate set point
 - c. Set to 1 sccm for a brain coral CVD. To produce a flow of 1 sccm, the calculated setting for the dial is 139 (1 in the window, 39 on the dial ring).
 - d. Check that the Methane flow controller readout is at zero +/-.
- 9 Open the Hydrogen gas cylinder
 - a. Open the valve on the Hydrogen cylinder two full rotations
 - b. Open the regulator valve to the Hydrogen cylinder
 - i. NOTE: the regulator is set at ~8 psi
- 10 Open the Gas Controller Panel - Fully open the Hydrogen flow valves (2 valves, 1 before and 1 after the flow controller) on the gas flow controller panel
- 11 Start the flow of Hydrogen
 - a. Turn on the Hydrogen Flow Controller power supply/readout by switching the right lever up into the "ON" position
 - b. Start the flow by switching the left lever up into the "FLOW" position
- 12 Record the start time of Hydrogen gas flow.
 - a. Allow the Hydrogen gas to flow for 10 minutes.
 - b. Set up the infrared (IR) thermometer during the 10 minute timed flow (see Procedure IX: IR thermometer measurements)
- 13 Record the time after 10 minutes has passed

The Hydrogen Flow Controller will read 99 sccm +/-
- 14 Set the chamber pressure to 10 -15 Torr
 - a. Set the Open/Close switch on exhaust valve controller to manual mode.
 - i. The knob is in the manual mode position (aligned with the line just above the lead line to the closed position.)
 - ii. Switch the lever into the neutral (middle) position (neither on open or close).
 - b. Flip the switch to "open" to decrease the pressure, "close" to increase the pressure.

Note: There is a delayed reaction when using the exhaust valve controller. If switched up into the 'open' position for too long, the valve will fully open and the pressure will drop to zero. If switched down into the closed position, the valve will fully close and the H₂ gas flow will create a pressure. This will be evident by the continual rise on the digital readout on the Baratron Pressure Gauge. Patience and a steady hand are required.

End of this procedure.

Procedure VI: Microwave Generation & Methane

Overview:

The Hydrogen is still flowing and the thermometer is set up. A Fan and a water-cooling jacket are used to cool the chamber while microwaves are being generated and the sample is heating/hot. The chamber pressure is increased to the setting on the throttle valve controller dial. The amperage is then minimized on the microwave generator and Methane is then introduced to the system. Time and temperature recordings are taken for the duration of the CVD process.

- 1 Turn on the cold water to the chamber cooling jacket. The water valve is located behind the CVD reactor. Use cold water only.
- 2 Turn on the chamber cooling fan located on the far right of the CVD reactor - check that the fan is aimed at the chamber
- 3 Check that the transformer knob is at zero.
- 4 Plug in the Microwave Generator power cable.
- 5 Turn on the Microwave Generator
 - a. turn on the microwave generator power switch and wait for 5 seconds
 - b. the orange 'standby' lamp will come on
- 6 Push the black "Operate On" button - the red "Operate" lamp will come on.
- 7 Slowly adjust the transformer until the anode voltage reads 0.IV
 - a. The meter will start to move when the transformer reaches about 140
 - b. A plasma should now be forming in the chamber. Note: do not look directly at the sample w/o the proper safety glasses. The sample can safely be seen in the mirror at the top of the chamber.
- 8 Minimize the current using the stub tuners
 - a. While holding the stub, release the set screw.
 - b. Making very small movements, slide the stub (in and out) on the first tuner and adjust it to the minimum current on the current meter. If the stub is slid too far up or down, the needle on the gauge will deflect and show an increase.
 - c. Repeat (a) and (b) on the second and third stub.
- 9 Turn the exhaust valve-controlled knob clockwise to "SS" (slow stop) mode

Procedure VI: Microwave Generation (continued)

The digital manometer readout on the Baratron Pressure Gauge will show the pressure increasing.

- 10 Slowly increase the anode voltage to the desired setting (for the brain coral micro texture CVD, voltage = 0.2V)

- 11 Repeat Step 7 to adjusting the stub tuners to obtain the minimum reflected current.

The digital manometer readout on the Baratron Pressure Gauge is ~70 Torr. Hydrogen plasma with the desired conditions is produced in the chamber

- 12 Record the time, temperature and voltage every 10 minutes. Allow the reaction to continue for 30 minutes.

	Time:	
	Temperature:	

After 30 minutes:

- 13 Open the Methane gas cylinder

- a. Open the valve to the Methane cylinder two full rotations
- b. Open the regulator valve on the Methane cylinder
 - i. The Methane regulator is set to ~17 psi

Note: Unlike the Ar or H₂ flow sequence, the Methane Flow Controller is opened prior to the valves on the Gas Control Panel. This is on purpose and due to the very low flow of Methane.

- 14 Turn on the Methane Flow Controller power supply/readout and open the flow controller

- a. Turn on the Methane Flow Controller power supply/readout by switching the right lever up into the "ON" position
- b. Open the flow controller by switching the left lever up into the "FLOW" position. Allow the controller time to stop fluctuating (may take 1+ minute or more).

- 15 Open the Gas Controller Panel

- a. Gently and slowly open the Methane flow valve before the flow controller. Allow the controller time to stop fluctuating.
 - b. Gently and slowly open the Methane flow valve after the flow controller. Allow the controller time to stop fluctuating.
- 16 Record the time and temperature. Continue to record the time and temperature at regular intervals (recommended: 15 minutes intervals – see chart, next page).
- c. If the temperature is fluctuating, check the anode voltage on the Microwave Generator
 - d. If the anode voltage on the Microwave Generator is not at the desired setting, adjust the transformer to achieve the desired anode voltage. Record the anode voltage before the adjustment was made and the time the adjustment was made.

The CVD process is now taking place. Allow this reaction to continue for your pre-determined time period, taking temperature readings at regular intervals.

Procedure VI: Microwave Generation (continued)

Time & Temperature Chart

	Time	Temp (°C)	CH4 flow (sccm)	H2 Flow (sccm)	Pressure (Torr)	Defltn Current (mA)	Input Voltage (V)
0:00							
0:15							
0:30							
0:45							
1:00							
1:15							
1:30							
1:45							
2:00							
2:15							
2:30							
2:45							
3:00							
3:15							
3:30							
3:45							
4:00							
4:15							
4:30							
4:45							
5:00							
5:15							
5:30							
5:45							
6:00							

End of this procedure.

Procedure VII: CVD Stop Process

Overview:

The CVD process is now complete. The flow of methane is stopped and the microwave generator is shut down. While allowing the Hydrogen to flow for 10 minutes, the IR thermometer is put away. The Hydrogen gas is stopped and a vacuum is pulled. The water cooling jacket and cooling fan for the chamber are turned off and the specimen is allowed to sit for a least 2 hours to cool.

- 1 Stop the flow of Methane
 - a. Stop the flow by switching the left lever from the "FLOW" position to the middle.
 - b. Turn off the Methane Flow Controller power supply/readout by switching the right lever down into the "OFF" position.
 - c. Record the time
- 2 Close the Gas Controller Panel - Close the Methane flow valves (2 valves, 1 before and 1 after the flow controller) on the gas flow controller panel
- 3 Close the Methane gas cylinder
 - a. Close the regulator valve to the Methane cylinder
 - b. Close the valve on the Methane cylinder
- 4 Gradually turn off the transformer – slowly rotate the knob to the left.
- 5 Turn power down the microwave generator
 - a. Push the red "Operate Off" button
 - b. The red "Operate" lamp will turn off, the orange "Standby" will stay on.
 - c. Allow the unit to run on "Standby" for 10 minutes – this will also keep the fan running on the magnetron.
 - d. Put away the infrared (IR) thermometer during the 10 minute timed cool down
- 6 Turn off the Microwave Generator power switch
- 7 Unplug the Microwave power cable
- 8 Stop the flow of Hydrogen
 - a. Stop the flow by switching the left lever from the "FLOW" position to the middle.
 - b. Turn off the Hydrogen Flow Controller power supply/readout by switching the right lever down into the "OFF" position.

Procedure VII: CVD Stop Process (continued)

- 1 Close the Gas Controller Panel - Close the Hydrogen flow valves (2 valves, 1 before and 1 after the flow controller) on the gas flow controller panel
- 2 Close the Hydrogen gas cylinder
 - a. Close the regulator valve to the Hydrogen cylinder
 - b. Close the valve on the Hydrogen cylinder
- 3 Open the throttling valve on the Exhaust Valve Controller (EVC)
 - a. The knob is in the 'SS' position, rotate it one position counter-clockwise, to align with the line just above the closed position. This is manual mode.
 - b. The switch is currently in the "Neutral" position (center). To open the valve, switch it up to the "OPEN" position.

The pressure will drop to 0 +/- on the Baratron Pressure Gauge

- 4 Plug in the thermocouple vacuum gauge
- 5 Record the time

After 10 minutes:

- 6 Close the throttling valve on the Exhaust Valve Controller (EVC)
 - a. Flip the switch down to the "CLOSED" position.
 - b. Rotate the knob counter-clockwise into the "CLOSED" position
- 7 Close the main valve on the vacuum pump
- 8 Unplug the vacuum pump
- 9 Turn off the water to the water cooling jacket
- 10 Turn off the fan on the reaction chamber
- 11 Let the specimen remain in the chamber for 2+ hours to cool

End of this procedure.

Procedure VIII: System Shut Down

Overview:

A vacuum must always be maintained in the chamber. The system should never be left open to atmospheric pressure for any longer than need be to insert/remove specimens. If the system has been opened, a vacuum should be pulled for at least one hour. After pulling a vacuum, the system can be shut down. When the system is shut down, all valves should be closed.

Some of the following instructions may have already been completed, depending on which procedure preceded this one.

- 1 Close the Pre-Reactor valve on the gas flow panel
- 2 Close the throttling valve on the Exhaust Valve Controller (EVC)
 - a. Flip the switch down to the “CLOSED” position.
 - b. Rotate the knob counter-clockwise into the “CLOSED” position.
- 3 Close the main valve on the vacuum pump
- 4 Unplug the vacuum pump (turn if off)
- 5 Check that the thermocouple gauge is unplugged (turn if off)
- 6 Turn off the EVC. Pull the lever out and flip it down into the “off” position.
- 7 Turn off the Baratron Pressure gauge. Pull the lever out and flip it down into the “off” position.
- 8 Turn off the cooling fan behind the EVC.

End of this procedure.

Procedure IX: IR thermometer measurements

Overview:

The IR Thermometer measures temperatures between 600 – 3000 °C. In the case of CoCrMo, the emissivity is set to 0.27. The temperatures will run near 1000 °C. The thermometer is set up on a tripod aimed through the viewer at the mirror at top of the reactor tower. The specimen can be seen in this mirror. When using the thermometer, be aware that the position on the tripod may drift, therefore, you should ‘scan’ the specimen for the peak temperature.

- 1 Set up the tripod by extending the legs raising the head to the highest level at which you can easily see through the site. Lock in the height using the knob.
- 2 On a table, open the silver hard case that contains the thermometer
- 3 Remove the thermometer and attach it to the head of the tripod. The dovetail clip for to connect the thermometer to the trip should be attached to the thermometer.
- 4 Remove the power supply and plug it into an outlet nearest the tripod.
- 5 Connect the power supply to the thermometer. The input is located on the front, next to the lens.
- 6 Remove the lens cap – store in the thermometer case
- 7 Turn the thermometer on.
 - a. The digital display will illuminate.
 - b. Check that the emissivity is set to the desired level
 - c. Focus the lens on the specimen
 - d. Unless the temperature you are measuring is greater than 600 °C, the readout will display “Lo”

End of this procedure.

7 APPENDIX B:

%% Written by Nathanael Seay adapted from David Mercier

% CRM Group, Avenue du Bois Saint-Jean 21, B27 – Quartier Polytech 4, 4000 Liège,
Belgium

% <https://tridimap.readthedocs.io/en/latest/>

%% Get files

clc

clear

```
%-----
% -----inputs-----
%-----  

binsize=2;  

limit=.00000001; %precision  

maxiter= 10000; %maximum loop iterations  

M=2; %number of phases  

soubor= '5A_results'; %output file name  

% How many files?  

File_number = 5;  

%sample? (e.g. '5A')  

sample='5A';  

%format: 'Row_1_5A.xlsx'  

%number of indents per line  

indents=30;  

%position vector  

position=[50,60,70,120,220];  

%-----  

% -----End inputs-----
%-----  

%initializing -----  

%fetching excel files-----  

for k = 1:File_number
```

```

myfilename = sprintf('Row_%d_%s.xlsx', k, sample);
%row{k} = importdata(myfilename);
row{k}= readtable(myfilename,'Range','A3:K32','ReadVariableNames',false);
end

%extracting row 9: modulus-----
for k = 1:File_number

    placeholder = row{:,k};
    row_modulus_array=table2array(placeholder);
    row_modulus(:,k)=row_modulus_array(:,9);

end
%% Delete outliers
%row_modulus_clean=zeros(indents, File_number);

for k = 1:File_number

    row_modulus_clean{:,k}=deleteoutliers1(row_modulus{:,k},1);

end
%% Find the means
% Modulus_row1_mean= mean(modulus_array_row1_clean)

for k = 1: File_number

    row_mean(:,k)= mean(row_modulus_clean{:,k});
end
%% Deconvolute line 1
figure
line1{1}=row_modulus_clean{:,1}';

for k= 2:File_number

    line1{k,:}=[line1{k-1} row_modulus_clean{:,k}];
end
%line =reshape(row_modulus_clean,1,[])
% binsize=3;
% limit=.00000001 %precision
% maxiter= 10000 %maximum loop iterations
% M=3; %number of phases
soubor= '5A_line1_results';%output file name
minbin= min(line1{5,1});
maxbin= max(line1{5,1});
kategorie=minbin:binsize:maxbin;
E= line1{5,1};
n=length(E);%number of values in a list
hi=histc(E,kategorie); %histogram by categories
exphist=zeros(length(hi),2);
Epdf=hi/n; %probability density function (property must be divided by the number of values and binsize)
Epdf=Epdf/binsize;
bar(kategorie,Epdf);
%adds a title, x-axis description, and y-axis description

```

```

title('PDF');
xlabel('Property');
ylabel('Frequency density');
exphist(:,1)= kategorie' ; %fill the first column of A by vector of categories
exphist(:,2)= Epdf; %fill the secondf column of A by PDF

%-----
%---Deconvolution algorithm
%-----

norma2=1;
minnorma=1;
iter=0;
maxE=max(E); %maximum value in E vector
N=length(E); %dimension of E vector

while( (norma2>limit) && (iter<=maxiter))

    r=rand(M-1,1); %nahodny vektor M-1 cisel 0,1
    r=sort(r); %vzestupne serazeny vektor r
    meze(1)=0; %prvni mez je na nule
    pom= maxE .* r; % generace M-1 mezi z nahodneho vektoru

    for i=1:M-1

        meze(i+1)=pom(i); % generace M-1 mezi

    end

    meze(M+1)=maxE; %posledni mez
    sE=sort(E); %vzestupne serazeny vektor E

    for i=1:M+1

        index_meze(i)=N; %naplni vektor indexu maximalni hodnotou

    end
    index_meze(1)=0; %index pred prvni mezi je nula
    j=2; %zacinam od druhe meze (prvni je nula)
    mez=meze(j);

    for i=1:N %cyklus pres vsechny hodnoty

        if (sE(i) > mez)
            index_meze(j)=i-1; %ulozi index hodnoty, ktera lezi pod mezi
            j=j+1;
            mez=meze(j);

        end
    end

    x=exphist(1,1); %prvni kategorie

```

```

for i=1:M %cyklus pres faze
    vektor=sE(index_meze(i)+1:index_meze(i+1));
    if (length(vektor)>1)
        prumer(i) = mean(vektor);
        stddev(i) = std(vektor);
    else
        prumer(i) = 0;
        stddev(i) = 0;
    end
    f(i)=length(vektor)/N; %fraction
end

for j=1:M %cyklus pres faze
    x=exphist(1,1);
    if (prumer(j)~=0)
        %p(1,j)=cdf('normal',x,prumer(j), stddev(j)); %cdf pro prvni kategorii
        p2(1,j)=pdf('normal',x,prumer(j), stddev(j)); %pdf
    else
        %p(1,j)=0;
        p2(1,j)=0;
    end
    for i = 2 : length(exphist) %cyklus pres vsechny kategorie
        x_prev=exphist(i-1,1);
        x=exphist(i,1);
        if (prumer(j)~=0)
            p2(i,j)=pdf('normal',x,prumer(j), stddev(j))*f(j);
        else
            p2(i,j)=0;
        end
    end
end
norma2=0;

```

```

for i = 1 : length(exphist)

p_all2(i)=0;

for j=1:M %cyklus pres faze

p_all2(i)=p_all2(i)+p2(i,j);

end

norma2=norma2+(exphist(i,2)-p_all2(i))^2 * exphist(i,2)^2;

end

iter=iter+1;

if(norma2<minnorma)

% output if precision was reached
minnorma=norma2;
minmeze=meze;
minprumer=prumer;
minstddev=stddev;
minf=f;

cla;
%plot(exphist(:,1), exphist(:,2),'ko'
bar(exphist(:,1), exphist(:,2),'w')
hold on %legend ('show');
for j=1:M

t=sprintf('%8.3f\n%8.3f\n%8.3f\n', minprumer(j), minstddev(j), minf(j));

switch j
    case 1
        plot(exphist(:,1),p2(:,1),'b');
    case 2
        plot(exphist(:,1),p2(:,2),'r');
    case 3
        plot(exphist(:,1),p2(:,3),'g');
    case 4
        plot(exphist(:,1),p2(:,4),'y');
    case 5
        plot(exphist(:,1),p2(:,5),'m');
    case 6
        plot(exphist(:,1),p2(:,6),'c');

otherwise

end

end

```

```

%graphical output
plot(exphist(:,1),p_all2,'--')

switch M

case 1
    legend ('Experiment','#1','Overall PDF');
case 2
    legend ('Experiment','#1','#2','Overall PDF');
case 3
    legend ('Experiment','#1','#2','#3','Overall PDF');
case 4
    legend ('Experiment','#1','#2','#3','#4','Overall PDF');
case 5
    legend ('Experiment','#1','#2','#3','#4','#5','Overall PDF');
case 6
    legend ('Experiment','#1','#2','#3','#4','#5','#6','Overall PDF');
otherwise

end

%adds a title, x-axis description, and y-axis description
%title('PDF');
xlabel('Modulus GPa');
ylabel('Frequency density');
end %end of if(norma2<minnorma)

end %end of iteration loop

%write to file

%soubor= 'String';
f=fopen(soubor, 'wt');
fprintf(f,'Decon 3.0 ----Output----\n');
fprintf(f,'Calculated on %s\n', datestr(now));
fprintf(f,'-----\n');
fprintf(f,'Number of iterations: %d\n',iter-1);
fprintf(f,'Required norm= %e \n',limit);
fprintf(f,'Resulting norm= %e \n',minnorma);
fprintf(f,'-----\n');
for j=1:M

fprintf(f,'Distribution #%d \n',j);
fprintf(f,'Mean %f\n',minprumer(j));
fprintf(f,'St. Dev. %f\n',minstddev(j));
fprintf(f,'Fraction %f\n',minf(j));
fprintf(f,'-----\n');

end

```

```

fprintf(f,'n----- End -----n');
fclose(f);
%Show text_log
t=strcat('Output file written to: ', soubor);

%-----
%---end of Deconvolution algorithm
%-----

%% plot the means
figure
plot(position, row_mean)
xlabel('Depth (micrometers)')
ylabel('Modulus')
title('Sample Modulus vs. Depth')
%% Function box
function [b,idx,outliers] = deleteoutliers1(a,alpha,rep)
%

if nargin == 1
    alpha = 0.05;
    rep = 0;
elseif nargin == 2
    rep = 0;
elseif nargin == 3
    if ~ismember(rep,[0 1])
        error('Please enter a 1 or a 0 for optional argument rep.')
    end
elseif nargin > 3
    error('Requires 1,2, or 3 input arguments.');
end

if isempty(alpha)
    alpha = 0.05;
end
b = a;
b(isinf(a)) = NaN;

%Delete outliers:

outlier = 1;

while outlier
    tmp = b(~isnan(b));
    meanval = mean(tmp);
    maxval = tmp(find(abs(tmp-mean(tmp))==max(abs(tmp-mean(tmp))))));
    maxval = maxval(1);
    sdval = std(tmp);
    tn = abs((maxval-meanval)/sdval);
    critval = zcritical(alpha,length(tmp));
    outlier = tn > critval;
    if outlier
        tmp = find(a == maxval);
        b(tmp) = NaN;
    end
end

```

```
        end
    end
if nargout >= 2
    idx = find(isnan(b));
end
if nargout > 2
    outliers = a(idx);
end
if ~rep
    b=b(~isnan(b));
end
return
end

function zcrit = zcritical(alpha,n)

    % Computes the critical z value for rejecting outliers (GRUBBS TEST)
    tcrit = tinv(alpha/(2*n),n-2);
    zcrit = (n-1)/sqrt(n)*(sqrt(tcrit^2/(n-2+tcrit^2)));

end
```

8 APPENDIX C

%% Hardstuff.m Written by Nathanael Seay

```
%The purpose of this program is to read in an AFM FFM image
%section the image in to blocks
%analyze each block based on some given threshold
%and to assemble data into a single gradient for pixel intensity

%% SET UP WORKSPACE

clc;           %clear command window
clear;          %clear variables
close all;      %close all figures
workspace;     %workspace panel open
fontSize = 20;  %Set font size

cd 'C:\Users\Nate\Google Drive\Research\THESIS DATA\AFM\200130'      %set
current directory

%% READ IN IMAGE & RESIZE

sizeC = 256;
sizeR = 256;
myimage=imread('Image0021EcT.tif');           %read in image
mysizeimage=imresize(myimage,[sizeC,sizeR],'nearest');    %define pixels
mygrayimage=rgb2gray(mysizeimage);             %convert to grey
image
imshow(mygrayimage);                         %display image for check
% figure
% mygrayimage=imfill(mygrayimage,'holes')
% imshow(mygrayimage);
```

```

% title('filled image');
[rows, columns, numberOfColorBands] = size(mygrayimage);
figure

%% Split into blocks

blockSizeR = sizeR/8; % Rows in block.
blockSizeC = sizeC/8; % Columns in block.

% Figure out the size of each block in rows.
% Most will be blockSizeR but there may be a remainder amount of less than that.
wholeBlockRows = floor(rows / blockSizeR);
blockVectorR = [blockSizeR * ones(1, wholeBlockRows)];%, rem(rows, blockSizeR)];
% Figure out the size of each block in columns.
wholeBlockCols = floor(columns / blockSizeC);
blockVectorC = [blockSizeC * ones(1, wholeBlockCols)];%, rem(columns, blockSizeC)];

% Create the cell array, ca.

ca = mat2cell(mygrayimage, blockVectorR, blockVectorC);

% Now display all the blocks.
plotIndex = 1;
numPlotsR = size(ca, 1);
numPlotsC = size(ca, 2);
for r = 1 : numPlotsR
    for c = 1 : numPlotsC
        % fprintf('plotindex = %d, c=%d, r=%d\n', plotIndex, c, r);
        % Specify the location for display of the image.
        subplot(numPlotsR, numPlotsC, plotIndex);
        % Extract the numerical array out of the cell
        rgbBlock = ca{r,c};
        imshow(rgbBlock);
        [rowsB,columnsB,numberOfColorBandsB] = size(rgbBlock);
        % Make the caption the block number.
        caption = sprintf('Block #%d of %d\n%d rows by %d columns', ...
            plotIndex, numPlotsR*numPlotsC, rowsB, columnsB);
        %title(caption);
        drawnow;
        % Increment the subplot to the next location.
        plotIndex = plotIndex + 1;
    end
end

```

```
% % Display the original image in the upper left.
% subplot(4, 6, 1);
% imshow(mygrayimage);
% title('Original Image');
```

%% ANALYZE THE BLOCKS

```
r=1;
c=1;
for r = 1 : numPlotsR
    for c = 1 : numPlotsC

        % Extract the numerical array out of the cell
        grayBlock = ca{r,c};
        BW{r,c} = im2bw(grayBlock,.5);

        nWhite = sum(BW{r,c}, 'all');
        nBlack = numel(BW{r,c}) - nWhite;
        Fraction_O_Hardstuff{r,c} = nWhite/numel(BW{r,c});

    end
end
figure
imshow(BW{1,1})

Fraction_O_Hardstuff=cell2mat(Fraction_O_Hardstuff);
profile = mean(Fraction_O_Hardstuff)

blockpixels = blockSizeR * blockSizeC ;

%profile= blockpixels*profile*wholeBlockRows;

x=[1:8]'-1)*(30/7);
plot(x',profile)
xx = linspace(0,max(x));
profile2=fit(x, profile','exp2')
[profile3, scraps]=fit(x, profile','poly5')

% figure
% [pd, xi]= ksdensity(profile)
% % y1 = pdf(pd,x)
```

```

% plot(xi, pd)

hold on
%profile2=fit(x, profile','poly6');
% %[fitpara, scraps]=gamfit(profile,.1)
%
% %fit =gampdf(xx,fitpara(1), fitpara(2));
% %fplot(@(xx) gampdf(xx,fitpara(1),fitpara(2)))
% plot(profile2, 'g')
plot(profile3)

hold off
%% Analyze fit

% profile_function= @(x) profile3
%
% int=integral(profile_function,0,7)
%
% figure
% plot(int)

%% Time to %50 drop

y=feval(profile3,xx);
[maxy,l]=max(y);
maxx= xx(l);
xxx=linspace(maxx,max(x));
y=feval(profile3,xxx);
miny=min(y);

ybar= (maxy-miny)/2+ miny;

deltay=abs(y-ybar);

[error,l]= min(deltay);

time_to_fifty_percent=xxx(l)

%% Area under the curve

INT = integrate(profile3, xx, 0);

```

```
area_under_curve= INT(100)

%% Centroid

profile3vector=profile3(xx);

int_profile3= trapz(profile3vector);

num=xx*int_profile3-trapz(int_profile3);

int_den=trapz(profile3vector);

centroid= num/int_profile3
```

9 APPENDIX D:

```
#####
# Interfacial Fracture

# Mark Tschopp, Nathan Rhodes, Nathanael Seay 2020

# Imp_exe -var datfile Fe_110_sig3.txt -var nloop 100 < in.gb_fracture.txt

# Simulation deletes atoms outside of +/- deldist from GB and constrains and pulls

# atoms outside of +/- fixdist from GB to fracture the GB

#####

variable datfile index TiAl_TiC_vesta2.imp
variable strain equal 0.001
variable nloop equal 150
variable repx equal 1
variable repz equal 1
variable strain2 equal "1+v_strain"
variable deldist equal 168
variable fixdist equal 160

#####

# INITIALIZATION

units      metal
dimension   3
boundary    p    p    p
atom_style  atomic
atom_modify map array

#####

# SIMULATION CELL VARIABLES (in Angstroms)

read_data ${datfile}

#variable minlength equal 100
```

```

variable xlen equal lx
variable ylen equal ly
variable zlen equal lz

print "lx: ${xlen}"
print "ly: ${ylen}"
print "lz: ${zlen}"

# Replicate simulation cell in each direction

replicate ${repx} 1 ${repz}

#####
# INTERATOMIC POTENTIAL

pair_style      hybrid meam/c morse 2.5
pair_coeff      * * meam/c library3.meam Ti Al C TiAlCpar2.meam Ti Al C
pair_coeff      2 3 morse 0.4691 1.738 2.246

neighbor        2.0 bin
neigh_modify    delay 3

# Compute stress information for Atomeye visualization

compute stress all stress/atom NULL
compute stress1 all reduce sum c_stress[1]
compute stress2 all reduce sum c_stress[2]
compute stress3 all reduce sum c_stress[3]
compute stress4 all reduce sum c_stress[4]
compute stress5 all reduce sum c_stress[5]
compute stress6 all reduce sum c_stress[6]

#####
# Minimize first

reset_timestep 0
thermo          10
thermo_style    custom step temp lx ly lz press pxx pyy pzz pe c_stress1 c_stress2
c_stress3 c_stress4 c_stress5 c_stress6
min_style      cg
fix 1 all box/relax x 0.0 y 0.0 couple none vmax 0.001
minimize 1.0e-25 1.0e-25 1000 10000
unfix 1

```

```

# Compute distance for each side of the grain boundary to displace

variable lz1 equal lz
variable lz0 equal ${lz1}
variable lzdelta equal "v_strain*v_lz0/2"

# Setup file output (time in ps, pressure in GPa)

variable p1 equal "(lz-v_lz0)/v_lz0"
variable p2 equal "-pxx/10000"
variable p3 equal "-pyy/10000"
variable p4 equal "-pzz/10000"
variable p5 equal "-pxy/10000"
variable p6 equal "-pxz/10000"
variable p7 equal "-pyz/10000"
variable p8 equal "pe"

# Output stress and strain information to datafile for Matlab post-processing

#fix equil1 all print 1 "${p1} ${p2} ${p3} ${p4} ${p5} ${p6} ${p7} ${p8}" file
data.${datfile}.txt screen no
fix equil1 all print 1 "${p1} ${p2} ${p3} ${p4} ${p5} ${p6} ${p7} ${p8}" file data.txt screen
no
fix 1 all nve
run 1
unfix 1
variable pressf1 equal pzz
variable pressf equal ${pressf1}

#####
# Create cfg files with stress in y direction for AtomEye viewing

dump 1 all atom 100 pull.dump #mass type xs ys zs c_stress[3]

#dump 1 all cfg 500 ${datfile}_*.cfg mass type xs ys zs c_stress[3]

#####

# CREATE REGIONS FOR BOUNDARY CONDITIONS

# Delete groups of atoms far from boundary

region rlow block 0 200 0 200 -200 0 units box
region rhigh block 0 200 0 200 ${deldist} 200 units box

```

run 1

```
$$$$$$$$$$$$$$$$$$$$$$$$$$$$$$$$$$$$$$$$$$$$$$$$$$$$$$$$$$$$$$$$$$$$
unfix 4

#####
# MS Deformation loop

variable a loop ${nloop}
label loop

# Increase box bound and minimize again

# reset_timestep 0

change_box gblow z delta -${lzdelta} 0 remap units box
change_box gbjhigh z delta 0 ${lzdelta} remap units box

minimize 1.0e-25 1.0e-25 1000 10000
neigh_modify exclude group gleftb glefft
```

run 1

```
print "Pressf: ${pressf}"
variable pdiff equal "pyy - v_pressf"
print "Pressf: ${pressf}"
print "Pdiff: ${pdiff}"
#if ${pdiff} > 10000 then "exit"
variable pressf1 equal pyy
variable pressf equal ${pressf1}

next a
jump TiCAL_Rhodes3.in loop

unfix equil1

#####
# SIMULATION DONE

print "All done"
```


10 APPENDIX E

```

#-----single atom impact-----

clear
variable thisfile string Impact2.in.txt
variable logfile string result_run01.log
variable restartfile string ConWrestart600200

#-----initialize-----

units metal
dimension 3
boundary p p f
atom_style atomic
atom_modify map array

#----- Read data-----

read_data Ti3Al_supstrate5.imp.txt

variable xlen equal lx
variable ylen equal ly
variable zlen equal lz
variable xylen equal xy
variable xleni equal lx-10
variable yleni equal ly-10
variable zleni equal -lz+10

print "lx: ${xlen}"
print "ly: ${ylen}"
print "lz: ${zlen}"

#-----carbon initial position-----

variable C_init_position equal 3

#-----Steps-----
variable substrate_temp_rescale_step equal 2000
variable total_cycles equal 64 #5000
variable cycle_steps equal 128 #10000

```

```

variable check_interval equal 1 #100

#-----create substrate atoms-----

#from read data file

#-----Regions-----

# region 1 prism 0 10 0 ${ylen} -${zlen} 0 ${xylen} 0 0 #left berendsen wall
# region 2 prism ${xleni} ${xlen} 0 ${ylen} -${zlen} 0 ${xylen} 0 0 #right berendsen wall
# region 3 prism 0 ${xlen} 0 10 -${zlen} 0 ${xylen} 0 0 #back wall berendsen wall
# region 4 prism 0 ${xlen} ${yleni} ${ylen} -${zlen} 0 ${xylen} 0 0 #front berendsen wall
# region wall union 4 1 2 3 4
region 5 prism 0 ${xlen} 0 ${ylen} -${zlen} ${zleni} ${xylen} 0 0 #bottom
# region 6 prism 0 ${xlen} 0 ${ylen} 0 3.1 ${xylen} 0 0 #air top
region mobile prism 10 ${xleni} 10 ${yleni} ${zleni} 0 ${xylen} 0 0 #middle region
region whole prism 0 ${xlen} 0 ${ylen} -${zlen} 10 ${xylen} 0 0 #entire simulation

#-----simulation box-----

#create_box 3 whole

#-----Groups-----

# group wall_group region wall
group mobile_group region mobile
group bottom region 5
group non_fixed subtract all bottom
group berendsen subtract all bottom mobile_group

#-----Mass-----

#from read data file

#-----Carbon velocity and substrate temp-----

variable substrate_temp equal 1539 #kelvin
variable C_energy equal 600 #ev
variable C_speed equal (-1)*sqrt(${C_energy}*1.602e-19*2.0/(12.0107*1.661e-27))*1.e10/1.e12 # A/ps

#-----Potential-----
pair_style      hybrid meam/c morse 2.5

```

```

pair_coeff      * * meam/c library3.meam Ti Al C TiAlCpar2.meam Ti Al C
pair_coeff      2 3 morse 0.4691 1.738 2.246
neighbor        2.0 bin
neigh_modify    delay 0

#-----fix bottom substrate-----
fix zeroforce bottom setforce 0 0 0

#-----initial substrate temp-----
velocity non_fixed create ${substrate_temp} 10000 rot yes dist gaussian

#-----relax-----
fix 1 all nve
fix 2 non_fixed temp/rescale 100 ${substrate_temp} ${substrate_temp} 0.1 1.0
compute cmp_substrate_temp non_fixed temp
timestep 0.0001
thermo_style custom step temp pe cpu tpcpu spcpu #cmp_substrate_temp
thermo_modify lost warn
thermo 25
run ${substrate_temp_rescale_step}
unfix 1
unfix 2
unfix zeroforce
write_restart ${restartfile}

#>>>>>>>>>>>>>>Bombardment<<<<<<<<<<<<<<
#-----C velocity-----
variable C_azi_angle equal "random(0,6.2831852, 1)"
variable C_polar_angle equal "random(0,20/180*3.1415926, 4)" #radians
variable rn equal 0.0
variable C_x equal 142
variable C_y equal 250
variable C_z equal ${C_init_position}
variable C_vx equal ${C_speed}*sin(${C_polar_angle})*cos(${C_azi_angle})
variable C_vy equal ${C_speed}*sin(${C_polar_angle})*sin(${C_azi_angle})
variable C_vz equal ${C_speed}*cos(${C_polar_angle})
variable C_zb equal ${C_init_position}-.5
variable C_zt equal ${C_init_position}+.5
region C_start_rgn prism 0 ${xlen} 0 ${ylen} ${C_zb} ${C_zt} ${xylen} 0 0 units lattice

#-----Shooting the carbon-----
variable i loop ${total_cycles}

```

```

variable n loop ${total_cycles}
label cycle_loop

#-----reset-----
clear
read_restart ${restartfile}
pair_style      hybrid meam/c morse 2.5
pair_coeff      * * meam/c library3.meam Ti Al C TiAlCpar2.meam Ti Al C
pair_coeff      2 3 morse 0.4691 1.738 2.246
neighbor        2.0 bin
neigh_modify    delay 0
timestep        0.0001
reset_timestep  0
fix 1 all nve
fix 2 berendsen temp/berendsen ${substrate_temp} ${substrate_temp} 0.01
fix zeroforce bottom setforce 0 0 0
region flying_atoms prism 0 ${xlen} 0 ${ylen} 2.9 10 ${xylen} 0 0 units lattice

#-----print "">>>> shooting the $i -th C...
create_atoms 3 single ${C_x} ${C_y} ${C_z}
group group_all_C type 3
compute Ctemp group_all_C ke
compute_modify Ctemp dynamic yes #carbon temp
compute cmp_substrate_temp non_fixed temp #substrate temp
variable allcke equal c_Ctemp #kinetic energy of C
variable czz equal xcm(grp_all_C,z) # z coord of C
thermo_style custom step temp pe c_cmp_substrate_temp c_Ctemp v_czz cpu tpcpu
spcpu
thermo_modify lost warn
thermo 100

#get random number-----

variable rn equal ${C_azi_angle}
variable rnp equal ${C_polar_angle}
variable C_vx equal ${C_speed}*sin(${rnp})*cos(${rn})
variable C_vy equal ${C_speed}*sin(${rnp})*cos(${rn})
variable C_vz equal ${C_speed}*cos(${rnp})
velocity group_all_C set ${C_vx} ${C_vy} ${C_vz} units box
group grp_all_C type 3
group grp_substrate type 1 2
variable cx equal xcm(grp_all_C,x)
variable cy equal xcm(grp_all_C,y)

```

```

variable cz equal xcm(grp_all_C,z)
print "The $i -th C initial location is ${cx} ${cy} ${cz}"
label cont_run
variable steps equal step
if "${steps} > ${cycle_steps}" then "jump ${thisfile} writeC"
run ${check_interval}
variable numC equal count(grp_all_C)
if "${numC} <= 0" then "jump ${thisfile} writeC" #C lost, jump to writeC to output the Sub
number
if "${allcke} > 0.2" then "jump ${thisfile} cont_run"
label writeC
delete_atoms region flying_atoms
variable Cidx equal $n
if "${numC} <=0" then "variable Cidx equal 0"
variable Cxx equal xcm(group_all_C,x)
variable Cyy equal xcm(group_all_C,y)
variable Czz equal xcm(group_all_C,z)
variable Subnum equal count(grp_substrate)
variable Cnum equal count(grp_all_C)
print ">>>>> Recording $n -th C..."
fix write_CW_info group_all_C print 1 "${Cidx} / ${i} ${Cxx} ${Cyy} ${Czz} ${allcke}"
${steps} ${Cnum} ${Subnum}" title "+" append ${logfile} screen no

```

run 1

```

unfix write_CW_info
if "${numC} > 0" then "next n"
next i
jump ${thisfile} cycle_loop

```

